# Large-scale local-orbital DFT calculations of Si – Ge core – shell nanowires

*Shereif Youssef Mujahed*

A dissertation submitted in partial fulfillment

of the requirements for the degree of

**Doctor of Philosophy**

of

**University College London**.

Department of Physics & Astronomy

&

London Centre for Nanotechnology

University College London

Friday 26th November, 2021

I, Shereif Youssef Mujahed, confirm that the work presented in this thesis is my own. Where information has been derived from other sources, I confirm that this has been indicated in the work.

*This thesis is dedicated to my parents,*

*Iman & Youssef Mujahed.*

*In loving memory of my grandparents,*

*Bernadette Stacey,*

*Fatima Bouzo & Mahmoud Mujahed.*

# Abstract

Nanowires, represent the smallest device dimensionality for efficient transport of electrons and other more exotic quasiparticles. Among a plethora of applications identified, research directed towards field-effect transistors (FETs), the building blocks of next-generation computer processors, is of utmost importance considering current 7 nm FET technologies are expected to be the limit of "top-down" manufacturing techniques. Characterisation of the mechanical and electronic properties of nanowires, by conventional electronic structure techniques, have coincidentally reached a limit due to the maximum simulation sizes they are capable of.

CONQUEST is a code capable of simulation of *millions* of atoms using $O(N)$ methods and *thousands* of atoms using Hamiltonian diagonalisation with a pseudo-atomic orbital basis. Physical quantities calculated using CONQUEST do not exhibit systematic convergence using PAO basis sets, unlike plane-wave codes, so we quantify PAO basis sizes needed to achieve comparable accuracy to plane-wave calculations for a variety of bulk and molecular systems with varying chemical environments. Implementation of the stress tensor, presented in this thesis, resulted in the discovery of slow stress convergence with respect to density matrix localisation. We quantify the $O(N)$ simulation parameters necessary to achieve stress calculations to a required accuracy.

We present the first study of experimentally relevant, surface reconstructed, Si(core)-Ge(shell) nanowires. Vegard's law, used to quantify experimental results and as an approximation in theoretical calculations, has been found to poorly describe our nanowires and we assess the relative error due to its usage. Young's modulus is shown to decrease with increasing shell deposition and dependent on

relative nanowire composition. Poisson ratios, also correlated to composition, exhibit anisotropy. Shell deposition induced strain has been mapped by our method and shows strong anisotropy in different bonding directions. Our nanowires exhibit a direct-to-indirect band gap transition with *intrinsic* uniaxial strains $> 0.5\%$ and effective hole masses 50% smaller than similar unreconstructed nanowires. Finally, valence band offsets which are responsible for the formation of hole gases, were found to be *double* that of unreconstructed models.

# Impact Statement

Open-source software is not simply a free software paradigm, but one that has far reaching benefits to society. A recent European Commission study [1] has found,

> "... an increase of 10% in contributions to Open Source Software code would annually generate an additional 0.4% to 0.6% GDP, as well as more than 600 additional ICT start-ups in the EU."

This demonstrates how small contributions towards open-source software projects can actually create further jobs and stimulate economic growth, improving people's quality of life. Building on this, open-source scientific software can increase public engagement and provide opportunities for the use of software in settings where funding for expensive, research quality software may prove prohibitive (e.g. state schools).

This thesis details one such small contribution to CONQUEST, an open-source, research grade software, released in 2020 to the general public. CONQUEST is a large-scale electronic structure code and has been demonstrated in applications such as biological, molecular and solid state systems. Within the context of this thesis, CONQUEST has been used to probe the mechanical and electronic properties of Si (core) - Ge (shell) nanowires, with applications to next-generation field-effect transistors (FETs). Specifically, we have characterised the modulation of strain due to deposition and its effects on the band gap, effective carrier mass and confinement.

The knowledge gained from our work on nanowires could potentially influence design of future FETs. FETs have applications in almost all consumer electronics, but nanowire FETs would be of particular use in the successor to the 7 nm process for computer processors. Benefits of smaller transistors in general results from

increases in power and thermal efficiency, and increased transistor density reducing the environmental impact of computational devices. This could open the door for sophisticated internet-of-things devices further improving quality of life. However, whilst the work presented in this thesis is exciting the realisation of these devices will require significant further work.

# Acknowledgements

*"Ars longa, vita brevis"*

As a child, I had always aspired to be a *"real"* physicist, dreamed of visiting Japan, and hoped that one day I could make a small but measurable contribution to science. Indulging my reveries was the job of my grandparents; encouraging me to follow them, my parents; and guiding them, my supervisor's. I will be forever grateful to my parents for the sacrifices they had made, ensuring I had the opportunity to attend university and a fantastic one at that! I am truly blessed to have the privilege of being supervised by Dave. Always reminding me about the folly of "wabbits", having the patience to listen to my over-caffeinated ideas and just being a fantastic human and teacher.

I am so thankful to Dr. Tsuyoshi Miyazaki for organising trips to NIMS (Japan) and for some very fond memories at Torikichi. Dr. Ayako Nakata was a fantastic mentor, and friend, to me whilst visiting Japan. Always keen to help me navigate Japanese culture and encourage random scientific chats. And for Abe-san, someone who radiates kindness and makes everything run like clockwork. Zamaan, thank you for helping me appreciate my own work, and for some great music conversation.

Back in London. My group-mates Conn O'Rourke, Kane Shenton, Jack Poulton and Jack Baker – TY bros for all the wild discussions and good times! My brothers, Aamar and Mo, you guys always knew how to make me laugh, especially when I needed to. Will Dunn, Ben Shepherd, Josh Thomas-Wilsker and Varun Manthri: You guys have been incredible and I love that you always ask me the hard questions. Finally, working at UCL and the LCN is such a special place, and it is the people within those departments that make them so special: Thank you all for

collectively fostering such a friendly and supportive environment. Without doubt there will be people I know I have forgotten to thank individually, so to all of you, thank you for making my journey so special.

I would like to express my thanks to WPI-MANA for the funding necessary to do my work. Work presented in this thesis required exceptional computational facilities and support staff. I am very lucky to have access to extensive computational resources as a member of the UK Car-Parrinello Consortium (UKCP). These resources include: The UK national high performance computing service, ARCHER via UKCP consortium through EPSRC grant ref EP/P022561/1; The UK Materials and Molecular Modelling Hub partially funded by EPSRC (EP/P020194), accessed via UKCP consortium and funded by EPSRC grant ref EP/P022561/1; LCN resources (Salviati); and UCL local resources (Grace).

"Alea iacta est"

# Publications

Parts of this thesis have been published, or are in preparation for publication, as follows:

**Chapter 3:** Published

David R. Bowler, Jack S. Baker, Jack T.L. Poulton, Shereif Y. Mujahed, Jianbo Lin, Sushma Yadav, Zamaan Raza, and Tsuyoshi Miyazaki. Highly accurate local basis sets for large-scale DFT calculations in conquest. *Japanese Journal of Applied Physics*, 58(10), 2019.

**Chapter 4:** Published

Ayako Nakata, Jack S. Baker, Shereif Y. Mujahed, Jack T. L. Poulton, Sergiu Arapan, Jianbo Lin, Zamaan Raza, Sushma Yadav, Lionel Truflandier, Tsuyoshi Miyazaki, and David R. Bowler. Large scale and linear scaling DFT with the CONQUEST code. *The Journal of Chemical Physics*, 152(16):164112, 2020.

**Chapter 6:** Published

Conn O'Rourke, Shereif Y. Mujahed, and Chathurangi Kumarasinghe. Structural properties of silicon germanium and germanium silicon core shell nanowires. *Journal of Physics: Condensed Matter*, 30, 2018.

**Chapter 5:** In Preparation

Shereif Y. Mujahed, David R. Bowler, Tsuyoshi Miyazaki. Effects of density matrix localisation on: Energy, forces and pressure in $O(N)$ DFT.

**Chapters 7 and 8:** In Preparation

Shereif Y. Mujahed, David R. Bowler, Ayako Nakata, Tsuyoshi Miyazaki. Electronic and mechanical properties of $(2 \times 1)$ reconstructed Si-Ge core-shell nanowires.

# Contents

# List of Figures

# List of Tables

# Chapter 1

# Introduction

Nanostructures, defined as having at least one dimension smaller than 100 nm, exhibit fascinating properties due to their reduced dimensionality as compared to their bulk counterparts [2]. Nanostructures with only one dimension above this threshold are defined as *one*-dimensional and when these structures are hollow they are referred to as *nanotubes*, with their filled analogue called *nanowires*. This reduced dimensionality of nanowires has given rise to some unique electronic [3], optical [4, 5], thermal [6], mechanical [7, 8] and magnetic properties [9–11]. As it will soon become apparent to the reader, the material covered in this thesis will only be applicable to a subset of these properties.

Metal-oxide semiconductor field-effect transistors (MOSFETs), a subset of field-effect transistors (FETs), use an electric field to control the flow of current in electronic devices. Comprised of three terminals (source, gate and drain), FETs control current through application of a voltage bias to the gate, altering the conductivity of the material connecting the source and drain. In the context of computer processors, this "on-off" control forms the basis of their circuit logic. Size reduction of FET devices is one factor which drives computational speed increase, and has historically followed Moore's law. Miniaturisation of planar MOSFETs through improvements in established "top-down" device fabrication techniques have resulted in commercially available devices manufactured on a 7 nm process [12, 13]. Adherence to Moore's Law, via top-down methods, is expected to slow due to fundamental manufacturing issues and diminishing performance/investment ratio since the 14

nm process (two device generations prior) [14]. Thus, new "bottom-up" approaches for the manufacture of FETs have the potential to go beyond the limits of traditional top-down manufacturing techniques.

Silicon nanowires (Si NWs), in particular, are the ideal choice since they provide a perfect interface with the existing Si devices. Si nanowires are frequently grown by the bottom-up vapor-liquid-solid (VLS) method since it readily produces single-crystalline nanowires in large numbers [15]. To briefly decribe VLS; a catalyst (Cat) particle is deposited onto a Si surface, reacting with atoms of the substrate and forming Cat-Si alloy droplets. These droplets then adsorb Si-$H_4$ gas inside the reaction vessel, resulting in a supersaturated state where Si atoms precipitate and a Si NW begins nucleation [1].

VLS grown nanowires have been grown and form single crystalline wires [17, 18], an important consequence of which are the well defined crystal directions they grow along. Both the Young's modulus [19, 20] and band gap [21] have been show to be highly anisotropic. It has been found that nanowire diameter determines their growth direction where $\langle 110 \rangle$ nanowires dominate at diameters between 3-20 nm and $\langle 111 \rangle$ nanowires dominate at diameters $> 20$ nm [22, 23]. Control over growth direction has been proven to be affected by catalyst particle size, where $d_{Cat} < 25$ nm results in $\langle 110 \rangle$ NWs and $d_{Cat} \geq 25$ nm yields $\langle 111 \rangle$ NWs [24]. Further control of nanowire growth direction may be be achieved through pressure control of precursor gases in the reaction vessel [25].

So far we have demonstrated that Si NWs are an excellent candidate for future development of FET technologies, outlining factors which affect their growth and modify their physical properties. Control of carrier concentration is an important factor in the design of FETs, and in the context of semiconductor FETs, is achieved through doping of the material. Dopant atoms may be either *donors*, donating an electron to the lattice, or *acceptors*, removing an electron from the lattice [26, p. 222-226]. Upon an acceptor gaining an electron there is now one fewer electrons to roam the lattice, leaving a positively charged *quasiparticle* called an

[1] For a review of NW growth techniques see Ref. [16]

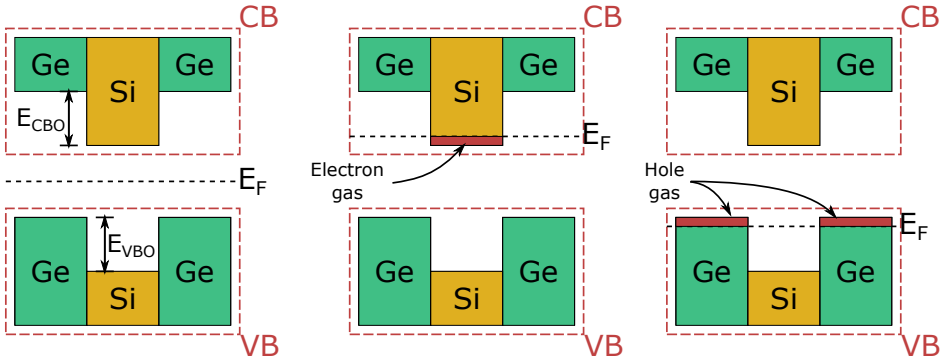


**(a)** Band offsets **(b)** Electron gas formation **(c)** Hole gas formation

**Figure 1.1:** Schematic band diagrams of Si (core) - Ge (shell) nanowires. (a) illustrates the band offsets of valence ($E_{VBO}$) and conduction ($E_{CBO}$) bands, giving rise to an effective confinement potential. A 1D carrier gas will form in the presence of a suitable bias such that the Fermi level ($E_F$) is bent in the direction of: (b) the conduction band resulting in electron gas; or (c) the valence band resulting in hole gas formation.

*electron hole* or simply a *hole*. The energy difference between the dopant energy level and the relevant conduction or valence band edge defines the *ionisation* energy of the dopant atom, and results in either a net positive (donors) or negative (acceptors) charge on the atom [27, p. 136-139]. Considering the motion of charge carriers through this system, these dopant atoms now cause scattering of charge carriers via a Coulomb potential which will negatively affect conductivity.

Reducing the effects of Coulomb scattering may be achieved through heterostructures, where layers of two (or more) materials are grown coherently with one common crystal structure. At the interface of these materials band edges are not aligned, thus band offsets are defined, and in the context of this chapter a good example is Si (core) - Ge (shell) nanowires fig. 1.1. Radial (i.e. core-shell) heterostructures have attracted significant research effort since strain on the nanowire core can be controlled by varying shell growth time [28], offering the ability to produce wires with specific mechanical and electronic properties.

Core-shell NWs are built on from their elemental NW counterparts by ordinary chemical vapour deposition (CVD) of the shell material after VLS growth of the core [29, 30]. It has been observed that Si (core) - Ge (shell) nanowires may be grown with interfaces as sharp as 1 nm [31] and dislocation-free shells [32],

a critical factor in engineering their electronic properties and undesirable surface roughening. The shape of $\langle 110 \rangle$ Si NWs has been shown to be hexagonal [22, 33] for nanowires with a diameter of at least 3 nm, suggesting that core-shell nanowires are at least 4 nm in experimental observations in ideal conditions.

Typically plane-wave DFT investigations of radial heterostructures, where simulation size is limited, have focused on modelling nanowires less than 3 nm without surface reconstructions [34–37]. Reconstructions can have significant effects on the structural [38] and electronic [39, 40] properties of nanowires, which result in metallic and semi-metallic Si nanowires, but have not been explored for core-shell nanowires. Effects on the electronic and mechanical properties of core-shell nanowires due to strain induced by deposition has so far proven elusive, most likely due to limitations of simulation size.

Publications on the electronic and mechanical properties of nanowires have grown rapidly in the last two decades [41], adding pressure to the modelling community to keep pace with their rapid development. Plane-wave DFT calculations are typically carried out on 500 atoms and rarely more that 1000. There is a limited amount of physics that can be squeezed out of a 1000 atom cell, and so truly large-scale simulation methods, such as CONQUEST [42–45], are needed to further this field.

Simulation accuracy is of paramount importance to both the developers of CONQUEST and the wider scientific community. Given the accepted accuracy benchmark of electronic structure methods is considered to be plane-wave methods, we demonstrate CONQUESTs ability to match it in Chapter 3. Calculation of stress is an extremely useful quantity for measuring convergence of structural relaxation simulations and fundamental to NPT molecular dynamics; in Chapter 4 we demonstrate stress implementation in CONQUEST and test its accuracy. Prior to the development of multi-site support functions (covered in Chapter 2), $O(N)$ DFT was the only CONQUEST method suitable for large-scale simulation, however, accurate calculation of stress could be affected by approximations made in $O(N)$ and we quantify these in Chapter 5.

Without the aid of stress, we use $O(N)$ DFT to verify the applicability of Vegard's law to surface reconstructed Si (core) - Ge (shell) nanowires with diameters up to 10.2 nm, and produce bond-direction resolved maps of their local strain environment via a novel method for its calculation in Chapter 6. The Young's modulus and Poisson ratio of Si (core) - Ge (shell) nanowires are determined for diameters of wire 5-9 nm using CONQUESTs non-$O(N)$ method, and comparisons between the previous strain mapping and Vegard's law results, are presented in Chapter 7. Finally in Chapter 8, we calculate the bandstructures, effective carrier masses, band offsets and atomically projected densities of state to establish the connection to strain presented in the previous chapter.

Overall, we present the first comprehensive modelling study of experimentally relevant core-shell nanowires, covering both physical and electronic properties, giving insight into the accuracy and appropriateness of different modelling techniques for these challenging simulations.

# Chapter 2

# Theoretical background

In this chapter we provide a brief introduction to the foundations of density functional theory (DFT). DFT is a powerful approach to *ab initio* prediction of the properties of matter, using quantum mechanics. DFT is a ubiquitous tool in research of the condensed phase, and whilst many excellent books exist on this topic (such as Ref. [46]), there are methods used in this thesis that go beyond those in standard texts. Thus, for the benefit of the reader, and to provide a simplified reference should it be needed, we summarise many of the fundamental concepts and theorems underlying DFT.

## 2.1 The Schrödinger equation and many-body Hamiltonian

The Schrödinger equation is a wave-equation, and the solutions to it describe quantum phenomena. Most undergraduate physicists are able to recall that there are two variables to the wavefunction of a quantum mechanical particle, space and time. Methods in DFT are available to solve the time-dependent Schrödinger equation, aptly named time-dependent DFT (TDDFT), however, whilst CONQUEST has a development branch dedicated to this it is not used in this thesis[1]. So, we will only consider the solutions to the *time-independent* Schrödinger equation, relating the interactions of quantum states to system energy:

[1] For the interested reader, this development is covered in the thesis of Dr. Conn O'Rourke.

$$\hat{H}\Psi(\{\mathbf{r},\mathbf{R}\}) = E\Psi(\{\mathbf{r},\mathbf{R}\}), \tag{2.1}$$

where $\Psi(\{\mathbf{r},\mathbf{R}\})$ is the wavefunction of the coupled system of electrons and nuclei; $E$ the energy; and $\hat{H}$ the Hamiltonian of the system. The Hamiltonian describes the physics of the system, and for our systems of interest, the form is:

$$\hat{H} = \underbrace{-\frac{\hbar^2}{2M_\alpha}\sum_\alpha \nabla_\alpha^2}_{\hat{T}_{ion}} \underbrace{-\frac{\hbar^2}{2m_e}\sum_i \nabla_i^2}_{\hat{T}_{e^-}} + \underbrace{\frac{1}{2}\sum_{\alpha\neq\beta}\frac{Z_\alpha Z_\beta\, e^2}{|\mathbf{R}_\alpha - \mathbf{R}_\beta|}}_{\hat{V}_{ion-ion}} + \underbrace{\frac{1}{2}\sum_{i\neq j}\frac{e^2}{|\mathbf{r}_i - \mathbf{r}_j|}}_{\hat{V}_{Ha}} \underbrace{-\sum_{i,\alpha}\frac{Z_\alpha e^2}{|\mathbf{r}_i - \mathbf{R}_\alpha|}}_{\hat{V}_{e^- -ion}}, \tag{2.2}$$

where $M_\alpha$ is the mass of the ion, $m_e$ the electron rest mass, $Z_{\alpha/\beta}$ the charge of the ion, $\mathbf{R}_{\alpha/\beta}$ the vector position of ionic cores, $\mathbf{r}_{i/j}$ the vector position of electrons and $e$ the charge on an electron.

## 2.2 Born – Oppenheimer approximation

The Born – Oppenheimer approximation [47] is an approach which decouples the electronic and nuclear degrees of freedom in $\Psi(\{\mathbf{r},\mathbf{R}\}) \implies \Psi(\{\mathbf{r}:\mathbf{R}\})$. The mass of a nucleon is almost 2000 times larger than that of an electron, and so the ions can be considered adiabatic [48] since the electrons can be considered to respond instantaneously to changes of nuclear positions. This parametric dependence of the electronic coordinates on the nuclear coordinates allows the calculation of the nuclear kinetic energy to be done separately from the rest of the terms in eq. (2.2), reducing the number of free parameters to be optimised. Using the quasi-classical approximation, i.e. treating the nuclei as classical point charges providing a constant external field to the electrons, the Hamiltonian now "feels" the electrostatic presence of the nuclei frozen in space. The ground-state electronic energy is then determined by the methods described in section 2.7 with respect to the fixed nuclear positions. The nuclear forces are evaluated through the Hellmann – Feynman theorem [49], and the ions moved to minimise the forces on the ions. This process is then repeated until a relaxed structure is established.

## 2.3 Hohenberg – Kohn theorems

The Hohenberg – Kohn theorems [50] formulate density functional theory as an exact theory of many-body systems. The formalism relates a system of interacting particles moving in an effective potential, from which we can define a density of these particles and the energy as a functional of this density. The motivation for this is quite simple; the exact solution of the Schrödinger equation uses a wave-function which has $3 \times (n_{elec.} + n_{nuc.})$ free parameters and minimising the energy of this becomes exponentially difficult as the system size in increased. The relationships established by Hohenberg and Kohn are as follows:

**Theorem 1:** For any system of interacting particles in an external potential, $V_{ext}(\mathbf{r})$, the potential is determined uniquely by the ground state electron density, $n_0(\mathbf{r})$. The Hamiltonian of the system is fully determined, with the exception of a constant energy shift, it follows that we may now define the many-body wave-functions for all states. Hence, all ground state physical properties of the system are defined given only the ground state density $n_0(\mathbf{r})$.

**Theorem 2:** There exists some "*universal functional*" for the energy such that $E[n_0(\mathbf{r})]$ is valid for any $V_{ext}(\mathbf{r})$. The functional $E[n_0(\mathbf{r})]$ is enough to determine the exact ground state energy and density, however, excited states must be determined by other methods.

## 2.4 Kohn – Sham ansatz

The Kohn – Sham ansatz [51] provides an exact mapping of the Hohenberg – Kohn interacting problem to an ancillary system of non-interacting electrons. The Hohenberg – Kohn energy functional is:

$$E[\mathbf{n}] = \int \hat{V}_{ext}(\mathbf{r}) n(\mathbf{r}) d^3r + F[\mathbf{n}], \tag{2.3}$$

although the form of the functional $F[\mathbf{n}]$ is unknown and $\hat{V}_{ext}(\mathbf{r})$ is some general external potential. Kohn and Sham proposed the following functional form, using non-interacting single electron orbitals and electron densities:

$$E_{KS}[\mathbf{n}] = \underbrace{\frac{1}{2}\sum_{i=1}^{N}\int d^3r\,|\nabla\psi_i(\mathbf{r})|^2}_{T_e[\mathbf{n}]} + \underbrace{\int d^3r\,\hat{V}_{ext}(\mathbf{r})n(\mathbf{r})}_{E_{ext}[\mathbf{n}]} + \underbrace{\int d^3r\,\hat{V}_{Ha}(\mathbf{r})n(\mathbf{r})}_{E_{Ha}[\mathbf{n}]} + E_{xc}[\mathbf{n}], \tag{2.4}$$

where $\psi_i(\mathbf{r})$ the wave-function for a single non-interacting electron and all other electron interactions are taken care of in $E_{xc}$ (described in section 2.5). To minimise the energy with respect to $n(\mathbf{r})$, subject to the normalisation condition $\int n(\mathbf{r})d\mathbf{r} = N$ (where $N$ is the number of electrons), yields:

$$\mu = \frac{\delta E_{KS}[\mathbf{n}]}{\delta \mathbf{n}} = \frac{\delta T_e[\mathbf{n}]}{\delta \mathbf{n}} + \frac{\delta E_{ext}[\mathbf{n}]}{\delta \mathbf{n}} + \frac{\delta E_{Ha}[\mathbf{n}]}{\delta \mathbf{n}} + \frac{\delta E_{xc}[\mathbf{n}]}{\delta \mathbf{n}}, \tag{2.5}$$

where $\mu$ is the Lagrange multiplier associated with the normalisation condition. Kohn and Sham adopted the orbital picture, constructing the density from single electron wavefunctions:

$$n(\mathbf{r}) = \sum_{i=1}^{N} |\psi_i(\mathbf{r})|^2. \tag{2.6}$$

From eq. (2.5) we obtain an equation identifying the Kohn – Sham potential:

$$\hat{V}_{KS}[n(\mathbf{r})] = \hat{V}_{ext}[n(\mathbf{r})] + \hat{V}_{Ha}[n(\mathbf{r})] + \hat{V}_{xc}[n(\mathbf{r})] \tag{2.7}$$

which will now enable us to solve the single electron time-independent Schrödinger equation:

$$\hat{H}_{KS}\psi_n = \left(-\frac{\hbar^2}{2m_e}\nabla^2 + \hat{V}_{KS}\right)\psi_n = \epsilon_n\,\psi_n. \tag{2.8}$$

Since the Kohn – Sham potential depends on the density, we have defined a system which must be solved self-consistently. A trial density is constructed, defining the Kohn – Sham potential, allowing us to solve the Schrödinger equation and construct a new density. This process is, in practice, repeated iteratively until we reach some energy tolerance between two consecutive steps.

## 2.5 Exchange - correlation

Section 2.4 introduced $E_{xc}$, and here I will begin by defining what is meant by exchange and correlation;

**Exchange**

The exchange energy is due to the wave function of indistinguishable electrons being subject to exchange symmetry, changing their sign when two particles are exchanged (i.e. antisymmetric).

**Correlation**

Correlation is defined as the difference between the exact solution of the non-relativistic Schrödinger equation and everything else in eq. (2.4), i.e. $E_c = E_{KS} - T_e - E_{I-e^-} - E_{Ha} - E_x$.

The contribution to the total energy of the exchange-correlation term is small, when compared to others, although it is important for describing correct bond properties. There are a diverse range of approximation methods, and within the physics community, the most frequently are: (i) the local density approximation (LDA); and (ii) the generalised gradient approximation (GGA). The LDA method is by far the simplest, approximating the exact XC energy as that of an homogeneous electron gas of the same density, and may be written as:

$$E_{xc}^{LDA}[n(\mathbf{r})] = \int n(\mathbf{r})\, \epsilon_{xc}^{hom.}\, [n(\mathbf{r})] d\mathbf{r}. \tag{2.9}$$

The form of the exchange energy for a homogeneous electron gas is known analytically, and the LDA applies this point-wise to a density that is non-homogenous. Accurate methods of finding correlation energy density utilise quantum Monte Carlo methods [52], and various analytic fitting methods have been proposed [53–56]. The LDA does remarkably well for systems that have a nearly homogeneous electron density which varies slowly, however, in systems such as molecules this is found to be a step too far. Bond geometries and ground state energies were significantly improved with the development of GGA methods [57–61]. The GGA

differs to the LDA by taking into account the gradient of the density at the same point:

$$E_{xc}^{GGA}[n(\mathbf{r})] = \int n(\mathbf{r})\, \epsilon_{xc}\, [n(\mathbf{r}), \nabla n(\mathbf{r})] d\mathbf{r}. \tag{2.10}$$

Potentially more accurate results can be obtained with methods such as meta-GGA [62], which takes into account the second derivative of the density, and hybrid functionals [63–65], which mix in exact exchange (from Hartree-Fock theory) with other sources of XC energy.

## 2.6 Pseudopotentials

The pseudopotential approximates an atomic potential with an effective potential, such that complex effects due to the motion of core (non-valence) electrons are neglected. In this approach only the chemically active valence electrons are dealt with explicitly, while the core electrons are 'frozen', being considered together with the nuclei as rigid non-polarizable ion cores. Outside of some critical radius from the ionic core, $r_c$, the pseudopotential and corresponding pseudo-wavefunction are chosen to follow the all electron potential and wavefunction. Inside $r_c$ the pseudopotential diverges from the correct potential, varying more smoothly and becoming well defined at r=0. This reduces the overall computational cost by removing core electrons from calculations, and when considering plane-wave DFT, the number of plane-waves required to adequately describe the system (see section 2.8).

First-principles pseudopotentials are usually non-local, meaning that different angular momentum states feel different effective potentials, giving a potential operator of the form [66]:

$$\hat{V}_{ps} = \hat{V}_{ps}^{loc} + \sum_{lm} \delta\hat{V}_l |Y_{lm}\rangle\langle Y_{lm}|, \tag{2.11}$$

where $V_{ps}^{loc}$ is the local part, $\delta V_l$ is the semi-local part and $|Y_{lm}\rangle\langle Y_{lm}|$ projects this onto angular momentum and radial states. The form of $\delta V_l$ is specific to the type of pseudopotential used and is only non-zero for $r \leq r_c$. There are a diverse

range of methods for the construction of pseudopotentials, the two most popular being; (i) norm-conserving ; and (ii) ultra-soft. Generally all satisfy these criteria:

1. All-electron and pseudo-valence eigenvalues agree for the atomic reference configuration.

2. All-electron and pseudo-valence wavefunctions agree beyond the cut-off radius $r_c$.

3. Logarithmic derivatives of both wavefunctions coincide at $r_c$.

4. First derivative, with respect to energy, of the logarithmic derivative agree for both wavefunctions for $r \geq r_c$.

Norm-conserving pseudopotentials [67] additionally require the integrated charge, for $r < r_c$, of each wavefunction to be equal. A consequence of this requisite is that the *norm* of the pseudo-wavefunction be identical to the all-electron wavefunction within $r_c$;

$$\langle \phi_l(r) | \phi_{l'}(r) \rangle - \langle \tilde{\phi}_l(r) | \tilde{\phi}_{l'}(r) \rangle = 0, \tag{2.12}$$

where $\phi_l(r)$ is the all-electron state and $\tilde{\phi}_l(r)$ the pseudo-valence state at angular momentum $l$. To ensure transferability and accuracy, small cut-off radii are chosen to sufficiently define core states. This requires a large basis set because electron wavefunctions near the core region are rapidly oscillating due to the orthonormality constraint. Relaxing the condition in eq. (2.12), as proposed by Vanderbilt [68], we may increase the cut-off radius, reducing the basis set size and ensuring smoother ("softer") wavefunctions.

## 2.7 DFT solution methods within CONQUEST

CONQUEST has two modes of operation: (i) exact diagonalisation; and (ii) $O(N)$. Exact diagonalisation exhibits scaling behaviour as $O(N^3)$, where $N$ is the number of atoms, whilst the $O(N)$ method scales linearly with the number of atoms. The

$O(N)$ method has been used for calculations in Chapters 5 and 6 and exact diagonalisation in Chapters 3 to 5, 7 and 8, along with plane-wave calculations in Chapter 3. This chapter will focus on the methods underlying CONQUEST's methods for DFT, however, for the purpose of brevity details of methods involving plane-wave DFT will not be covered in this thesis. There are *many* other places one can find full descriptions of these methods, not entirely different to methods in section 2.7.1, but different enough that an interested reader may like to explore. A personal recommendation would be "Electronic Structure: Basic Theory and Practical Methods" by Martin [46, Ch. 12-13].

### 2.7.1 Exact diagonalisation

One similarity to plane-wave DFT and the diagonalisation method within CONQUEST is the use of *periodic boundary conditions* such that the potential terms in the Hamiltonian are necessarily periodic. This in turn allows for the use of Bloch's theorem,

$$\hat{T}\psi(\mathbf{r}) = \psi(\mathbf{r}+\mathbf{T}) = e^{i\mathbf{k}\cdot\mathbf{T}}u(\mathbf{r}), \tag{2.13}$$

where $\hat{T}$ is a translation operator which translates the Bloch state $\psi(\mathbf{r})$ by the lattice vector $\mathbf{T}$, and $u(\mathbf{r})$ a basis function with the same periodicity as the simulation cell. Here the reciprocal space wavevector $\mathbf{k}$ is restricted to the first Brillouin zone since the phase factor $\exp[i\mathbf{k}\cdot\mathbf{T}]$ in eq. (2.13) is unchanged if a reciprocal lattice vector is added.

Construction of the Hamiltonian matrix elements in real-space is given by,

$$H_{m,m'}(\mathbf{T}) = \int d\mathbf{r}\; u^*_m(\mathbf{r}-\tau_m)\;\hat{H}\;u_{m'}(\mathbf{r}-(\tau_{m'}+\mathbf{T})) \tag{2.14}$$

$m \rightarrow \{\kappa, i, \alpha\}$ is a composite index of $\kappa$ atom types, $i$ atomic index, $\alpha$ the basis index and $\tau_m$ the position of atom $m$. An expression for the Hamiltonian matrix elements in terms of the wavevector $\mathbf{k}$ will enable the Hamiltonian matrix to be represented in terms of Bloch states and is given by,

$$H_{m,m'}(\mathbf{k}) = \int d\mathbf{r}\; u^*_{m\mathbf{k}}(\mathbf{r})\; \hat{H}\; u_{m'\mathbf{k}}(\mathbf{r}) \tag{2.15}$$

$$= \sum_{\mathbf{T}} e^{i\mathbf{k}\cdot\mathbf{T}}\; H_{m,m'}(\mathbf{T}) \tag{2.16}$$

Now that we have an expression for $H_{m,m'}(\mathbf{k})$, finding these matrix elements will require sampling of the Brillouin zone (BZ) by using integration points in reciprocal space called k-points. The most common scheme for sampling the BZ to evaluate these matrix elements is the Monkhorst-Pack [69] method, a scheme of regularly spaced k-points, for structural relaxations. However, band structure calculations will require sampling along special high-symmetry $\mathbf{k}$-vectors from the BZ origin ($\Gamma$-point) along a path of the BZ boundary and back to $\Gamma$. The exact path, and names of the high-symmetry points along the path, is dependent on the crystal structure of the material being modelled and will have to be looked up prior to these types of calculations.

From this point, diagonalisation of the Hamiltonian matrices yield the eigenvalues and eigenstates, which is what we refer to as the *exact diagonalisation* method in CONQUEST. Accurate simulation of materials with this DFT method will require the k-point density used for calculations to be converged such that increases to k-point density result in negligible energy differences. The interested reader should refer to the book "Numerical Recipes: The art of Scientific Computing" [70] for practical implementations of matrix diagonalisation, and the specific implementation used in CONQUEST is part of the SCALAPACK package for optimised computation over many computer processors.

### 2.7.2 Linear scaling DFT

Exact diagonalisation and plane-wave DFT typically scale as $O(N^3)$, where $N$ refers to the number of atoms in the simulation cell, placing a practical limit of around 1000 atoms[2]. Linear scaling DFT utilises Kohn's 'nearsightedness' principle [71],

[2]It will become apparent in Chapters 7 and 8 the use of MSSFs (see section 2.8.2) makes larger simulations of up to a few thousand atoms possible with exact diagonalisation.

which assumes that electronic structure is inherently local and will decay exponentially with distance, i.e. the Kohn – Sham density $n(\mathbf{r},\mathbf{r}') \longrightarrow 0$ as $|\mathbf{r}-\mathbf{r}'| \longrightarrow \infty$. CONQUEST works directly with the density matrix rather than the wavefunctions, and the form of the density is given by:

$$n(\mathbf{r},\mathbf{r}') = \sum_{i\alpha,j\beta} \phi_{i\alpha}(\mathbf{r}) K_{i\alpha j\beta} \phi_{j\beta}(\mathbf{r}'), \tag{2.17}$$

where $K_{i\alpha j\beta}$ is the density matrix element, $\phi_{i\alpha}(\mathbf{r})$ and $\phi_{j\beta}(\mathbf{r}')$ are local support functions centred on atom $i$ and $\alpha$ the support function number on the same atom, rather than the Kohn–Sham eigenstates which extend throughout space. To obtain an expression for the energy we must first define the density matrix,

$$\mathbf{K} = 3\mathbf{LSL} - 2\mathbf{LSLSL}, \tag{2.18}$$

where $\mathbf{L}$ is the auxiliary density matrix and $\mathbf{S}$ is the overlap with $S_{ij} = \langle \phi_i | \phi_j \rangle$. The auxiliary density matrix $\mathbf{L}$ is essentially the $n^{th}$ iteration of $\mathbf{K}$, however the initial guess for $\mathbf{L}$ follows that of Palser & Manolopoulos [72],

$$\mathbf{L}_0 = \frac{\lambda}{2}(\mu \mathbf{S}^{-1} - \mathbf{S}^{-1}\mathbf{H}\mathbf{S}^{-1}) + \frac{1}{2}\mathbf{S}^{-1} \tag{2.19}$$

with $\mu$ the chemical potential, $\mathbf{S}^{-1}$ the inverse overlap matrix and $\mathbf{H}$ the Hamiltonian matrix. The $\lambda$ term given by,

$$\lambda = min\left\{ \frac{1}{H_{max} - \mu}, \frac{1}{\mu - H_{min}} \right\}, \tag{2.20}$$

where $H_{max}$ and $H_{min}$ are the upper and lower bounds of the eigenvalue spectrum of $H$.

To minimise the energy with respect to the density matrix[3] $\hat{\rho}$ two conditions must be met: (i) $\hat{\rho}$ is idempotent, i.e. $\hat{\rho}^2 = \hat{\rho}$; and (ii) $2Tr(\hat{\rho}) = N$, where $N$ is the number of electrons [73, 74]. The condition of idempotency requires the eigenvalues of $\hat{\rho}$ to be either 0 or 1, however, for eigenvalues in the interval $[0,1]$, weak

[3] Here $\hat{\rho}$ is used in place of either $\mathbf{K}$ or $\mathbf{L}$ for simplicity.

idempotency is sufficient to prevent non-physical "run-away" solutions [75]. In CONQUEST, weak idempotency is first achieved through the McWeeny [76] purification of the the density matrix as in eq. (2.18), and then through Li-Nunes-Vanderbuilt (LNV) method [77] for efficient computation of the energy [78]. Writing $E = \mathrm{Tr}[\mathbf{KH}]$, we can use the gradient $\partial E/\partial L_{i\alpha,j\beta}$ to minimise the energy with respect to the density matrix [45].

In the previous section (section 2.7.1) periodic boundary conditions are used such that the interactions of atoms within the simulation cell are interacting with infinitely repeating images of the simulation cell at the cell boundary. This enables the use of Bloch's theorem where the interaction of atoms in the cell with the periodic images are folded in to the cell by the phase factor in eq. (2.13), which effectively treats interactions *implicitly*. However, in $O(N)$ mode, CONQUEST tiles of the simulation cell until the largest matrix range[4] is enclosed within the image cells. CONQUEST then constructs the relevant matrix elements treating the interactions of atoms in the cell and the images *explicitly*, i.e. there is no folding of interactions in to the simulation cell and an atom will interact with all of it's different images. As a result of not folding in the interactions between atoms and their images, no k-points are used (or can be defined) in CONQUEST's $O(N)$ method, and to our knowledge is a unique feature of CONQUEST.

## 2.8 Basis sets

### 2.8.1 Pseudo-atomic orbitals

Real space DFT methods tend to use a basis set which are spatially local such as numerical atomic-like orbitals. They have gained popularity due to efficient algorithms for populating matrix elements, using either all-electron [79] or pseudo-atomic orbitals (PAOs) [80,81]. Both basis functions are written as a radial function multiplied by a spherical harmonic:

[4]The largest matrix range is highly dependent on both the basis set (see Section 2.8 and Chapter 3) and the chosen cutoff range of the density matrix, thus it is not possible definitively inform the reader which matrices will be the largest.

$$\chi_{nlm}(\mathbf{r}) = R_{nl}(r)Y_m^l(\mathbf{r}), \tag{2.21}$$

where $n, l$ and $m$ are the principal, azimuthal and magnetic quantum numbers respectively.

To generate a PAO basis set, we solve the Schrödinger equation for the pseudo-atom using pseudopotentials (see section 2.6). This will result in orbitals with long, exponentially decaying tails. Within solids and molecules, these long-range terms are not really appropriate and can detrimentally effect the accuracy of calculations. Confining the atom within a box by one of two methods: (i) set a cut-off radius such that $\chi_{nlm}(\mathbf{r_c}) = 0$ [82]; or (ii) define a fixed energy shift for each $l$ i.e. the difference between unconfined and confined is $\delta\ \epsilon_l$ [81, 83]. The latter is the method used in CONQUEST and will be discussed further in chapter 3.

With PAOs, there is no method for systematically improving the accuracy. One method for improving the accuracy is to increase the basis set size, but first I will explain what is meant by the size of a PAO. There is some minimal basis set, single-$\zeta$, for which each valence orbital is given one basis function (e.g. Si has four valence electrons, so single-$\zeta$ has 4 basis functions). To increase the size further, there are two approaches: (i) add an extra basis function to each valence orbital; or (ii) add polarisation orbitals. Double-$\zeta$ will have two basis functions per valence orbital, triple-$\zeta$ three etc. Polarisation can be defined in various ways, but for this report we simply add the next higher angular momentum channel to it, so single-$\zeta$ polarisation for Si has 9 basis functions, one s-, three p- and five d-orbitals.

### 2.8.2 Multi-site support functions

The recently proposed "multi-site" support functions (MSSFs) are the linear combinations of pseudo-atomic orbitals the on-site atom and their neighbouring atoms within a finite region [84]. As they correspond to local molecular orbitals (MOs), the multi-site support functions are free from the limitation from the atomic orbital symmetry and can be reduced to the minimal basis size. To determine the linear-combination of coefficients, we apply a localised filter diagonalisation (LFD)

method, originally proposed by Rayson and Briddon [85, 86]. In the LFD method, the linear-combination coefficients are determined efficiently by using the local MO coefficients projected onto localized trial vectors.

Usage of MSSFs requires the specification of two ranges: (i) the MSSF range ($R_{MSSF}$); and (ii) the LFD range ($R_{LFD}$). The MSSF range encircles the atoms, a distance no larger than $R_{MSSF}$ from the central atom, which define the linear combination of PAOs used to construct the support functions for the central atom. The LFD range specifies the distance from the central atom used to update the coefficients of the central atom support functions, and so there is a necessary condition that $R_{LFD} \geq R_{MSSF}$[5]. Whilst it is possible to minimise the total energy through variation of the MSSF coefficients, as in Ref. [87], we do not make use of it in this thesis to save the significant computational cost incurred. Instead, we opt for larger MSSF and LFD ranges which were found to yield excellent results when sufficient neighbouring atoms are included in MSSF construction [84].

### 2.8.3 Plane-waves

Within the solid-state physics community, DFT typically uses plane-wave basis sets to build the Kohn – Sham orbitals, see eq. (2.22). Plane-wave basis sets have been used largely because: (i) the accuracy can be systematically improved; and (ii) forces can be calculated without Pulay corrections because the basis set is independent of atomic positions (although a change in unit cell geometry will introduce Pulay *stress* terms). The accuracy can be improved by increasing the energy cutoff, $E_{cut}$, which is directly proportional to $G_{max}$ (the largest lattice point vector in reciprocal space) and thus the number of plane-waves.

$$u_{m,\mathbf{k}}(\mathbf{r}) = \sum_{|\mathbf{G}+\mathbf{k}|<G_{max}} c_{m,\mathbf{k}}(\mathbf{G}) e^{i\mathbf{G}\cdot\mathbf{r}} \tag{2.22}$$

[5]The interested reader should first read Ref. [84] to develop a more detailed of the MSSF methodology as implemented in CONQUEST.

# Chapter 3

# PAOs and accuracy

## 3.1 Introduction

The importance of DFT beyond the context of computational physics needs little introduction. In excess of 15,000 publications are published each year [88] dependent on search criteria[1], with the largest research topic being physical chemistry according to the Web of Science Core Collection (August 2020). Usage cases vary widely too, ranging from electronic structure prediction of novel solids to crystal structure prediction of both organic and inorganic compounds. In both instances, these *ab initio* results act as a baseline for the analysis of experimental data and planning future experiments.

More recently, DFT calculations have been used to build large databases [89–91] and carry out multi-scale simulation in which they serve as one part of the process chain [92–94]. The precision of DFT codes therefore determines the credibility and reproducibility of many growing areas of research, and so, it has implications reaching far beyond electronic structure research.

The electronic structure community have safeguarded the future of DFT, taking the first steps toward ensuring the accuracy and reproducibility of DFT with the first "delta" study [95, 96]. By comparing equation of state results from a variety of different DFT codes and pseudo-potential methods to those of highly accurate all-electron codes they were able to quantify a so-called "Δ-gauge". The Δ-gauge is

[1] Figure quoted uses search terms "density functional theory" or "DFT".

the average relative difference between a set of all-electron calculations and those of pseudo-potential based DFT codes for 71 elemental solids.

In light of this study, we too should like to validate the accuracy and transferability of CONQUEST basis sets. In section 3.2 we shall present two methods for the generation of pseudo-atomic orbitals, one of two basis function types available to CONQUEST users. In section 3.3 we present results for two bulk crystal structures: (i) the cubic perovskites $PbTiO_3$ and $SrTiO_3$; and (ii) zinc-blende structures of GaN and GaAs. We compare these, in a similar fashion to the "delta-study" paper of Lejaeghere *et al* [96], using the data from equation of states fitting from *both* CONQUEST and plane-wave calculations. Next, section 3.4 compares CONQUEST geometry relaxations of molecules to those found by plane-waves using the metrics of bond lengths, angles and dihedral angles were applicable. At the end of each of these sections we shall discuss the merits and failures of our PAO basis sets, culminating in the over-arching section 3.5 where we shall give an overview of our findings and suggest further work.

## 3.2 Methodology

Tremendous effort has been placed in developing linear scaling approaches to DFT [97, 98] which have been shown capable of calculations on millions of atoms [99, 100]. In order to do so, a localised density matrix must be defined. In the context of CONQUEST we have two methods for defining basis functions: (i) blips; and (ii) pseudo-atomic orbitals. The former method is beyond the scope of this thesis, and a full description of PAOs can be found in section 2.8.1.

However, in section 2.8.1 we have neglected three questions: (i) What should be the largest angular momentum included?; (ii) how are radial functions calculated?; and (iii) How many basis functions should there be for each $n, l$ quantum number pair?

Question (i) is determined by the valence electrons included in the pseudo-potential since these angular momenta must be represented in the basis. In addition to the valence electrons in the pseudo-potential we consider the use of polarisation

functions to add basis flexibility and achieve well converged results. One can define a polarisation orbital by solving for an orbital with higher angular momentum than the valence electrons, however these tend to be unbound. Instead, we define these polarisation orbitals in a similar fashion to those of SIESTA [83] where the highest occupied orbital is polarised by a small electric field $\mathscr{E}$ along the z-direction. Using first-order perturbation theory,

$$(H-E)\delta\phi = -(\delta H - \delta E)\phi \tag{3.1}$$

where $\delta H = \mathscr{E} z$ and $\delta E = \langle\phi|\delta H|\phi\rangle = 0$ since $\delta H$ is odd. Owing to selection rules this yields a perturbed orbital with $l' = l \pm 1$, from which we chose the $l+1$ orbital since we already have lower angular momenta orbitals within the basis.

Localisation of PAOs is of paramount importance and the methods used to do so will have a direct effect of the quality of the basis used in the calculations. It is well-known that atomic-like orbitals in molecules and solids yield the best results when the orbital range is shorter than those of a free atom [101]. Binding in molecules or solids is driven by a reduction in the total energy, which in turn is afforded through the electrons being closer to nuclei without requiring as much kinetic energy as those of free atoms. Artacho *et al* present a method such that a single parameter, an energy-shift $\Delta E$, may define the confinement radii [102]. This energy-shift is the energy increase that each orbital experiences when confined to a finite sphere as compared to the free atom solution. In doing so we have a consistent, physically motivated definition of confinement.

For large-scale DFT codes such as CONQUEST and SIESTA, radial basis functions are solutions to the Kohn – Sham Hamiltonian for an isolated pseudo-atom in spherical boundary conditions, a method originally pioneered by Sankey and Niklewski [82]. The Sankey – Niklewski method enforced locality by an arbitrary cut-off distance $r_c$ beyond which $\phi(r \geq r_c) = 0$, however, the method for choosing a cut-off is not intuitive. A smaller cut-off will offer the greatest gain in efficiency, compared to larger cut-offs, since it can increase the number of elements in the overlap matrix equal to zero, increasing matrix sparsity and thus benefitting algorithms

where sparsity is key. Although, this may be at the cost of accuracy, especially in systems where long-ranged effects or weak interactions are significant.

As a result of the information presented above, two ideas[2] for the construction of well confined basis functions are tested: (i) equal spacing of confinement energies; and (ii) equally spaced confinement radii [103]. Confinement by equal energy spacing employs the energy-shift method in Artacho *et al* [102]. Practically, for a single zeta (SZ) and SZ plus polarisation (SZP) basis a single energy-shift value (default of 20 meV) is used to determine the confined orbital. For two radial functions, two energy-shifts are used (default 2000 meV and 20 meV); and for three basis functions a third intermediate value (defaults 2000, 200 and 20 meV) are used.

The equal radii method redefines the extent of the radial functions found from equal energy. For all basis functions confined to a given energy shift, the radial extent of those orbitals is found and an *unweighted average* of their extent in space determined. This average radial extent is now used as a spatial cutoff for a given confinement energy and the basis set is recalculated. Polarisation orbitals are excluded from the averaging proceedure. This is because they inherit their radial extent, regardless of confinement method used, from the highest energy $n,l$ orbital [83, 102, 103] and including them in the averaging procedure will bias the basis toward the highest energy $n,l$ orbitals[3]. Figure 3.1 provides a more intuitive, graphical representation of the process for defining the equal radii method.

The equal energy confinement results in basis functions with irregular extents, i.e. for a given confinement energy all $n,l$ pairs will have different extents in $r$ (see fig. 3.1(a)). In contrast the equal radii method will produce orbitals with regular spacing in $r$, for a given confinement "energy"[4], and will generally produce more tightly confined orbitals (see fig. 3.1(b)). So, the equal radii method has the advantage of being more computationally efficient owing to increased (and more regular) sparsity patterns of matrices used in CONQUEST, however, they may require a finer

[2]These ideas were formulated and implemented by Prof David R. Bowler.

[3]Whilst it wouldn't necessarily be incorrect to do this, we have chosen to bias toward the occupied orbital states.

[4]We use "energy" here since the actual confinement energy of the radially averaged orbital will not correspond to an exact 20, 200 or 2000 meV energy shift.

integration grid due to the increased compression of more diffuse orbitals.

Finally, in answer to question (iii) above, the choice is complex. In CONQUEST's $O(N)$ method, using a basis set larger than a single radial and single polarisation orbital per $n,l$ pair (SZP), it could result in a failure to invert the overlap matrix. This is because we create an approximate $\mathbf{S}^{-1}$, with linear scaling, by enforcing a sparsity pattern and using Hotelling's method[5]. When a basis is larger than SZP this results in *ill-conditioning* of $\mathbf{S}^{-1}$. At present, it is not known if this ill-conditioning can be overcome with a change in the methodology and is beyond the scope of this thesis, so $O(N)$ will not be used in this chapter. However, for exact diagonalisation the choice is somewhat arbitrary and related to the desired accuracy, which we shall quantify in this chapter along with the accuracy of the two confinement methods presented above.

Our motivation in this chapter is to test the PAOs produced by CONQUEST as compared to plane-wave results. To maintain direct comparability between results we have made use of the PWSCF suite of QUANTUMESPRESSO [104] which reads the same pseudopotentials as CONQUEST. PBESol [105] pseudopotentials were used for the investigation of GaN, GaAs, $SrTiO_3$ and $PbTiO_3$ since they are considered generally better for solids, whilst we used regular PBE [60] pseudopotentials for the rest of the results. We used the LIBXC library [106] for the generation of basis sets and CONQUEST calculations.

[5] An iterative method where $\mathbf{S}^{-1} = \lim_{n\to\infty} \mathbf{X}_n$ using $\mathbf{X}_0 = \mathbf{I}$ and $\mathbf{X}_{n+1} = 2\mathbf{X}_n - \mathbf{X}_n\mathbf{S}\mathbf{X}_n$. In practice this method is terminated when a specified residual is reached.

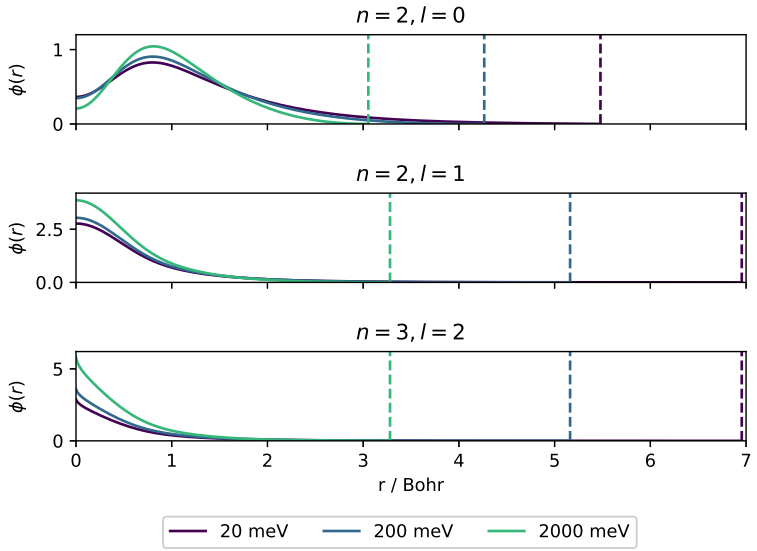


**(a)** Energy method.

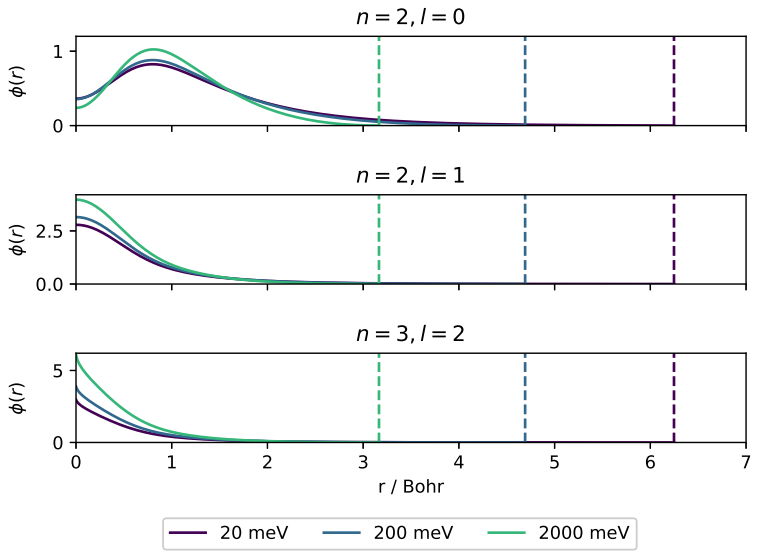


**(b)** Radii method.

**Figure 3.1:** Plots of the resultant PAOs, $\phi(r)$, produced by the confinement methods of either: (a) equal energy; or (b) equal radii. The plots above show the 2s and 2p valence orbitals of a PBE pseudopotential C atom, with the 3d polarisation orbitals included. Notice how all equal radii zetas for a given energy confinement (see legend), specifically the 2s and 2p orbitals in (b), have the same extent in real space? The extent of PAOs generated by the equal radii method is determined by the *average* extent of equal energy based PAOs, for a given confinement energy, i.e. all 200 meV energy based PAOs (excluding polarisation orbitals) have their extent averaged to yield the extent of the equal radii PAOs. This average radial extent then sets the cutoff for all "200 meV" equivalent equal radii PAOs. Labels for the $n$ and $l$ quantum numbers are shown above their graphs, and dashed vertical lines in the plots indicate the cutoff radius of the PAO.

## 3.3 Bulk systems

Electronic structure calculations are most commonly associated with simulation of the condensed phase, so to provide insight into the accuracy of our basis set methodology in the context of bulk materials with cutting edge device technologies we have chosen GaN, GaAs, $SrTiO_3$ and $PbTiO_3$ as our systems of interest. GaN and GaAs are prototypical, III - V direct gap semiconductors with applications to light emitting diodes and transistors, specifically GaN has been identified as an excellent candidate for THz devices [107]. An abundance of physical phenomena have been observed in $ABO_3$ perovskites, many of which are subject to distortions to the structure formed during growth. To accurately simulate these structures requires many thousands of atoms [108], therefore well beyond the capabilities of traditional plane-wave DFT codes.

Table 3.1 presents the results of our work on the cubic perovskites. $SrTiO_3$ (STO) lattice parameter results for equal radii generally perform better than their equal energy counter-parts compared to plane-wave results[6], and the same is true for $PbTiO_3$ (PTO). Bulk modulus energy method results for STO show no specific pattern of convergence to plane-wave results, although we note that the addition of a more tightly confined radial basis functions had the most significant effect. This may indicate that orbitals responsible for STO elastic characteristics are loosely confined[7]. Bulk modulus results for STO using the equal radii method suggest it is unsuitable for calculating the elastic properties of STO due to the necessity of irregular radial functions for accurate calculation.

Bulk modulus results for energy-based method PTO results share similarity with results in STO, demonstrating that the higher confinement basis functions for DZP take the bulk modulus further away from plane-wave results whilst the addition of an intermediate restores some of the "loose-ness" required to adequately describe the elastic properties. As is evident in table 3.2 the radial confinement method

[6] All plane-wave calculations of the cubic perovskites presented in our paper [103] and this thesis were carried out by Jack S. Baker whilst CONQUEST calculations were done by the author of this thesis.

[7] Table 3.2 shows the omission of *d*-orbital states for Sr, an oversight that has since been corrected, and may explain the results for STO.

| | Basis | $SrTiO_3$ | | $PbTiO_3$ | |
|---|---|---|---|---|---|
| | | $V_0$(Å$^3$) | $B_0$(GPa) | $V_0$(Å$^3$) | $B_0$(GPa) |
| QUANTUM ESPRESSO | PW | 58.79 | 186.4 | 60.14 | 191.1 |
| CONQUEST (Energy) | SZ | 61.39 | 187.0 | 61.66 | 191.2 |
| | SZP | 60.76 | 182.6 | 61.44 | 183.0 |
| | DZP | 60.52 | 180.0 | 61.06 | 186.2 |
| | TZTP | 60.08 | 183.4 | 60.83 | 187.8 |
| CONQUEST (Radii) | SZ | 60.54 | 192.7 | 61.00 | 203.3 |
| | SZP | 60.99 | 170.0 | 61.66 | 189.2 |
| | DZP | 60.15 | 180.7 | 60.69 | 190.9 |
| | TZTP | 59.67 | 169.9 | 60.62 | 190.3 |

**Table 3.1:** Comparision of the optimal lattice volumes and bulk moduli for cubic perovskites strontium titanate and lead titanate. Plane-wave calculations used a plane-wave cutoff of 42 Ha owing to the "hard" pseudopotentials of oxygen and titanium. CONQUEST calcuations used an integration grid cutoff of 350 Ha. All calculations used a 9×9×9 Γ-centred Monkhorst-Pack k-point mesh.

brings up the average value for the 5$d$-orbital, negatively impacting the SZ basis where variational freedom of the energy is poorest. This indicates the 5$d$-orbital is expected to dominate the description of PTO elastic properties.

For GaN (see table 3.3) SZ lattice results show that both methods perform poorly with the equal radii method performing the worst, whilst the equal energy method SZP results demonstrate a marked improvement over the equivalent equal radii result. Analysis of the basis in table 3.4 indicates the poor results of the radii method are due to the 3$d$-orbitals being under-confined and 4$p$-orbitals over-confined. Larger basis sets show a similar lattice parameter performance for both confinement methods afforded by greater variational freedom. Bulk modulus results are generally poorly approximated by the equal energy confinement method, indicating the Ga 4$s$-orbital plays a pivotal role in the elastic properties of GaN. GaAs results show that both methods benefit from an increase in variational freedom and require more tightly confined basis functions for accurate results.

| n | l | Energy | | | Radial | | |
|---|---|---|---|---|---|---|---|
| 5 | d | 4.46 | 3.51 | 2.61 | 6.85 | 5.34 | 3.78 |
| 6 | s | 6.54 | 5.21 | 3.87 | 6.85 | 5.34 | 3.78 |
| 6 | p | 9.57 | 7.19 | 4.85 | 6.85 | 5.34 | 3.78 |
| 6 | d | 9.57 | 7.19 | 4.85 | 6.85 | 5.34 | 3.78 |

**a** Pb basis

| n | l | Energy | | | Radial | | |
|---|---|---|---|---|---|---|---|
| 4 | p | 4.94 | 3.94 | 2.96 | 7.95 | 6.19 | 4.38 |
| 5 | s | 10.98 | 8.34 | 5.83 | 7.95 | 6.19 | 4.38 |
| 5 | p | 10.98 | 8.34 | 5.83 | 7.95 | 6.19 | 4.38 |

**b** Sr basis

**Table 3.2:** Ranges of the support functions for Sr and Pb for both energy confinement and average radii methodologies with length units quoted in Bohr. Note there are three basis functions for each $n,l$ quantum number pair, this corresponds to a TZTP basis. The first column for each method corresponds to a confinement energy of 0.02 eV, the second 0.2 eV and the third 2 eV. To obtain values for any size of basis the range does not change, instead you choose the appropriate values by the rules given in section 3.2.

| | Basis | GaN | | GaAs | |
|---|---|---|---|---|---|
| | | $V_0$(Å$^3$) | $B_0$(GPa) | $V_0$(Å$^3$) | $B_0$(GPa) |
| QUANTUM ESPRESSO | PW | 91.10 | 187.5 | 181.47 | 68.8 |
| CONQUEST (Energy) | SZ | 96.03 | 167.1 | 195.65 | 57.3 |
| | SZP | 93.80 | 176.1 | 189.93 | 60.7 |
| | DZP | 92.83 | 181.7 | 183.34 | 69.4 |
| | TZTP | 92.59 | 178.7 | 183.22 | 68.1 |
| CONQUEST (Radii) | SZ | 96.87 | 169.6 | 196.31 | 55.7 |
| | SZP | 95.24 | 169.8 | 193.91 | 58.5 |
| | DZP | 92.88 | 187.2 | 182.69 | 68.3 |
| | TZTP | 92.14 | 185.4 | 183.16 | 69.5 |

**Table 3.3:** GaN and GaAs: Comparison of optimal lattice volumes and bulk moduli. QUANTUM ESPRESSO calculations were performed with a plane wave cutoff of 42Ha and CONQUEST with an integration grid cutoff of 350Ha. All calculations used a Γ-centred Monkhorst-Pack k-point mesh, for GaN we used a 9×9×9 and GaAs used a 7×7×7 mesh.

| n | l | Energy | | | Radial | | |
|---|---|---|---|---|---|---|---|
| 3 | d | 3.58 | 2.82 | 2.02 | 6.50 | 5.06 | 3.58 |
| 4 | s | 6.58 | 5.24 | 3.89 | 6.50 | 5.06 | 3.58 |
| 4 | p | 9.41 | 7.07 | 4.77 | 6.50 | 5.06 | 3.58 |
| 4 | d | 9.41 | 7.07 | 4.77 | 6.50 | 5.06 | 3.58 |

**a** Ga basis

| n | l | Energy | | | Radial | | |
|---|---|---|---|---|---|---|---|
| 4 | s | 5.89 | 4.64 | 3.44 | 6.88 | 5.29 | 3.74 |
| 4 | p | 7.94 | 5.96 | 4.07 | 6.88 | 5.29 | 3.74 |
| 4 | d | 7.94 | 5.96 | 4.07 | 6.88 | 5.29 | 3.74 |

**b** As basis

| n | l | Energy | | | Radial | | |
|---|---|---|---|---|---|---|---|
| 2 | s | 4.81 | 3.74 | 2.71 | 5.48 | 4.17 | 2.85 |
| 2 | p | 6.11 | 4.53 | 2.95 | 5.48 | 4.17 | 2.85 |
| 3 | d | 6.11 | 4.53 | 2.95 | 5.48 | 4.17 | 2.85 |

**c** N basis

**Table 3.4:** Ranges of the support functions for Ga, As and N in Bohr. Note there are three basis functions for each $n,l$ quantum number pair, this corresponds to a TZTP basis. The first column for each method corresponds to a confinement energy of 0.02 eV, the second 0.2 eV and the third 2 eV. To obtain values for any size of basis the range does not change, instead you choose the appropriate values by the rules given in section 3.2.

## 3.4 Molecular systems

### 3.4.1 Methane, Silane and Germane

To begin testing the accuracy of our PAOs to plane-wave basis sets we have started with some of the simplest molecules; methane, silane and germane. Silane and germane are often utilised in the growth of nanowires via vapour deposition techniques. Thus, these molecules are of special interest in potential future work for the simulated growth of nanowires using CONQUEST and the nudged-elastic band technique.

There are limited metrics for comparison of such simple molecules, however, as a preliminary step to more detailed comparisons of basis sets we have chosen to compare the average X – H bond length and H – X – H bond angle (see table 3.5). We used a plane-wave cutoff of 41 Ha for these tests. This represents the "normal" precision as per the PSEUDODOJO website (Accessed: 2020/08/26) for C, the hardest element studied. The methodology can be found in Section 5 of Van Setten *et al* [109], summarised by having a total energy difference of $\leq$ 5 meV/atom. For CONQUEST calculations we found that an integration grid cutoff of 200 Ha yielded

| | | QUANTUM ESPRESSO | CONQUEST (Energy) | | | | CONQUEST (Radii) | | | |
|---|---|---|---|---|---|---|---|---|---|---|
| | | | SZ | SZP | DZP | TZTP | SZ | SZP | DZP | TZTP |
| $CH_4$ | $\overline{R}_{C-H}$ (Å) | 1.098 (0.001) | 1.210 (0.000) | 1.145 (0.000) | 1.109 (0.000) | 1.107 (0.000) | 1.207 (0.000) | 1.146 (0.000) | 1.108 (0.000) | 1.106 (0.000) |
| | $\overline{\theta}_{H-C-H}$ (°) | 109.5 (0.1) | 109.5 (0.0) | 109.5 (0.0) | 109.5 (0.0) | 109.5 (0.0) | 109.5 (0.0) | 109.5 (0.0) | 109.5 (0.0) | 109.5 (0.0) |
| $SiH_4$ | $\overline{R}_{Si-H}$ (Å) | 1.500 (0.001) | 1.648 (0.000) | 1.547 (0.000) | 1.502 (0.000) | 1.499 (0.000) | 1.643 (0.000) | 1.548 (0.000) | 1.501 (0.000) | 1.498 (0.000) |
| | $\overline{\theta}_{H-Si-H}$ (°) | 109.5 (0.1) | 109.5 (0.0) | 109.5 (0.0) | 109.5 (0.0) | 109.5 (0.0) | 109.5 (0.0) | 109.5 (0.0) | 109.5 (0.0) | 109.5 (0.0) |
| $GeH_4$ | $\overline{R}_{Ge-H}$ (Å) | 1.537 (0.001) | 1.680 (0.000) | 1.596 (0.000) | 1.544 (0.000) | 1.542 (0.000) | 1.674 (0.000) | 1.598 (0.000) | 1.543 (0.000) | 1.542 (0.000) |
| | $\overline{\theta}_{H-Ge-H}$ (°) | 109.5 (0.1) | 109.5 (0.0) | 109.5 (0.0) | 109.5 (0.0) | 109.5 (0.0) | 109.5 (0.0) | 109.5 (0.0) | 109.5 (0.0) | 109.5 (0.0) |

**Table 3.5:** Average X – H bond lengths ($\overline{R}_{X-H}$) and H – X – H bond angles ($\overline{\theta}_{H-X-H}$) for methane, silane and germane. These simple molecules were calculated *in vacuo* with a minimum separation of 24 Å between periodic images. Plane-wave calculations were performed with a 41 Ha cut-off energy, the "normal" precision rating for C (hardest element) recommended by the PSEUDODOJO website (Accessed: 2020/08/26). For CONQUEST calculations we found an integration grid cutoff of 200 Ha to be adequate to give a total energy tolerance of 1 meV/atom. All structures were relaxed to a force tolerance of 0.0005 Ha/$a_0$ ($\sim$ 0.026 eV/Å).

a total energy difference of $\leq$ 1 meV/atom.

Comparing the average C – H bond length for methane we found a SZ basis set size to give a result within 10% of QUANTUM ESPRESSO results, SZP within 5% and DZP and TZTP within 1%. Si – H bond lengths were found to be within 10% for SZ, approximately 3% for SZP and exact matches for DZP and TZTP basis sets sizes. Ge – H bond lengths were overestimated by SZ basis sets by 9% and 4% for SZP, with the SZ radial confinement basis producing slightly better results compared to the energy confinement method. DZP and TZTP basis sets again yield an exact match with the results produced by QUANTUM ESPRESSO. Bond angles for all DFT codes, basis sets and molecular systems reproduced the expected bond angle of 109.5°, although the plane-waves showed small deviations from the mean values whereas PAOs yielded the correct bond angle exactly.

### 3.4.2 Simple alkanes

As a further test of the accuracy of PAOs, we moved on to alkanes. The alkanes we have simulated are ethane, propane and butane. We have chosen to vary the length

| | | Quantum Espresso | Conquest (Energy) | | | | Conquest (Radii) | | | |
|---|---|---|---|---|---|---|---|---|---|---|
| | | | SZ | SZP | DZP | TZTP | SZ | SZP | DZP | TZTP |
| $C_2H_6$ | $R_{C-C}$ (Å) | 1.527 | 1.597 | 1.538 | 1.530 | 1.528 | 1.591 | 1.538 | 1.530 | 1.525 |
| | $\overline{R}_{C-H}$ (Å) | 1.098 (0.000) | 1.208 (0.000) | 1.148 (0.000) | 1.113 (0.000) | 1.110 (0.000) | 1.206 (0.000) | 1.150 (0.000) | 1.113 (0.000) | 1.109 (0.000) |
| $C_3H_8$ | $\overline{R}_{C-C}$ (Å) | 1.530 (0.001) | 1.588 (0.000) | 1.537 (0.000) | 1.533 (0.000) | 1.529 (0.000) | 1.584 (0.000) | 1.537 (0.000) | 1.532 (0.000) | 1.527 (0.000) |
| | $\overline{R}_{C-H}$ (Å) | 1.099 (0.001) | 1.206 (0.001) | 1.149 (0.001) | 1.114 (0.001) | 1.110 (0.001) | 1.205 (0.000) | 1.151 (0.001) | 1.114 (0.001) | 1.109 (0.001) |
| | $\theta_{C-C-C}$ (°) | 112.1 | 109.2 | 111.9 | 112.3 | 112.3 | 111.8 | 111.9 | 112.3 | 112.3 |
| $C_4H_{10}$ | $\overline{R}_{C-C}$ (Å) | 1.529 (0.001) | 1.582 (0.003) | 1.535 (0.000) | 1.534 (0.002) | 1.529 (0.000) | 1.579 (0.002) | 1.535 (0.000) | 1.532 (0.000) | 1.527 (0.000) |
| | $\overline{R}_{C-H}$ (Å) | 1.100 (0.002) | 1.206 (0.001) | 1.150 (0.001) | 1.115 (0.002) | 1.111 (0.001) | 1.205 (0.000) | 1.151 (0.002) | 1.114 (0.002) | 1.110 (0.001) |
| | $\overline{\theta}_{C-C-C}$ (°) | 113.2 (0.0) | 111.1 (0.4) | 111.8 (0.1) | 113.1 (0.0) | 112.2 (0.0) | 111.2 (0.4) | 111.8 (0.1) | 112.2 (0.0) | 112.2 (0.0) |
| | $\phi_{C-C-C-C}$ (°) | 179.2 | 178.9 | 178.9 | 179.0 | 178.9 | 178.9 | 178.9 | 178.9 | 178.9 |

**Table 3.6:** Accuracy of simulating alkanes with varying chain length. Numbers in brackets underneath values are the standard deviation for the given averaged observable. Plane-wave calculations were performed with a 41 Ha cut-off energy, as recommended by the PseudoDojo website (Accessed: 2020/08/26). Conquest calculations we found an integration grid spacing of 200 Ha to be adequate to give an energy tolerance of 1 meV/atom and thus making the forces reliable to within 1 meV/Å. All structures were relaxed to a force tolerance of 0.0005 Ha/$a_0$ ($\sim$ 0.026 eV/Å).

of the alkane chain since we expect to see variation in the C – C bond lengths and, where applicable, there should be a variation in the bond angles or dihedral angle.

The C – C bond lengths we report in table 3.6 for ethane are very promising. We find that the SZ basis set overestimates the bond length by approximately 4%, with the radial confinement method performing slightly better than the energy based version. Both SZP basis sets found the C – C bond length to within 1% of the converged plane-wave result, with DZP and TZTP replicating the plane-wave result perfectly. The C – H bond lengths for both confinement methods are indistinguishable with SZ giving an overestimate of 11%, SZP 5.5%, and DZP and TZTP approximately 2% as compared to the computed plane-wave result.

Propane C – C bond lengths for Quantum Espresso calculations have quite a large variation in length and comparing with experiment [110] underestimate the bond length by a little over 3% (exp. C – C is 1.53 Å). SZ energy based confinement basis overestimates the C – C bond length by 4% and the radially confined basis by

3%, while both SZP basis overestimate by less than 1%. DZP and TZTP basis give the same result as experiment exactly. Average C – H bond lengths for QUANTUM ESPRESSO calculations underestimate the experimental bond length by 6.5%, with the experimental value being 1.107 Å. For the CONQUEST calculations no significant difference was found between either confinement method. SZ overestimates the experimental bond length by 9%, SZP by 4%, with DZP and TZTP basis near exactly reproducing the experimental bond length.

The reported experimental C – C – C bond angle is 112 ° and we find that the converged plane-wave calculation overestimates this bond angle by approximately 2%. There is a more significant effect of confinement method for the SZ basis sets, with respect to the bond angle, with the energy based confinement underestimating the bond angle by 2.5% whereas the radially confined basis is within 0.2%! For SZP, DZP and TZTP basis sets there is no difference between the confinement method chosen and the bond angles reported in table 3.6 are all within approximately 0.2%, a very good agreement.

The average C – C bond lengths for plane-wave calculations are quite poor when compared to experiment underestimating by nearly 6%. CONQUEST results for this bond length show no dependence on the confinement method used with SZ overestimating by 3%, SZP by 0.6% and DZP/TZTP results reproducing the experimental bond length exactly. C – H bond length for butane is experimentally found to be 1.117 Å. We find that there is a slight dependence on the confinement method used, radial confinement producing slightly better results than those of the energy method. SZ energy confined results are approximately 8% off the experimental value whilst the radial confinement is within 7.5%. SZP results are within 3% for both methods and DZP/TZTP basis sets are than 1%.

C – C – C bond angles for the QUANTUM ESPRESSO results are a little over 1.5% larger than those found by experiment. SZ results for both confinement method underestimate by around 2.5% and SZP by a little under 2%. The energy confined DZP gets the closest to experiment underestimating by a little more than 0.5%, whilst radially confined DZP and both TZTP basis sets underestimate the

angle by just under 1.5%. The dihedral angle specified by the four carbon atoms should be 180° for the ground state and all calculations predict the correct dihedral angle by less than 1%, although plane-wave calculations are the closest to the experimental value.

### 3.4.3 Simple alkenes

The final test for the PAO basis sets was to test them on alkenes, offering particular challenge to transferability where the symmetry about the molecular centres are broken in the case of propene and but-1-ene. Additionally, comparing these alkenes to their alkane counter-part will offer great insight in to the basis set transferability.

The first alkene we've chosen to test is ethene. Being the simplest possible alkene, this will be the most fundamental test for the carbon atom basis if the double bond is well represented. We find a C – C bond length of 1.33Å using plane-wave methods in excellent agreement with the experimental value of 1.329Å. We find no significant difference in the C – C bond length for either of the basis confinement methods, with SZ overestimating by 6.5%, SZP by 3%, DZP by 1.5% and TZTP by 0.75%. C – H bond distance from experiment is 1.082Å. Our plane-wave results underestimate this by 1%. There is very little to distinguish between confinement methods for CONQUEST calculations, the exception being radially confined DZP overestimates the bond length by 2% as compared to the energy method at 3%.

Propene has two distinct C – C bonds, one double and one single. For propene we chose the first C – C bond to be the double bond by fixing the initial distances between pairs of C atoms. We find that there is no significant difference between the confinement methods for these bonds, although, the radial confinement method is slightly closer to the plane-wave result then the energy based method. Both SZ results overestimate the double bond length by 6%, SZP by 3%, DZP a little over 1% and TZTP a little under 1%. For the single C – C bond we find the SZ results show a little more sensitivity to the confinement method used for basis generation, with the energy confinement overestimating the plane-wave result by 5% and the radial method by 4.5%. The rest of the results show very little difference with SZP overestimating by a little under 1.5%, while DZP and TZTP by much less than

0.5%.

C – H bond lengths do not show much sensitivity to the confinement method used for the basis sets, however, again the radial confinement shows a very slight improvement over the energy based method. SZ overestimates the bond length by approximately 10%, SZP by 5% and both DZP and TZTP by less than 0.5%. An important feature of these results are the standard deviation of the C – H bonds. We have chosen the standard deviation to represent the shape of the average C – H bond length distribution. In this regard, the energy based SZ appears to replicate the shape of the plane-wave results well, whilst the radial confinement shows a worse agreement. SZP results contrast these with the radial confinement agreeing more closely than the energy based counter-part, whilst both confinement methods for DZP and TZTP results match exactly with the plane-wave results.

C – C – C bond angles have a stronger dependence on the confinement method for SZ results with energy based SZ underestimating the angle by a little over 2% and radially based by a little under 1.5%. SZP results are extremely close to those found in plane-wave calculations and underestimate by less than 0.2%, whereas the DZP and TZTP basis sets overestimate by about 0.3%. These differences are almost insignificant, although it is interesting that the larger basis sets uniformly over estimate the bond angle. Comparing with the literature, we find the bond angle to be 124.3° [110], so the plane-wave result exactly matches and the errors seen in CONQUEST results are solely due to the basis set.

But-1-ene will present the largest challenge to PAO calculations. Large flexibility in basis set is expected to be required owing to the lack of centrosymmetry. Whilst there are only two types of C – C bonds, three different bond lengths are to be expected since the single-bond closest to the double-bond will be in an environment that has been slightly polarised due to the charge required by the double-bond.

Studying the first C – C (double) bond in table 3.7, we find the radial confinement method uniformly offers results slightly closer to the plane-wave calculations than the energy based counter-parts. SZ basis overestimates the plane-wave result by approximately 6%, SZP a little under 3%, DZP by around 1% and TZTP just

under 1%. The second C – C (single) bond is overestimated by about 4.5% for SZ basis sets, about 1% for SZP, whilst both DZP and TZTP results are less than 0.5%. For the final C – C (single) bond, SZ overestimates by about 4%, SZP by about 0.5% and DZP by less than 0.2%. Curiously, the TZTP results *underestimate* this bond length by less than 0.2%.

C – H bonds are overestimated by 10% for SZ, 5% for SZP, less than 1.5% for DZP and around 1% for TZTP. The first bond angle listed in table 3.7 measures the angle between C – C double bond and the single bond. SZ results vary a little, with the energy based confinement underestimating the angle by abut 4.5% whilst the radial method is closer to 4%. SZP underestimates the angle by about 1.5%, whilst DZP and TZTP overestimate by about 0.5%. The second bond angle is underestimated by just over 2% for SZ, a little over 1.5% for SZP, DZP less than 1% with the radially confined basis slightly closer to plane-wave results. Energy confinemed TZTP exactly matches plane-wave data and the radially confined version less than 0.5%. Results for the dihedral angle vary. The energy confined SZ overestimates by 10% and the radially confined version about 9%. Both SZP methods overestimate by less than 0.2%, DZP by energy about 0.5%, DZP by radii about 1%, TZTP by energy just over 1% and by energy less than 1%.

But-2-ene allows for more direct comparisons of transferability against but-1-ene since the shift in the double bond to the molecular centre changes only the polar environment of the bond. Bonds for C1 – C2 and C3 – C4 are expected to be of equal length and we find that they are within 0.001Å for all results. In all CONQUEST calculations we overestimate these bond lengths. Both SZ basis do so by just about 4.5% with the radial confinement methods performing slightly better. SZP results are a little under 1.5% from the plane-wave results and DZP/TZTP results are less than 0.5% with the TZTP by radii basis near exactly replicating the plane-wave results. SZ results for the C – C double bond are a overestimate the bond length by a little over 5.5%, SZP by a about 2.5%, DZP just over 1% and TZTP just under 1%.

Average C – H bond lengths for SZ are overestimated by about 10% with

the standard deviations a little larger than those of plane-wave calculations. SZP overestimate by about 5%, with radially confined results slightly worse than those by energy. Both DZP and TZTP overestimate these bond lengths by around 1%. The standard deviation for SZP, DZP and TZTP C – H bond lengths agrees with the plane-wave results indicating distribution of the bonds around the molecule are similar.

All calculations predict *trans*-but-2-ene to be the ground-state isomer, as such the dihedral angle expected is 180° which all calculations have correctly predicted. Bond angles between neighbouring carbon atoms are expected to be equal, which the plane-wave calculations have accurately reproduced according to the literature [110]. We find that CONQUEST basis sets consistently underestimate the absolute value of the two C – C – C bond angles. Radial confinement method results are closer to that of plane-waves at smaller basis sets sizes, although the energy confinement results converge to the radial method results.

| | | Quantum Espresso | Conquest (Energy) | | | | Conquest (Radii) | | | |
|---|---|---|---|---|---|---|---|---|---|---|
| | | | SZ | SZP | DZP | TZTP | SZ | SZP | DZP | TZTP |
| $C_2H_4$ | $R_{C-C}$ (Å) | 1.332 | 1.424 | 1.373 | 1.348 | 1.345 | 1.418 | 1.372 | 1.346 | 1.341 |
| | $\overline{R}_{C-H}$ (Å) | 1.090 (0.001) | 1.211 (0.000) | 1.151 (0.000) | 1.106 (0.000) | 1.102 (0.000) | 1.209 (0.000) | 1.153 (0.000) | 1.105 (0.000) | 1.100 (0.001) |
| $C_3H_6$ | $R_{C1-C2}$ (Å) | 1.335 | 1.418 | 1.374 | 1.352 | 1.348 | 1.414 | 1.373 | 1.350 | 1.345 |
| | $R_{C2-C3}$ (Å) | 1.498 | 1.573 | 1.518 | 1.502 | 1.500 | 1.568 | 1.517 | 1.501 | 1.498 |
| | $\overline{R}_{C-H}$ (Å) | 1.095 (0.004) | 1.210 (0.003) | 1.151 (0.001) | 1.110 (0.004) | 1.107 (0.004) | 1.208 (0.002) | 1.153 (0.002) | 1.110 (0.004) | 1.105 (0.004) |
| | $\theta_{C-C-C}$ (°) | 124.3 | 121.5 | 124.1 | 124.7 | 124.6 | 122.5 | 124.2 | 124.7 | 124.7 |
| 1-$C_4H_8$ | $R_{C1-C2}$ (Å) | 1.336 | 1.416 | 1.374 | 1.352 | 1.348 | 1.412 | 1.373 | 1.350 | 1.345 |
| | $R_{C2-C3}$ (Å) | 1.500 | 1.567 | 1.519 | 1.507 | 1.505 | 1.565 | 1.520 | 1.505 | 1.502 |
| | $R_{C3-C4}$ (Å) | 1.536 | 1.597 | 1.542 | 1.539 | 1.535 | 1.596 | 1.544 | 1.538 | 1.534 |
| | $\overline{R}_{C-H}$ (Å) | 1.096 (0.004) | 1.207 (0.001) | 1.150 (0.002) | 1.112 (0.004) | 1.108 (0.004) | 1.206 (0.001) | 1.153 (0.003) | 1.111 (0.004) | 1.106 (0.004) |
| | $\theta_{C1-C2-C3}$ (°) | 125.7 | 120.1 | 123.7 | 125.9 | 126.3 | 120.5 | 124.0 | 126.1 | 126.2 |
| | $\theta_{C2-C3-C4}$ (°) | 111.7 | 109.2 | 110.4 | 112.7 | 111.7 | 109.1 | 110.3 | 112.3 | 112.2 |
| | $\phi_{C-C-C-C}$ (°) | 240.7 | 265.4 | 241.3 | 239.5 | 238.0 | 263.2 | 241.2 | 238.1 | 238.7 |
| 2-$C_4H_8$ | $R_{C1-C2}$ (Å) | 1.498 | 1.569 | 1.519 | 1.504 | 1.501 | 1.564 | 1.518 | 1.503 | 1.499 |
| | $R_{C2-C3}$ (Å) | 1.338 | 1.413 | 1.373 | 1.354 | 1.349 | 1.410 | 1.373 | 1.352 | 1.347 |
| | $R_{C3-C4}$ (Å) | 1.497 | 1.569 | 1.519 | 1.504 | 1.501 | 1.565 | 1.518 | 1.503 | 1.498 |
| | $\overline{R}_{C-H}$ (Å) | 1.098 (0.002) | 1.210 (0.004) | 1.151 (0.002) | 1.113 (0.002) | 1.109 (0.002) | 1.209 (0.003) | 1.154 (0.002) | 1.113 (0.002) | 1.108 (0.002) |
| | $\theta_{C1-C2-C3}$ (°) | 125.3 | 121.7 | 124.0 | 124.5 | 124.4 | 122.1 | 124.1 | 124.5 | 124.4 |
| | $\theta_{C2-C3-C4}$ (°) | 125.3 | 121.4 | 123.6 | 124.3 | 124.3 | 121.7 | 123.6 | 124.3 | 124.4 |
| | $\phi_{C-C-C-C}$ (°) | 180.0 | 180.0 | 180.0 | 180.0 | 180.0 | 180.0 | 180.0 | 180.0 | 180.0 |

**Table 3.7:** Comparison of average X – H bond lengths ($\overline{R}_{X-H}$) and H – X – H bond angles ($\overline{\theta}_{H-Ge-H}$) between Quantum Espresso and all default Conquest set sizes. Plane-wave calculations were performed with a 41 Ha cut-off energy, as recommended by the PseudoDojo website (Accessed: 2020/08/26). Conquest calculations we found an integration grid spacing of 200 Ha to be adequate to give an energy tolerance of 1 meV/atom and thus making the forces reliable to within 1 meV/Å. All structures were relaxed to a force tolerance of 0.0005 Ha/$a_0$ ($\sim$ 0.026 eV/Å).

## 3.5 Concluding remarks

The purpose of this chapter was to assess: (i) if an arbitrary increase in basis size generally yielded better results; and (ii) to test a novel method for basis generation. Plane-wave calculations guarantee higher accuracy for an arbitrary increase in basis size, i.e. they are systematically improvable. PAOs are discrete, and as such, an arbitrary increase in basis size *does not* guarantee systematic convergence. For molecular systems we find that arbitrary increases in the basis size do perform better than a minimal basis set size, in particular DZP and TZTP results are closest to those found by plane-wave calculations. Furthermore, differences between the equal radii

and energy basis set approaches are minimal for the molecular systems under study.

Bulk systems, however, do not necessarily guarantee better results, e.g. SZ equal energy results for perovskites in table 3.1, although in those particular instances we attribute this to fortuitous tuning. In general, we do find that for an untested system larger basis sets are required and that DZP offers the best trade-off between accuracy and calculation time. When comparing the performance between equal radii and equal energy methods one important consideration is the identification of tightly or loosely confined states, and the magnitude of the difference between them.

Averaging effects of the equal radii method have been found to work both in favour of (spontaneous tuning) and against the method. In the context of the wider sampling in our paper [103], we find that the equal radii method gives better results overall. In light of the results presented in this chapter, it must be stressed that basis sets *should* be tested and a significant result of this chapter (not the paper) is that the comparison between plane-wave results and *both* confinement methods enables us to pin point states which may impact results. Moving forward, on-the-fly basis coefficient optimisation is implemented in CONQUEST and further studies using both confinement methods would be of particular interest. Doing so could enable us to produce high quality basis sets optimised for either calculation efficiency or accuracy.

# Chapter 4

# Implementing stress in CONQUEST

## 4.1 Introduction

Simulations of molecules, liquids and solids are often studies of atomic position and simulation cell variations; determining the dynamics or minimising the total energy of the system. Pressure is an important concept in the characterisation of states in condensed matter [111–113]; a state of a system is specified by the total energy, forces on each atom and pressure. Furthermore, a system is considered to be in equilibrium if: (i) the force on each individual atom is zero; and (ii) the macroscopic stress is equal to the externally applied stress. In this chapter we build on previous work implementing forces in CONQUEST [114, 115] which will be necessary for the implementation of stress and pressure. We present verification of stress implementation by comparison of the implemented stress calculations with those from finite differences.

Prior to the pioneering work of Nielsen and Martin [116], all DFT calculations used force criteria to define the equilibrium state of a material. Indeed, this does define *an* equilibrium state, however, the *physical* state must be assumed, i.e. the crystallographic phase at a given temperature and pressure. In this seminal paper they present a general method defining the stress tensor, derived from the quantum virial theorem, and demonstrate their method through calculations of the elastic properties of bulk Si with a plane-wave basis and exchange – correlation handled with the local density functional. A later paper shows a more detailed derivation

of the stress, with explicit terms for ion-ion, pseudopotential, Hartree, exchange – correlation and electronic kinetic energies [117, 118]. Their final paper gives a single expression for total stress, grouping terms in a form for practical calculation of stress in Fourier space as shown by Ihm, Zunger and Cohen [119, 120], demonstrating the efficacy of their method with calculations on Si, Ge and GaAs [121].

The stress theorem, presented in the Nielsen and Martin papers above, was derived and implemented in the context of a plane-wave basis set. Feibelman reformulated the stress theorem from plane-waves to local orbitals in the context of the linear combination of atomic orbitals (LCAO) formalism [122]. His motivation for deriving stress equations in an LCAO basis were two-fold: (i) plane-wave DFT required *many* plane-waves for accurate calculations of second row elements and transition metals[1]; and (ii) LCAO total energy derivatives are exact for a given basis with respect to the simulation cell.

This final point is a reference to the Pulay corrections of forces, a detailed discussion of which can be found in section 4.2. In brief, Pulay corrections of forces are required for basis functions which move with the atoms, which do not apply in a plane-wave basis. However, the total energy in plane-wave DFT calculations is often not converged with respect to simulation cell size. So, if the simulation cell changes, the number of plane-waves required to maintain the same energy tolerance will change. Thus, stress calculation will either require: (i) more (fewer) plane-waves if the simulation cell becomes larger (smaller); or, corrections such as those proposed by Francis & Payne [123] or Rignanese *et al* [124]. Both require additional computational effort, however, for the corrections this is *considerably* reduced in comparison to an increase in the plane-wave cut-off energy.

### 4.1.1 What is stress?

Following references [45, 83, 116], we define the *internal* stress as,

$$\sigma_{\lambda\mu} = \frac{\partial E^{KS}}{\partial\, \epsilon_{\lambda\mu}} \tag{4.1}$$

[1]The author does not elaborate on this point but we assume this is due to the use of norm-conserving pseudopotentials and rapidly varying potentials near the pseudo-core region.

where $\lambda$ and $\mu$ are the Cartesian coordinate indices, and $\epsilon$ denotes the strain. Pressure is the volume-averaged internal stress, defined as $\bar{\sigma}_{ab} = \tau_{ab}/\Omega$ where $\tau$ is the internal stress and $\Omega$ the volume of the cell [45, 83, 116]. It is important to note that cell optimisation of lattice vectors parallel to the direction of the vacuum gap, using either stress or pressure, without appropriate restriction(s) on the lattice vectors will lead to spurious results.

To obtain formulae for stress we must have some expressions for strain, since we shall need derivatives with respect to it as per eq. (4.1). During deformation, all vector positions change with respect to,

$$r'_\lambda = \sum_{\mu=1}^{3} (\delta_{\lambda\mu} + \epsilon_{\lambda\mu}) r_\mu \tag{4.2}$$

The derivative with respect to $\epsilon_{\lambda\mu}$:

$$\frac{\partial r_\nu}{\partial\, \epsilon_{\lambda\mu}} = \delta_{\nu\lambda} r_\mu,$$

Using eq. (4.1) and the product rule for differentiation, we express stress as derivatives of energy with respect to strain and position (with some exceptions described below),

$$\begin{aligned}
\sigma_{\lambda\mu} &= \frac{\partial E^{KS}}{\partial\, \epsilon_{\lambda\mu}} \\
&= \frac{\partial E^{KS}}{\partial r_\nu} \frac{\partial r_\nu}{\partial\, \epsilon_{\lambda\mu}} \\
&= \frac{\partial E^{KS}}{\partial r_\nu} \delta_{\nu\lambda} r_\mu \\
&= \frac{\partial E^{KS}}{\partial r_\lambda} r_\mu
\end{aligned} \tag{4.3}$$

The final equation illustrates how stress is equivalent to a force scaled by a position vector, a delineation we will make thorough use of in this chapter, producing stress equations from existing force contributions. If we consider some volume element of a material, there are forces with two distinct characters: (i) those acting

within the volume; and (ii) those acting on the element surface. The latter is the stress and this is what distinguishes it from the force.

Whilst eq. (4.3) is true for *most* contributions to the stress, there are three exceptions. First, electrostatic integrals in reciprocal space where there are $1/|\mathbf{r}-\mathbf{r}'|$ terms in the integrand, addressed in sections 4.3 and 4.4. Second, changes in the volume per grid point affecting quantities calculated by integration on the grid (i.e. local, Hartree and XC energies), these terms require the Jacobian of the transform in eq. (4.2). The third difference involves part of the GGA contribution where the density is deformed $n(\mathbf{r}) \rightarrow n(\mathbf{r}')$, and so gradients thereof will change and are discussed in section 4.5.

## 4.2 Energy, forces and stresses in CONQUEST

Use of eq. (4.3) makes stress calculation seem a relatively straightforward transition from the forces, with exceptions as stated above. Methods for force evaluation in CONQUEST have been published previously [114] and we shall review them in this section to establish explicit connections to stress.

For a system of atoms with coordinates $\mathbf{R}_i$ and energy $E(\mathbf{R}_i)$ for a given configuration, the force on atom $i$ is given by $\mathbf{F}_i = -\partial E/\partial \mathbf{R}_i$. So far this statement makes no explicit reference to quantum mechanics, however, through the correspondence principal and Ehrenfest's theorem, the energy is $\langle \hat{H} \rangle$ which leads us to the equation,

$$\mathbf{F}_i = -\frac{\partial}{\partial \mathbf{R}_i}\langle \hat{H} \rangle \tag{4.4}$$

$$= -\frac{\partial}{\partial \mathbf{R}_i}\left(\langle \Psi | \hat{H} | \Psi \rangle\right) - \frac{\partial E^{ion-ion}}{\partial \mathbf{R}_i} \tag{4.5}$$

$$= \underbrace{-\left\langle \Psi \middle| \frac{\partial \hat{H}}{\partial \mathbf{R}_i} \middle| \Psi \right\rangle}_{\text{Hellmann–Feynman}} \underbrace{-\left\langle \frac{\partial \Psi}{\partial \mathbf{R}_i} \middle| \hat{H} \middle| \Psi \right\rangle - \left\langle \Psi \middle| \hat{H} \middle| \frac{\partial \Psi}{\partial \mathbf{R}_i} \right\rangle}_{\text{Pulay}} - \frac{\partial E^{ion-ion}}{\partial \mathbf{R}_i} \tag{4.6}$$

where we have assumed the normalisation of $\Psi$, the many-body wavefunction. Going from eq. (4.4) to eq. (4.5) we have made use of the Born – Oppenheimer approximation, see section 2.2. The final force term quantifies charged nuclei inter-

acting with each other through Coulomb potentials. At the electronic exact ground-state, terms with gradients of the wavefunction $\Psi$ with respect to nuclear position $\mathbf{R}_i$ vanish, since the exact ground state energy is extremal with respect to all variations of the many-body wavefunction.

It is exactly the variation above that leads to the "Hellmann – Feynman" theorem [49, 125]. In DFT, the many-body wavefunction is formed from the Kohn – Sham eigenstates. These, in turn, are represented in a basis set, the choice of which can affect the computational scaling behaviour and the detailed form of the forces. CONQUEST approximates the Kohn – Sham eigenstates, $\psi^n$, in a basis of pseudo-atomic orbitals $\phi_{i\alpha}$, see section 2.8.1, a direct consequence of which results in gradients of these eigenstates to change due to the displacement of atoms. Therefore, we require the explicit evaluation of Pulay-type forces, in contrast to a plane-wave basis, which do not change with the atomic positions.

To further develop the connection between forces and stresses in CONQUEST it is useful to examine solutions of the Schrödinger equation in terms of the Hamiltonian and overlap matrix elements. For the rest of this chapter we shall define a condensed notation for the indices for $\phi_{i\alpha}$ such that $a,b,c \equiv (i,\alpha)$, where $i$ denotes the atomic index and $\alpha$ the index of the PAOs or support functions.

$$\hat{H}|\psi^n\rangle = E^n|\psi^n\rangle \tag{4.7}$$

$$|\psi^n\rangle = \sum_b c_b^n|\phi_b\rangle \tag{4.8}$$

$$\hat{H}\sum_b c_b^n|\phi_b\rangle = E^n\sum_b c_b^n|\phi_b\rangle \tag{4.9}$$

$$\sum_b c_b^n\langle\phi_a|\hat{H}|\phi_b\rangle = E^n\sum_b\langle\phi_a|\phi_b\rangle \tag{4.10}$$

$$\implies \sum_b H_{ab}c_b^n = E^n\sum_b S_{ab}c_b^n \tag{4.11}$$

We perform DFT in a non-orthogonal basis set but the orthogonality of eigenstates is still requisite through the condition $\langle\psi^m|\psi^n\rangle = \delta^{mn}$. By considering only the first-order perturbation of the Hamiltonian, which in turn perturbs the Kohn –

Sham eigenstates $\psi^n$ and the energy $E^n$. The perturbation of $\psi^n$ will also result in a perturbation of the overlap matrix $\mathbf{S}$. This is described as,

$$\sum_b (H_{ab} + \delta H_{ab}) c_b^n = (E^n + \delta E^n) \sum_b (S_{ab} + \delta S_{ab}) c_b^n \tag{4.12}$$

$$\sum_b H_{ab} c_b^n + \delta H_{ab} c_b^n = E^n \sum_b S_{ab} c_b^n + E^n \sum_b \delta S_{ab} c_b^n + \delta E^n \sum_b S_{ab} c_b^n + O(\delta^2) \tag{4.13}$$

where $n$ indexes the Kohn - Sham eigenstate. From eq. (4.11), grouping all the terms on one side we easily see that $(\mathbf{H} - E\mathbf{S})\mathbf{c} = 0$. Contracting eq. (4.13) with a generalised vector $c_a^{m*}$, such that no assumption is made about orthogonality nor site, yields the expression:

$$\sum_{ab} c_a^{m*} (\delta H_{ab} - E^n \delta S_{ab}) c_b^n = \delta E^n \sum_{ab} c_a^{m*} S_{ab} c_b^n \tag{4.14}$$

$$= \delta E^n \delta_{mn} \tag{4.15}$$

$$\sum_{ab} c_a^{n*} (\delta H_{ab} - E^n \delta S_{ab}) c_b^n = \delta E^n \tag{4.16}$$

A fuller explanation of what is happening internally in CONQUEST can be achieved by expressing eq. (4.16) in terms of the density matrix $K_{ab}$ and energy density matrix $E_{ab}$,

$$\sum_n \delta E^n = \sum_{ab} (K_{ba} \delta H_{ab} - E_{ba} \delta S_{ab})$$

$$\delta E = \sum_{ab} (K_{ba} \delta H_{ab} - E_{ba} \delta S_{ab}) \tag{4.17}$$

$$K_{ab} = \sum_n f^n c_a c_b^* \tag{4.18}$$

$$E_{ab} = \sum_n f^n c_a \varepsilon^n c_b^* \tag{4.19}$$

where $f^n$ is the band occupation number. CONQUEST can solve for the density

matrix either by diagonalisation, as in eqs. (4.18) and (4.19), or $O(N)$ which is achieved through limiting the range of the density matrix and solving with LNV (see section 2.7.2). Within CONQUEST's code, the stresses and forces are calculated independent of the density matrix solution method and the only difference is the representation of the energy density matrix (**E**) and density matrix (**K**) [114],

$$\mathbf{K} = 3\mathbf{LSL} - 2\mathbf{LSLSL}$$
$$\mathbf{E} = -3\mathbf{LHL} + 2\mathbf{LHLSL} + 2\mathbf{LSLHL}$$

where the auxiliary density matrix **L** is defined in section 2.7.2.

Finally, we arrive at the general expression for forces in CONQUEST,

$$\begin{aligned}
\mathbf{F}_i &= \lim_{\delta R_i \to 0} \frac{\delta E}{\delta R_i} = \nabla_i E \qquad (4.20)\\
&= \sum_{ab} K_{ab} \underbrace{\langle \phi_a | \nabla_i \hat{H}^{KS} | \phi_b \rangle}_{\text{Hellmann – Feynman}} \\
&+ \underbrace{\sum_{ab} K_{ab} \left[ \delta_{ia} \langle \nabla_i \phi_a | \hat{H}^{KS} | \phi_b \rangle + \delta_{ib} \langle \phi_a | \hat{H}^{KS} | \nabla_i \phi_b \rangle \right]}_{\phi \text{ - Pulay}} \\
&+ \underbrace{\sum_{ab} E_{ab} \left[ \delta_{ia} \langle \nabla_i \phi_a | \phi_b \rangle + \delta_{ib} \langle \phi_a | \nabla_i \phi_b \rangle \right]}_{\text{S - Pulay}} \qquad (4.21)
\end{aligned}$$

So far we have only considered the electronic states, and the expression above is equivalent to eq. (4.6) without the nuclear electrostatic term which is easily included. From this template we have encoded all contributions to the forces, where the above expression includes terms involving the Hamiltonian matrix, the overlap matrix and variations thereof. To proceed, it is useful to remind ourselves of the Hamiltonian components,

$$\hat{H} = \hat{T} + \hat{V}^L + \hat{V}^{NL} + \hat{V}^{Ha} + \hat{V}^{XC} \qquad (4.22)$$

where $\hat{T}$ is the electronic kinetic energy, $\hat{V}^L$ the local part of the pseudopotential, $\hat{V}^{NL}$ the non-local pseudopotential, $\hat{V}^{Ha}$ the Hartree potential and $V^{XC}$ the exchange-correlation potential. In the following sections we shall define how each term of eq. (4.21) contributes to the total forces and stresses under the assumption of a self-consistent charge density. We will cover the differences when working with a non-self-consistent charge density in section 4.6.

### 4.2.1 Pulay terms

One draw back of utilising localised basis sets is that they move with the atoms, so taking derivatives of wavefunctions with respect to position has an error associated in doing so. Equation (4.21) shows the general forces in the context of a many-body wavefunction where we have defined the Pulay [126] terms of the forces involving gradients of the Kohn – Sham eigenstates represented in a basis of PAOs. We showed at the end of section 4.2 these Pulay terms in eq. (4.6) are equivalent to the Pulay terms in eq. (4.21).

#### 4.2.1.1 Basis Pulay

The $\phi$-Pulay parts of eq. (4.21) demonstrates how we require gradients of the basis functions to calculate this specific Pulay correction to the total force. This action is realised through gradients of the Hamiltonian matrix elements $H_{ab}$, which are themselves contractions of the individual grid-based Kohn – Sham potential terms $\hat{V}^{(L)}+\hat{V}^{Ha}+\hat{V}^{XC}$ with the basis functions.

Thus the $\phi$-Pulay forces and stresses are,

$$\begin{aligned} F^{\phi P}_{i\lambda} &= -2\sum_{ab} K_{ab}\big(\langle \nabla_{i\lambda}\phi_a|\hat{V}^{(L)}+\hat{V}^{Ha}+\hat{V}^{XC}|\phi_b\rangle \\ &\quad + \langle \phi_a|\hat{V}^{(L)}+\hat{V}^{Ha}+\hat{V}^{XC}|\nabla_{i\lambda}\phi_b\rangle\big) \qquad (4.23) \\ \sigma^{\phi P}_{\lambda\mu} &= -2\sum_{i}\sum_{ab} K_{ab}\big(\langle (\nabla_{i\lambda}\phi_a)R_{i\mu}|\hat{V}^{(L)}+\hat{V}^{Ha}+\hat{V}^{XC}|\phi_b\rangle \\ &\quad + \langle \phi_a|\hat{V}^{(L)}+\hat{V}^{Ha}+\hat{V}^{XC}|(\nabla_{i\lambda}\phi_b)R_{i\mu}\rangle\big) \qquad (4.24) \end{aligned}$$

where $\lambda,\mu$ are the Cartesian directions.

#### 4.2.1.2 Overlap pulay

Forces involving the overlap matrix (S-Pulay) forces eq. (4.21) require usage of the energy density matrix $E_{ab}$, defined in eq. (4.19). As such, all energy contributions from the Kohn – Sham Hamiltonian eq. (4.22) are included implicitly. Integrals for the overlap matrix are found in Fourier space as proposed by Sankey [82] and exact implementation details for CONQUEST can be found in Torralba *et al* [81]. The form of the S-Pulay force is,

$$F_{i\lambda}^{SP} = -2\sum_{ab} E_{ab}\big(\langle \nabla_{i\lambda}\phi_a|\phi_b\rangle + \langle \phi_a|\nabla_{i\lambda}\phi_b\rangle\big) \tag{4.25}$$

and the stress,

$$\sigma_{\lambda\mu}^{SP} = -2\sum_{i}\sum_{ab} E_{ab}\big(\langle(\nabla_{i\lambda}\phi_a)|\phi_b\rangle + \langle\phi_a|(\nabla_{i\lambda}\phi_b)\rangle\big)R_{i\mu} \tag{4.26}$$

#### 4.2.1.3 Kinetic

The radial components of basis functions, for the calculation of the electronic kinetic energy, are integrated by performing a one-dimensional Fourier transforms. This is similar to the method we use to find the overlap matrix, where the integral in eq. (4.27) is remarkably similar to that of the overlap. As we see in the equations for force and stress, this term involves the density matrix $K_{ab}$, distinguishing it as $\phi$-Pulay contribution. The force due to the kinetic energy of electrons enters DFT *only* in the case when the basis set depends upon the atomic positions, i.e. it is purely a Pulay correction. The kinetic energy in a basis of PAOs is given by,

$$E^{kin} = \frac{1}{2}\sum_{ab} K_{ab}\int d\mathbf{r}\ \nabla\phi_a(\mathbf{r})\cdot\nabla\phi_b(\mathbf{r}) \tag{4.27}$$

$$= \frac{1}{2}\sum_{ab} K_{ab}T_{ab} \tag{4.28}$$

And so the force and stress follow,

$$F_{i\lambda}^{kin} = -\frac{1}{2}\sum_{ab} K_{ab}\frac{\partial T_{ab}}{\partial R_{i\lambda}} \tag{4.29}$$

$$\sigma_{\lambda\mu}^{kin} = \frac{1}{2}\sum_{i}\sum_{ab} K_{ab}\frac{\partial T_{ab}}{\partial R_{i\lambda}} R_{i\mu} \tag{4.30}$$

### 4.2.2 Pseudopotential terms

Within the context of self-consistent DFT, the Hellmann – Feynman part of eq. (4.21) contains *only* contributions from the local and non-local parts of the pseudopotential, exactly equivalent to the Hellmann – Feynman theorem. Forces due to variations of the local potential (here $V^{ps,local}(\mathbf{r}) \equiv V^{(L)}(\mathbf{r})$) are,

$$E^{(L)} = \int d\mathbf{r}\, V^{(L)}(\mathbf{r}) n(\mathbf{r}) \tag{4.31}$$

$$F_{i,\lambda}^{(L)} = \frac{\partial E^{(L)}}{\partial R_{i,\lambda}} \tag{4.32}$$

$$= \int d\mathbf{r}\, n(\mathbf{r}) \frac{\partial V^{(L)}(\mathbf{r})}{\partial R_{i,\lambda}} \tag{4.33}$$

$$\sigma_{\lambda\mu} = \sum_{i} \int d\mathbf{r}\, n(\mathbf{r}) \frac{\partial V^{(L)}(\mathbf{r})}{\partial R_{i,\lambda}} R_{i,\mu} \tag{4.34}$$

where $i$ denotes the atomic index, $\lambda$ and $\mu$ the Cartesian direction index. The form of $V^{(L)}$ will vary depending on the pseudopotential implementation used. CONQUEST can use SIESTA's [83, 127, 128] form of the Troullier – Martins [129] pseudopotentials, or Hamann's ONCV [130] pseudopotentials. In each situation, the form of the local potential will differ, summarised by whether $V^{(L)}$ is calculated or tabulated. The SIESTA form of Troullier – Martins local potential optimises the "local" potential for smoothness producing a "local" density consequently reducing the number of integration grid points required for $V^{(L)}$. This results in eq. (4.33) becoming eq. (4.35), whereas the Hamann-type provides us with a tabulated form and we calculate $F_{i,\lambda}^{(L)}$ as in eq. (4.36).

$$F_{i,\lambda}^{TM,(L)} = \int d\mathbf{r}\ \frac{\partial n_i^{(L)}(\mathbf{r})}{\partial R_{i,\lambda}} V^{Ha}(\mathbf{r}) \tag{4.35}$$

$$F_{i,\lambda}^{Ham,(L)} = \int d\mathbf{r}\ n(\mathbf{r}) \frac{\partial V^{(L)}(\mathbf{r})}{\partial R_{i,\lambda}} \tag{4.36}$$

As mentioned at the end of section 4.1.1, the energy due to the local part of the pseudopotential is found on the grid. This results in the need to include a contribution due to the deformation of the cell, changing the volume associated with each integration grid point. This contribution to the total stress is given by the Jacobian of the transform eq. (4.2), henceforth termed the Jacobian stress. The contribution to the Jacobian stress given by the local potential is,

$$\sigma_{\lambda\mu}^{Jac,L} = \delta_{\lambda\mu} E^L \tag{4.37}$$

where $E^L$ is the energy from the local part of the pseudopotential and is a strictly diagonal contribution.

For the non-local (NL) part of the pseudopotential the energy and forces are given by,

$$E^{(NL)} = \sum_{ab,i\zeta} K_{ab} \langle \phi_a | \chi_{i,\zeta} \rangle A_{i,\zeta} \langle \chi_{i,\zeta} | \phi_b \rangle \tag{4.38}$$

$$\begin{aligned} F_{i,\lambda}^{(NL)} &= \frac{\partial E^{NL}}{\partial R_{i,\lambda}} \\ &= \sum_{ab,\zeta} \underbrace{K_{ab} \langle \nabla_{i,\lambda} \phi_a | \chi_{i,\zeta} \rangle A_{i,\zeta} \langle \chi_{i,\zeta} | \phi_b \rangle}_{\phi\text{-Pulay}} + \underbrace{K_{ab} \langle \phi_a | \nabla_{i,\lambda} \chi_{i,\zeta} \rangle A_{i,\zeta} \langle \chi_{i,\zeta} | \phi_b \rangle}_{\text{Hellmann–Feynman}} \end{aligned} \tag{4.39}$$

$$\begin{aligned} \sigma_{\lambda\mu}^{(NL)} &= \sum_{ab,i\zeta} K_{ab} \langle (\nabla_{i,\lambda} \phi_a) R_{i,\mu} | \chi_{i,\zeta} \rangle A_{i,\zeta} \langle \chi_{i,\zeta} | \phi_b \rangle \\ &\quad + K_{ab} \langle \phi_a | (\nabla_{i,\lambda} \chi_{i,\zeta}) R_{i,\mu} \rangle A_{i,\zeta} \langle \chi_{i,\zeta} | \phi_b \rangle \end{aligned} \tag{4.40}$$

where $a, b$ are indices inclusive of atomic and support function indices; $K_{ab}$ the density matrix; $\phi$ the PAOs; $\chi$ the non-local projector functions; $A$ the matrix

containing the scattering constants for the projector functions; and $\lambda$ the Cartesian direction. The index $\zeta$ denotes the $l,m$ quantum numbers necessary for the evaluation of the $l$-dependent $V^{(NL)}$. For completeness, SIESTA form the non-local potential using Kleinman - Bylander projector functions [66] (one projector per $l$), whilst Hamann uses Vanderbilt non-local projectors [68, 130] (multiple projectors per $l$). Mathematically, the non-local Hellmann–Feynman and Pulay terms can be calculated separately, however, within CONQUEST they are calculated together since we use atom-centred orbitals the quantity $\partial\langle\phi_i|\chi_k\rangle/\partial R_i = -\partial\langle\phi_i|\chi_k\rangle/\partial R_k$. So, we may calculate the $\phi$-Pulay NL contribution, $\partial\langle\phi_i|\chi_k\rangle/\partial R_i$), once and re-use for the calculation of Hellmann–Feynman NL contribution.

## 4.3 Ion-Ion interactions

Ion-ion terms are found through the use of Ewald sums, splitting the total interaction of all ions such that there is a long-ranged (reciprocal space) component and short-ranged (real space) component. Calculation of the energy and forces in CONQUEST are by the standard methods of Gaussian smeared charges and can be found in App. F of R. Martin's book *Electronic structure* [46] and references therein.

There are three distinct contributions to the ion interaction stress: real space; reciprocal space; and the self-interaction of the Gaussian like charges. The Gaussian self-stress is the diagonal quantity,

$$\sigma^{GSS}_{\lambda\mu} = \frac{\pi}{2\Omega\gamma^2}\left[\sum_i Z_i\right]^2 \delta_{\lambda\mu} \tag{4.41}$$

where $\gamma$ is a term used to balance the real and reciprocal space Ewald terms, $\Omega$ is the simulation cell volume and $Z_i$ is the charge on a nucleon. The reciprocal-space contribution is,

$$\sigma_{\lambda\mu} = \frac{\pi}{2\Omega\gamma^2}\sum_{G\neq 0}\frac{e^{-G^2/4\gamma^2}}{G^2/4\gamma^2}\left|\sum_I Z_I e^{i\mathbf{G}\cdot\mathbf{r}_I}\right|^2\left[\frac{G_\lambda G_\mu}{2\gamma}+\frac{2G_\lambda G_\mu}{G^2}-\delta_{\lambda\mu}\right] \tag{4.42}$$

The Ewald real space contribution to the stress is given by:

$$\sigma_{\lambda\mu} = -\sum_{ij} Z_i Z_j \frac{\left(\frac{erfc(\gamma^{1/2}|\mathbf{r}|)}{|\mathbf{r}|} + 2(\gamma\pi)^{1/2} e^{-\gamma|\mathbf{r}|^2}\right)}{|\mathbf{r}|^2} \mathbf{r}_{i\lambda}\mathbf{r}_{j\mu} \tag{4.43}$$

## 4.4 Hartree

The Hartree energy is the classical Coulomb interaction of all electrons in the system interacting with each other. Within the context of DFT, it is the integral of the electron density at some point $n(\mathbf{r})$ interacting with the electron density $n(\mathbf{r}')$ at another point. In Hartree atomic units this is given by,

$$E^{Ha} = \frac{1}{2}\int d\mathbf{r}\, d\mathbf{r}' \frac{n(\mathbf{r})n(\mathbf{r}')}{|\mathbf{r}-\mathbf{r}'|} \tag{4.44}$$

where $\mathbf{r}'$ indicates any other position away from $\mathbf{r}$. The Hartree potential is calculated in Fourier space using a fast-Fourier transform of the density and then Fourier transform back resulting in the form,

$$V^{Ha}(\mathbf{r}) = FT\left[\widetilde{V}^{Ha}(\mathbf{G})\right] \tag{4.45}$$

$$\widetilde{V}^{Ha} = \frac{\widetilde{n}(\mathbf{G})}{G^2} \tag{4.46}$$

At the end of section 4.1.1 we talked about corrections to the electrostatic integrals, involving $1/|\mathbf{r}-\mathbf{r}'|$, when the cell is deformed. Since we calculate the Hartree potential in Fourier-space, these changes to the length in $1/|\mathbf{r}-\mathbf{r}'|$ are now changes to the length of the **G**-vectors required to evaluated the Hartree potential. To account for this deformation to the cell we find an equation analogous to eq. (4.2) describing the deformation of the **G**-vectors,

$$G'_\lambda = \sum_\mu G_\mu(\delta_{\mu\lambda} - \epsilon_{\mu\lambda}) \tag{4.47}$$

$$\implies \frac{\partial}{\partial\, \epsilon_{\lambda\mu}} \frac{1}{G^2} = \frac{2G_\lambda G_\mu}{G^4} \tag{4.48}$$

again where $\lambda$ and $\mu$ are the Cartesian directions, and $\epsilon$ the strain. This term is analogous to the term in Ewald sum where the change in the cell volume necessitates the extra term above and is calculated,

$$\sigma_{\lambda\mu}^{Ha} = \int d\mathbf{r}\, n(\mathbf{r})\, FT\left[\frac{2G_aG_b}{G^4}\,\tilde{n}(\mathbf{G})\right] \tag{4.49}$$

Equation (4.44) is integrated on the grid and thus will also have a Jacobian contribution to the total stress from the changes in grid point volume which is,

$$\sigma_{\lambda\mu}^{Jac,Ha} = \delta_{\lambda\mu}E^{Ha} \tag{4.50}$$

## 4.5 Exchange-correlation

Exchange - correlation energy is found on the grid, and so there must be a term contributing to the stress as the grid point volume changes. For all exchange-correlation functionals this contribution is the Jacobian of the exchange-correlation energy,

$$\sigma_{\lambda\mu}^{Jac,XC} = \delta_{\lambda\mu}E^{XC} \tag{4.51}$$

For the LDA, the equation above completely defines the exchange-correlation forces and stresses, however, functionals involving gradients of the density require some care.

### 4.5.1 Generalised gradient approximation

A thorough derivation of this stress contribution in the context of pseudo-atomic orbitals and arbitrary integration grid can be found in the work of Balbás, Martins and Soler [131]. The generalised gradient approximation requires gradients of the density to be found as part of the correction to the total energy. Since we must take a gradient of the density, if the density were deformed then the gradients, upon which the corrections are found, must also change.

$$\sigma_{\lambda\mu}^{XC,GGA} = -\int d\mathbf{r}\frac{\partial f(n(\mathbf{r}),\nabla n(\mathbf{r}))}{\partial(\nabla_\lambda n(\mathbf{r}))}\nabla_\mu n(\mathbf{r}) \tag{4.52}$$

where $\lambda$ and $\mu$ denote the Cartesian directions, and $f(n(\mathbf{r})\nabla n(\mathbf{r}))$ is the local exchange-correlation energy density.

## 4.6 Non-self-consistent

This contribution is a special case, as noted in the introduction. One can think of non-self-consistent forces as a correction to the forces when the charge density is not converged and comes about from Harris-Foulkes theorem [132, 133]. As such, this force contribution is only valid when the initial charge density is formulated in terms of the atomic charge densities or in the limit of a few self-consistent steps [134]. At this point it is useful to provide the reader with a schematic highlighting the differences between the self-consistent and NSC forces,

$$F_i = F^L + F^{NL} + F^{SP} + F^{\phi P} + F^{Ha} + F^{XC} \quad \text{(SC)} \quad (4.53)$$

$$F_i = F^L + F^{NL} + F^{SP} + F^{\phi P} + \underbrace{F^{Ha} + F^{XC} + F^{\Delta Ha} + F^{\Delta XC}}_{F^{NSC}} \quad \text{(NSC)} \quad (4.54)$$

Since CONQUEST uses PAOs, a reasonable initial charge density is constructed from the superposition of the atomic charge densities. This is done for all calculations where a different initial charge density is not present (and loaded), and in the context of NSC calculations the form of this force contribution is,

$$n^{PAD}(\mathbf{r}) = \sum_i \eta_i(|\mathbf{r} - \mathbf{R}_i|) \quad (4.55)$$

$$\begin{aligned} \mathbf{F}_i^{NSC} &= -\int d\mathbf{r} \left[\Delta V^{Ha}(\mathbf{r}) + \Delta n(\mathbf{r}) \mu'_{XC}[n^{PAD}(\mathbf{r})]\right] \nabla_i \eta_i(|\mathbf{r} - \mathbf{R}_i|) \\ &= -\int d\mathbf{r} \left(V^{Ha,out}(\mathbf{r}) - V^{Ha,PAD}(\mathbf{r})\right) \nabla_i \eta_i(|\mathbf{r} - \mathbf{R}_i|) \\ &\quad -\int d\mathbf{r} \left(n^{out}(\mathbf{r}) - n^{PAD}(\mathbf{r})\right) \mu'_{XC}[n^{PAD}(\mathbf{r})] \nabla_i \eta_i(|\mathbf{r} - \mathbf{R}_i|) \end{aligned} \quad (4.56)$$

$$\sigma_{\lambda\mu}^{NSC} = -\int d\mathbf{r} \left[\Delta V^{Ha}(\mathbf{r}) + \Delta n(\mathbf{r}) \mu'_{XC}[n^{PAD}(\mathbf{r})]\right] \frac{\partial \eta_i(|\mathbf{r} - \mathbf{R}_i|)}{\partial R_{i,\lambda}} R_{i,\mu} \quad (4.57)$$

where $n^{PAD}$ is the inital charge density defined by the sum of the atomic

charge densities $\eta_i$. $\Delta n(\mathbf{r}) = n^{out}(\mathbf{r}) - n^{PAD}(\mathbf{r})$ is the difference between the input and output densities, where the output density is built from the KS orbitals, i.e. $n^{out}(\mathbf{r}) = 2\sum_n f^n |\psi^n(\mathbf{r})|^2$. $\Delta V^{Ha}$ is the Hartree potential associated with $\delta n(\mathbf{r})$. $\mu'_{XC}$ is essentially the derivative with respect to the density of $V^{XC}$, i.e. $V^{XC}(\mathbf{r}) \equiv \mu(n^{PAD}(\mathbf{r}))$ and $\mu'_{XC} = d\mu_{XC}(n)/dn$. Non-self-consistent forces for the GGA functional have been implemented in CONQUEST where glycine and alanine were 'pre-relaxed' using only NSC forces before progressing the relaxation with fully self-consistent forces [115].

We now have the form of the NSC force and stress, however, the change to the *total* stress is more complex. Inspecting eqs. (4.56) and (4.57) we see there are terms with the Hartree potential and terms with the exchange-correlation potential. The Hartree potential is calculated in Fourier-space (see eqs. (4.45) and (4.46)) and as the cell changes there are changes to the length of the **G**-vectors analogous to that of eq. (4.49),

$$\widetilde{V}^{Ha,PAD} = \frac{2G_aG_b}{G^4}\widetilde{n}^{PAD}(\mathbf{G}) \tag{4.58}$$

$$\widetilde{V}^{Ha,out} = \frac{2G_aG_b}{G^4}\widetilde{n}^{out}(\mathbf{G}) \tag{4.59}$$

where $\widetilde{n}^{PAD}(\mathbf{G})$ and $\widetilde{n}^{out}(\mathbf{G})$ are the Fourier transformed pseudo-atomic and output electron densities respectively, defining the Fourier-space Hartree potentials to be Fourier-transformed back to real-space ready for evaluation. The maximum **G**-vector is given by the integration grid spacing and the minimum by the simulation cell size. This difference in the calculation of the Hartree potential is accumulated in the Hartree stress, as in section 4.4.

The Hartree and exchange-correlation energy are found on the integration grid, as mentioned in sections 4.4 and 4.5. Therefore, there must be a contribution due to a change in the volume of the integration grid points under deformation. Equations (4.50) and (4.51) will now include an extra contribution,

$$\sigma_{\lambda\mu}^{Jac,Ha} = \delta_{\lambda\mu}(E^{Ha} + \Delta E^{Ha}) \tag{4.60}$$

$$\sigma_{\lambda\mu}^{Jac,XC} = \delta_{\lambda\mu}(E^{XC} + \Delta E^{XC}) \tag{4.61}$$

where $\Delta E^{Ha}$ and $\Delta E^{XC}$ are the corrections to the double-counting of the Hartree and exchange-correlation energies respectively.

## 4.7 Neutral atom

The neutral atom (NA) formalism [82, 83] is used to reduce the effort required to compute the electrostatics and requires a simple reformulation for some parts of the forces and stresses. The NA formalism replaces the need for an Ewald sum to compute the long range ion-ion interactions, a method adopted by many local orbital approaches for DFT. This is achieved through the screening of ionic cores with an atomic density and defining a modified density as in,

$$\delta n(\mathbf{r}) = n(\mathbf{r}) - n^{PAD}(\mathbf{r}) \equiv n(\mathbf{r}) - \sum_i n_i^{PAD}(\mathbf{r}) \tag{4.62}$$

where $\delta n(\mathbf{r})$ is the modified density, $n(\mathbf{r})$ the total density and $n^{PAD}(\mathbf{r})$ the total pseudo-atomic density found as the superposition of the per atom pseudo-atomic densities. For calculations outside of the neutral atom formalism the constituent components of the total energy are,

$$E^{tot} = E^{kin} + E^{NL} + E^{XC} + E^{L} + E^{Ha} + E^{cc} \tag{4.63}$$

where $E^{kin}$ the kinetic energy of electrons, $E^{NL}$ the non-local pseudopotential energy, $E^{XC}$ the exchange-correlation energy, $E^{L}$ the local pseudopotential energy, $E^{Ha}$ the Hartree energy and $E^{cc}$ the Ewald energy. The neutral atom formalism reformulates the last three terms such that,

$$E^{L} + E^{Ha} + E^{cc} = E^{NA} + E^{scc} + E^{\delta Ha} \tag{4.64}$$

where $E^{NA}$ is the neutral atom energy, $E^{scc}$ the screened ion-ion interaction energy and $E^{\delta Ha}$ the energy due to the modified Hartree potential, defined by $\delta n(\mathbf{r})$ (see eq. (4.62)). The form of each individual term on the right-hand side of eq. (4.64) are:

$$E^{NA} = \int d\mathbf{r}\, n(\mathbf{r}) \sum_i V_i^{NA}(\mathbf{r}) \tag{4.65}$$

$$E^{scc} = \frac{1}{2} \sum_{ij} \left[ \frac{Z_i Z_j}{|\mathbf{R}_i - \mathbf{R}_j|} - \int d\mathbf{r}\, n_i^{PAD}(\mathbf{r}) V_j^{Ha,PAD}(\mathbf{r}) \right] \tag{4.66}$$

$$E^{\delta Ha} = \frac{1}{2} \int d\mathbf{r}\, \delta n(\mathbf{r}) \delta V^{Ha}(\mathbf{r}) \tag{4.67}$$

where $V_i^{NA} = V_i^L + V_i^{Ha,PAD}$. Since $V_i^{NA}$ encompasses the local and atomic Hartree potential, the stress from the NA potential is accumulated in both the Jacobian and local Hellmann–Feynman term,

$$\sigma_{\lambda\mu}^{NA} = \int n(\mathbf{r}) \sum_i \frac{\partial V_i^{NA}}{\partial R_{i,\lambda}} R_{i,\mu} \tag{4.68}$$

$$\sigma_{\lambda\mu}^{Jac,NA} = \delta_{ab} E^{NA} \tag{4.69}$$

The screened ion-ion forces and stress,

$$F_{i,\lambda}^{scc} = \frac{1}{2} \sum_j \left[ \frac{Z_i Z_j}{|\mathbf{R}_i - \mathbf{R}_j|^3} (R_{i,\lambda} - R_{j,\lambda}) - \int d\mathbf{r}\, \frac{\partial n_i^{PAD}(\mathbf{r})}{\partial R_{i,\lambda}} V_j^{Ha,PAD}(\mathbf{r}) \right] \tag{4.70}$$

$$\sigma_{\lambda\mu}^{scc} = \sum_i \frac{1}{2} \sum_j \left[ \frac{Z_i Z_j}{|\mathbf{R}_i - \mathbf{R}_j|^3} (R_{i,\lambda} - R_{j,\lambda}) - \int d\mathbf{r}\, \frac{\partial n_i^{PAD}(\mathbf{r})}{\partial R_{i,\lambda}} V_j^{Ha,PAD}(\mathbf{r}) \right] (R_{i,\mu} - R_{j,\mu}) \tag{4.71}$$

where the maximum $\mathbf{G}$-vectors for the screening Hartree term are defined by the radial integration grid spacing for the Fourier transform and the minimum is given by the cutoff radius for the atomic species.

The delta Hartree stress

$$\sigma_{\lambda\mu}^{\delta Ha} = \delta_{\lambda\mu} E^{\delta Ha} \tag{4.72}$$

It has been shown that whilst the neutral atom may reduce the computational complexity and grid spacing as compared to calculations without NA, $V^{NA}$ can remain quite deep resulting in a less dramatic reduction in the number of integration grid points [135]. This may be negated through use of NA projectors, which have been implemented in CONQUEST, however, this is beyond the scope of this thesis and has been included for completeness.

## 4.8 Testing our implementation

To test the implementation we compare the analytic stress, as implemented in the sections prior to this, with a numerically derived stress. For the numerical stress we have used finite differences of the total energy of deformed structures. We have chosen the deformations such that we have two deformation lengths ($\Delta l$) such that they straddle a point of reference ($l$) used for the analytic calculation, i.e. if $l$ is a reference point then the two points used for the finite differences will be $l_1 = l - \Delta l$ and $l_2 = l + \Delta l$. Judicious choice of $\Delta l$ is essential, since a value too large will not accurately reflect the choice of using a two-point derivative and too small will introduce numerical rounding errors. We have chosen a deformation length of $1 \times 10^{-2}$ $a_0$, close to the criterion in the work of Golesorkhtabar *et al* [136] of $\Delta h < 10^{-2}$Å.

For our testing purposes we have chosen to use a variety of crystal systems with varying basis set size and and functionals. Furthermore we shall also test the stress calculation implementation of the different modes of operation: self-consistent; neutral atom; and non-self-consistent stress calculations. We vary the lattice parameters isotropically scaling the lattice parameters from their optimal values such that the formula for our finite difference is,

$$\sigma_{\lambda\lambda}^{num.} = \frac{(E_{tot}(V_2) - E_{tot}(V_1))(V_2 + V_1)}{2(V_2 - V_1)} \tag{4.73}$$

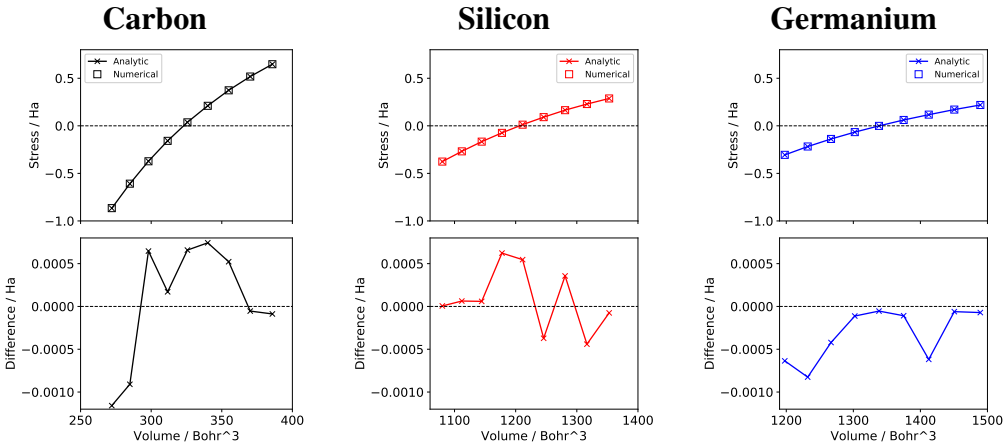


**Figure 4.1:** Comparison of analytic stress with stress from finite differences. The upper plots show a line for analytical stress ($\sigma^{ana.}$) and boxes represent stress from finite differences ($\sigma^{num.}$), see eq. (4.73). The lower plots show the difference, $\sigma^{ana.} - \sigma^{num.}$, since the difference is too small to distinguish between them in the upper plots.

where $V_1 = (l - \Delta l)^3$ and $V_2 = (l + \Delta l)^3$ for cubic systems; and $\lambda$ refers to Cartesian direction. We do not test the off-diagonal stresses since at present CONQUEST is limited to orthorhombic simulation cells only.

For our first tests we have used bulk C, Si and Ge, in a diamond crystal structure, with a single-$\zeta$ basis set, since the level of basis set completeness is not important when comparing with calculations of equal basis. Self-consistent calculations were done with a $9 \times 9 \times 9$ $\Gamma$-centred Monkhorst-Pack k-point mesh and an integration grid cutoff of 400 Ha were optimal. The choice of such fine integration grid spacing and k-point mesh, however, are crucial to the accuracy since the numerical stresses are sensitive to these inputs.

Figure 4.1 shows a near perfect agreement between stresses calculated by methods outlined above and finite differences in eq. (4.73). These results are of the same order of magnitude as results from a recent FHI-AIMS publication [137].

## 4.9 Conclusions and discussion

In this chapter we highlighted the importance of stress to specify the physical state of matter in materials simulation. We have reviewed how this has been derived, from

the initial work within a plane-wave basis, then in a basis of atomic orbitals, how these introduce Pulay terms and shown how the forces and stresses are computed. CONQUEST is able to produce calculations using a non-self-consistent algorithm, via the Harris energy functional, or in a self-consistent manner and we have shown how the formulae for the forces and stress differ within these two methods. The neutral atom formalism has previously been implemented, allowing CONQUEST to operate with a reduced number of integration grid points and less than linear scaling Ewald method for the electrostatics. We have discussed the changes to energy contributions and shown forces and stresses due to this change of formalism.

Our testing has shown that analytic and finite difference stresses agree extremely well with each other thus proving our implementation is accurate. Beside the importance of physical state specification, this work has since allowed for the implementation of the more sophisticated NPT ensemble, unlocking the potential for immense isobaric molecular dynamics (MD) simulation. Such calculations would be exceptionally impactful works for the study of amorphous materials, where large numbers of atoms are required to reduce finite-size effects and quenching of the simulation is usually under isobaric conditions [138]. Furthermore, this work has since been extended by other CONQUEST developers to calculate atomic stresses such that in the near future we may be able to perform transport calculations via the Green – Kubo relations.

So far we have not shown any testing of the $O(N)$ method, however, in the next chapter we shall be exploring the calculation for forces and stresses with some surprising results.

# Chapter 5

# Effects of density matrix localisation on: Energy, forces and pressure in $O(N)$ DFT

## 5.1 Introduction

Physical phenomena which can be modelled *atomistically* take place over a variety of length scales; from bonds between atoms at around 0.1 nm, to the size of crystal grains in the 10s of nanometers. Whilst these specific examples may be calculated using classical mechanics, this method relies on the fitting of empirical potentials. DFT relies upon quantum mechanics, a method which is *compared* to observation rather than fit to it[1]. Thus, large-scale simulation of systems with quantum mechanical accuracy are not simply desirable, but necessary to reveal details of larger features present in real-world materials.

Section 2.7 introduced the two methods by which CONQUEST solves for the density: (i) exact diagonalisation; and (ii) $O(N)$. Whilst $O(N)$ methods scale linearly with the number of atoms, a fundamental assumption is made on the locality of the density matrix or so-called "nearsightedness" [71]. Single-particle states $|\psi_n\rangle$ may span the entire system, however, the physics of the electronic states in a region

[1] The author accepts that use of hybrid functionals and Hubbard corrections (DFT+U) are counter-examples to this claim but would argue they are usually motivated by changes in the physics of the system.

of material is only affected by the *local* environment. For observables, determining *how* local this environment need be is central to the validity of practical $O(N)$ DFT calculations.

Localisation of the density matrix can be quantified as a decay rate of the density between two points $\rho(\mathbf{r},\mathbf{r}') \approx e^{-\gamma|\mathbf{r}-\mathbf{r}'|}$ , where $\gamma$ is the decay rate and the exponential decay has been proven analytically [139–142] and numerically [143]. Quantifying how $\gamma$ depends on the system under study is of paramount importance to $O(N)$ DFT and found to be: $\gamma \propto \sqrt{\Delta E_g}$ for insulators [144–146]; $\propto \Delta E_g$ for semiconductors [147]; $\propto \sqrt{T}$ for metals [146]; and $\propto T$ for metals at low-temperature [147] where $\Delta E_g$ is the band gap and $T$ the temperature. Recent work has found that exponential decay of the density matrix is not true for materials which exhibit broken time-reversal symmetry [148], however, this is beyond the scope of this thesis and included for completeness.

Previously, the error in total energy and forces against diagonalisation has been quantified for carbon [149]. Furthermore, the effects of density matrix truncation on the charge density of diamond have also been quantified [143], however, neither of these studies probed the effects of varying the band gap. In order to simplify testing of the effects of density matrix localisation on the convergence and reliability of $O(N)$ we have used simple 8-atom bulk carbon, silicon and germanium structures, all sharing the same atomic structure and varying only the assumed gap of the materials. We have chosen to quantify the convergence of: total energy; force; and pressure for minimum energy structures as compared to diagonalisation. Quantification of practical quantities, such as lattice parameter and bulk modulus were also investigated to qualitatively ascertain the error induced by **L**-matrix range truncation.

## 5.2 Methodology and computational details

A simple 8-atom diamond structure cell was used for all calculations presented in this chapter. To obtain the minimum energy structures for a given **L**-range[2],

[2]Not applicable to exact diagonalisation!

fully self-consistent static calculations of isotropically scaled structures were performed. Minimum energy structures were then obtained by Birch-Murnaghan [150, 151] equation of state fitting with the `Atomic Simulation Environment (ASE)` code [152] for energy-volume data. The data produced at this stage was used to produce figs. 5.2 and 5.3, whilst new self-consistent static calculations were performed for the new minimum energy structures (resulting in figs. 5.1(a) and 5.1(c)). Since the minimum energy structures have no forces between atoms, one atom is displaced 1% along the $\langle 100 \rangle$-direction to perturb the structure and yield forces. Only the maximum forces of the displaced atoms, along the $\langle 100 \rangle$-direction, were used to produce fig. 5.1(b).

Calculations presented in this chapter were performed using CONQUEST (`Master branch: v0.51-203`), for *both* $O(N)$ and exact diagonalisation calculations, with optimised norm-conserving Vanderbilt pseudopotentials using the ONCVPSP code v3.2.3 [130] and Perdew-Burke-Ernzerhof GGA exchange-correlation functionals [60, 61]. Single-zeta (SZ) basis sets were generated with v0.2 of the CONQUEST basis set generation suite using the default equal radii confinement method outlined in Chapter 3 and Ref. [103]. To ensure solution methods and **L**-range are isolated variables, excessive calculation parameters controlling accuracy were used. For exact diagonalisation we used an $9 \times 9 \times 9$ Monkhorst-Pack [69] $k$-point grid and Fermi-Dirac smearing factor of 0.0004 Ha to ensure no spurious fractional occupation of conduction band states. Both $O(N)$ and exact diagonalisation used a real-space integration grid cutoff of 400 Ha.

Since **L**-range is the variable being probed, values used are specified in the data of our $O(N)$ calculations. However, one should note that ranges specified in figures below are not given in units of length but rather as a multiplier factor of the lattice parameter:

$$\alpha^L = \frac{R^L}{a_0} \tag{5.1}$$

where $\alpha^L$ is the multiplier factor, $R^L$ the **L**-range and $a_0$ the lattice parameter of the system being calculated. This decision was taken to eliminate the comparison of

structures with two different lattice parameters with the same absolute $R^L$, which are actually *slightly* inequivalent calculations. Whilst SZ basis sets are not as accurate as those offering more variational degrees of freedom (Chapter 3), basis sets beyond SZP reduce the sparsity of matrices used for CONQUEST with the failure to invert the overlap (**S**-matrix) being particularly troublesome.

## 5.3 Results

Convergence of structure relaxations, when measured as differences in total energy, are generally quoted as an energy difference *per atom*. Considering an energy difference of 10 meV/atom our convergence tolerance, this roughly converts to a total energy difference of $3 \times 10^{-3}$ Ha for an 8 atom cell. Assuming a 10% error is acceptable, an absolute error of $3 \times 10^{-4}$ Ha: C requires an **L**-range of $3 \times a_0$; Si at least $3.6 \times a_0$; and Ge is off the chart (fig. 5.1(a)). However, this is a measure of *total energy* convergence which is known to be slow and measuring $O(N)$ total energy convergence to diagonalisation does not tell us how well $O(N)$ methods describe material properties. Energy differences, such as forces, converge much faster than total energy and differences between $O(N)$ and exact diagonalisation forces (see fig. 5.1(b)) illustrate this point very well. $O(N)$ forces are within 10% at the minimal **L**-range tested ($\alpha^L = 1.6a_0$) for all materials, assuring us that structural relaxation via $O(N)$ (like results in chapter 6) are reliable.

Practically, when performing cell optimisation a target pressure is specified. Results in fig. 5.1(c) are found from minimum energy structures, thus the pressure target here is 0 GPa. If we assume a pressure tolerance of 0.1 GPa, then to be within 10% of this ($1 \times 10^{-2}$ GPa) requires an **L**-range of 25 Bohr for C, more than 40 Bohr for Si and practically impossible for Ge (see fig. 5.1(c)). Thus, the error in pressure converges even more slowly than total energy with respect to **L**-range. For $O(N)$ calculations at zero temperature this poses a significant issue when performing pressure based structure searches, especially in the case of small band gap materials. However, at finite temperature the decay rate of the density matrix increases with increased temperature [153, 154], and we would expect the error

between $O(N)$ and exact diagonalisation to decrease.

Cell optimisation is fundamental to materials simulation and it raises the question: how well does $O(N)$ DFT compare to exact diagonalisation? Figure 5.2 compares two methods of defining a structural minimum: (i) minimum energy; and (ii) zero pressure structures[3]. Minimum energy lattice parameters were estimated by Birch-Murnaghan equation of states [150, 151] as implemented in `ASE` [152], whilst zero pressure was estimated by $2^{nd}$-order polynomial fit and root estimation in `SciPy` [155]. Unsurprisingly the minimum energy method generally outperforms the zero pressure method since we have ascertained pressure converges more slowly than energy with respect to **L**-range. However, it is interesting to note that *both* methods have an error of less than 1% for relatively small **L**-ranges, and whilst minimum energy results are more accurate, both offer a good approximation to the diagonalisation lattice parameter.

Elastic properties of materials is another important facet of materials research and our ability to do so on large structures is of particular importance to this thesis. Bulk moduli are found by the aforementioned Birch-Murnaghan equation of states fitting, taking energy-volume data as their input. Data presented in fig. 5.3 shows that bulk modulus is very well estimated for C, whilst reasonably well estimated for Si and Ge. Revisiting lattice (fig. 5.2) and energy (fig. 5.1(a)), a reason why the Ge bulk modulus appears to converge faster than Si beyond **L**-multiplier = 3.0 is not evident in the data. However, it is worth noting that lattice data around this **L**-range suggests volume convergence between them is close *and* Birch-Murnaghan equations of states are not particularly accurate [156], exhibiting sensitivity to initial guesses for volume and bulk modulus [157].

[3]Some data points in fig. 5.2 show troughs in lattice parameter convergence, however, these are due to absolute values of the differences being taken to make them representable on a logarithmic scale.

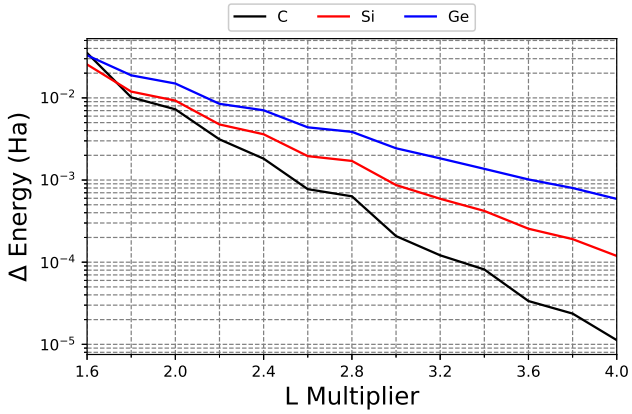


**(a)** Energy convergence.

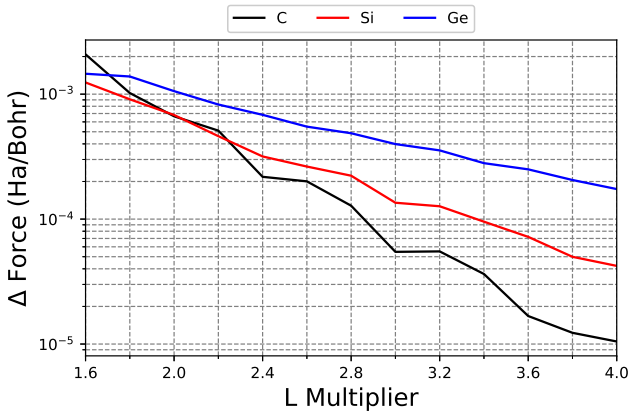


**(b)** Force convergence.

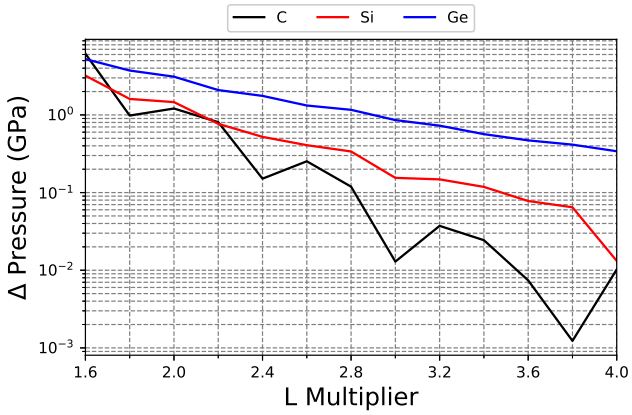


**(c)** Pressure convergence.

**Figure 5.1:** Error in convergence parameters from $O(N)$ as compared to diagonalisation for: (a) total energy; (b) forces; and (c) pressure. Diagonalisation total energies: C = -47.890984 Ha; Si = -39.589471 Ha; and Ge = -33.611024 Ha. Diagonalisation maximum forces: C = 0.03641 Ha/$a_0$; Si = 0.01435 Ha/$a_0$; and Ge = 0.01646 Ha/$a_0$. Diagonalisation minimum pressure: C = -0.1146 GPa; Si = 0.006180 GPa; and Ge = -0.008846 GPa.

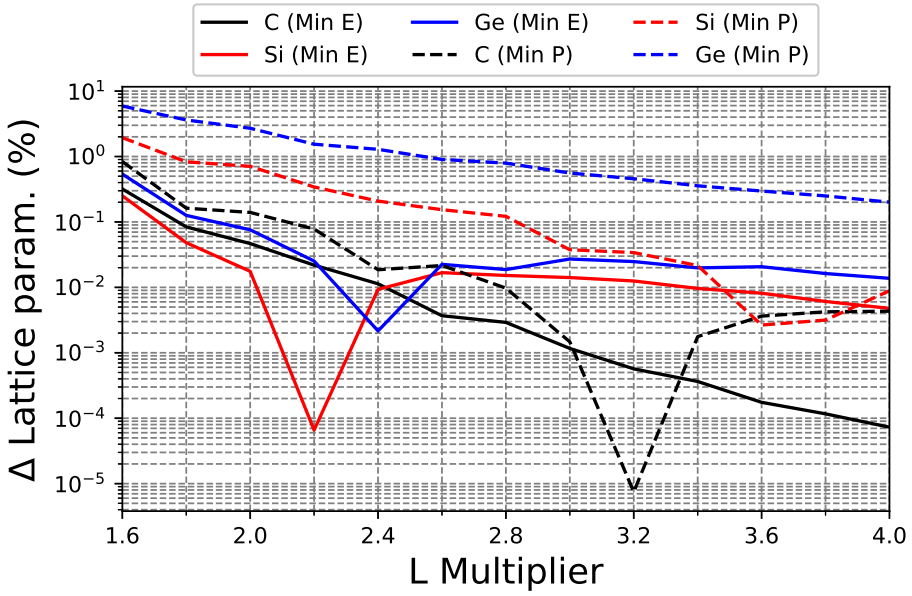


**Figure 5.2:** Error in $O(N)$ lattice parameter compared to exact diagonalisation. For each **L**-range, the optimal structure was found by either: (i) minimum energy structure (solid lines); or (ii) zero pressure structure (dashed lines). To enable calculation of the error magnitude the lattice parameters of diagonalisation are: C = 6.860546 Bohr; Si = 10.645583 Bohr; and Ge = 11.017632 Bohr respectively.

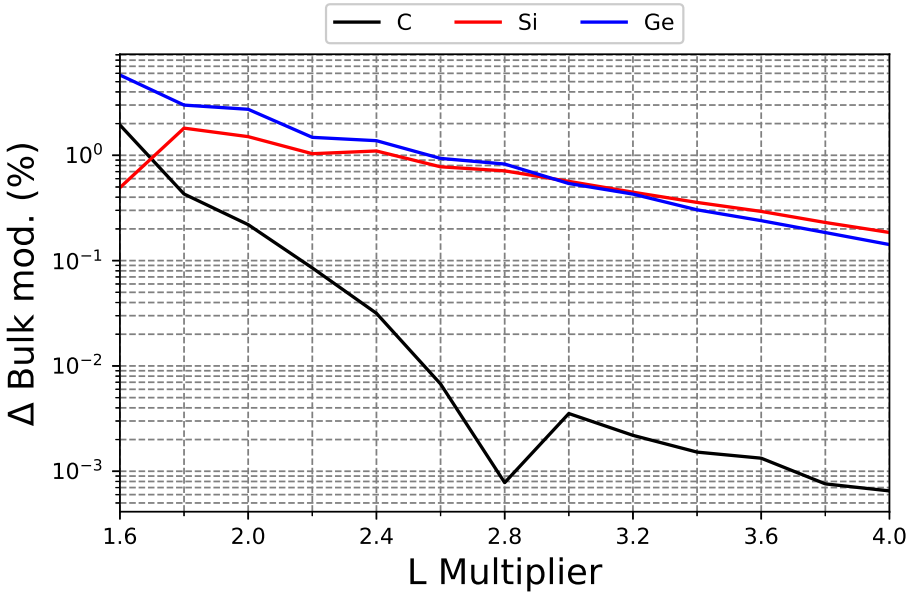


**Figure 5.3:** Error in $O(N)$ calculated bulk modulus as compared to exact diagonalisation. Bulk modulus was found by Birch-Murnaghan equation of states fitting, yielding exact diagonalisation results for: C = 393.874732 GPa; Si = 72.048677 GPa; and Ge = 50.967849 GPa.

## 5.4 Conclusion and further work

Locality of the density matrix is crucially important to the approximations made within $O(N)$ DFT, specifically the range at which the density matrix is truncated (**L**-range). This locality has been shown to correlate to the band gap of the materials being simulated, although there have been no studies quantifying the effects of **L**-range on the physical properties of materials. Figure 5.1 demonstrates convergence rate of forces $>$ energy $>$ pressure/stress, for structures which are equivalent (i.e. minimum energy for their density matrix solution method), and for practical $O(N)$ calculations the forces are reliable (within 10%) even with small **L**-ranges. We emphasise results in fig. 5.1 represent what would happen if you took a structure found from $O(N)$ and performed a static, self-consistent exact diagonalisation calculation to obtain those same physical parameters. In practice this means using an $O(N)$ structure to perform a one-shot band structure calculation (with exact diagonalisation) would be misrepresentative due to pressure induced from the truncation of **L**. Finally, both lattice parameters and bulk moduli have been shown to be well approximated with reasonably small **L**-ranges proving $O(N)$ DFT is accurate for structural calculation with modest **L**-ranges.

Since the decay rate of the density matrix is known to be proportional to the band gap of the material studied, one item for further work would be to calculate the band structures explicitly in order to generate parameters for the relationship between the two. In doing so it may be possible in future to provide future CONQUEST users with recommendations for the **L** range. However, a SZ basis has been shown to be inaccurate (chapter 3) for most structural parameters and $O(N)$ calculations with basis sets larger than SZP are not practical. At present the CONQUEST team are pursuing the development of so called *"on-site support functions"* which can reduce a large basis to a smaller one. Completion of that development will enable more accurate structural results afforded by increased variational freedom, but also a more meaningful description of the band gap. So, obtaining a general, queryable database to suggest **L**-range would be best *after* completion of the development of on-site support functions.

# Chapter 6

# Vegard's law and strain: An $O(N)$ DFT study of core – shell nanowires

Strain is a critical factor in the structural stability [158], optical [159] and electronic properties [37] of nanowires. Comparison of the lattice parameters of bulk Si and Ge reveals a lattice mismatch of approximately 4.2%, thus within Si-Ge nanowires there exists an intrinsic strain of the Si–Ge bonds forming the interface between the two which will ultimately modify the strain within the rest of the nanowire. Experimentally, the strain present in core-shell nanowires can be determined by X-ray diffraction (XRD) [28] and high-resolution transmission electron microscopy (HRTEM) [160]. However, theoretical literature on this subject is relatively sparse and centres around combining multiple experimental data sources with finite-element analysis [161–163] offering local strain data to a resolution of about 1.5 nm for very large nanowires.

Simulation of large structures is particularly computationally expensive, thus, any method that saves computational time is highly valuable in the simulation scientists arsenal. One such method is through the use of the empirical Vegard's law [164, 165], interpolating bulk lattice parameters weighted by number of atoms of a given species:

$$a_0^{lin} = \frac{N^{Si} a_0^{Si} + N^{Ge} a_0^{Ge}}{N^{Si} + N^{Ge}}, \tag{6.1}$$

where $N^X$ is the number of element $X$ in the simulation cell, and $a_0^X$ is the bulk

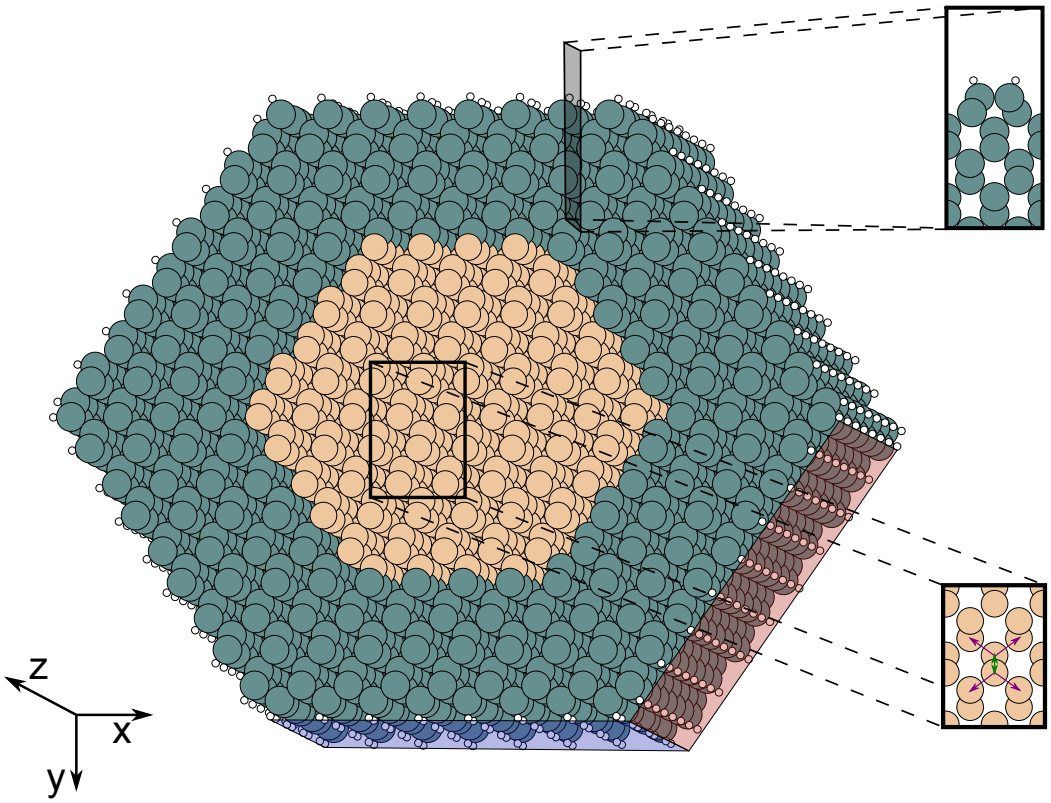


**Figure 6.1:** Perspective view along the axis of a Si (core) - Ge (shell) NW. Yellow spheres represent Si, green Ge and white hydrogen for the purpose of passivation. Red highlighted facet exhibits the $\langle 111 \rangle$ surface(s) and blue highlighted facet the $\langle 001 \rangle$ surface. Black highlight represents a slice along the axial direction, with inset showing the $(2\times1)$ surface reconstruction on the Ge $\langle 001 \rangle$ surface with dimer rows running perpendicular to the NW axial direction. Inset of the Si core shows bonding directions within our NW model, green arrows representing $\langle 001 \rangle$ and purple $\langle 111 \rangle$ bonding directions respectively.

lattice parameter of $X$.

A significant number of publications demonstrate that adherence to Vegard's law seems to be the exception rather than the rule [166–171]. Many factors, beside the fact it is empirical, have been proposed for deviations from Vegard's law: (i) the relative size of the constituent elements; (ii) the relative volume per valence electron; (iii) Brillouin-zone effects; and (iv) electrochemical differences between the elements [172]. Improved theoretical models since Vegard's original paper have been and continue to be proposed, however, a first comprehensive review by Gschneidner and Vineyard [173] found these models failed to predict the sign and magnitude of the deviations.

Whilst Vegard's law is often shown to be inaccurate, usage cases arise in experimental characterisation of core - shell nanowires. Stankevič *et al* used grazing-incidence X-ray diffraction (GIXRD) to measure the lattice constants of their shell material and thus estimate the composition and strain present by way of Vegard's law [174]. In another paper the spacing of Moiré fringes, measured by annular dark-field scanning transmission electron microscopy (ADF-STEM), were used to determine the Ge composition assuming Vegard's law holds true for the planar spacing of a $Si_{1-x}$-$Ge_x$ alloy and the Si core has the bulk Si lattice parameter [175].

Clearly, there is a need for large-scale structural investigations of surface reconstructed Si-Ge core-shell nanowires, a challenge CONQUEST and $O(N)$ DFT are best suited to. From the structural information above, experimental evidence supports the simulation of hexagonal $\langle 110 \rangle$ core-shell nanowires with $(2 \times 1)$ surface reconstructions on the $\langle 001 \rangle$ facets. A visual representation of our nanowire model can be found in fig. 6.1[1]. Section 6.1 outlines the parameters of our calculations. We shall then investigate the applicability of Vegard's law with respect to our nanowire models in section 6.2, assessing the deviation to axial lattice parameters predicted.

Production of local strain maps (section 6.3) will enable us to understand, at an atomic level, the complex strain fields present. Such strain mapping would enable us to determine areas of high strain and thus pin-point locations likely to produce dislocations and defects for strain relief [177]. It will aid the identification of regions of the wire where dopant stability is highest, for example Dunham *et al* [178] found that boron dopants diffuse most rapidly under tensile strain whilst arsenic is mobile under compressive strain and more stable under tensile strain. Additionally, they would be most beneficial to correlate with atomically projected density of states enabling a more detailed understanding of the influence of strain on the local electronic structure of given regions.

[1]This chapter was published in collaboration with Dr. C. O'Rourke [176]. He provided me with the initial structure files generated with his code and performed calculations on the Ge (core) - Si (shell) nanowires, whilst I took responsibility for the Si (core) - Ge (shell) nanowires calculations.

| NW Size | $N^{Si}$ layers | $N^{Si}$ atoms | $N^{Ge}$ layers | $N^{Ge}$ atoms | $N^{tot}$ atoms |
|---|---|---|---|---|---|
| 3-3 | 3 | 160 | 3 | 372 | 612 |
| 3-5 | 3 | 160 | 5 | 740 | 1004 |
| 3-7 | 3 | 160 | 7 | 1204 | 1492 |
| 6-3 | 6 | 532 | 3 | 588 | 1236 |
| 6-5 | 6 | 532 | 5 | 1100 | 1772 |
| 6-7 | 6 | 532 | 7 | 1708 | 2404 |

**Table 6.1:** Table showing the number of layers and number of atoms in each simulated NW structure examined by $O(N)$ in our paper [176]. The axial direction of the NW simulation cell contains *two* $\langle 110 \rangle$ oriented primitive cells of Si/Ge yielding an axial cell length of $\sqrt{2}\, a_0$ , where $a_0$ is the relaxed bulk lattice vector length of Si.

## 6.1 Computational details

All calculations performed in this section were done so with the Perdew, Burke and Ernzerhof [60, 61] (PBE) generalised gradient approximation. We chose to relax these structures using the $O(N)$ method to find solutions to the density matrix as detailed in section 2.7.2. The $O(N)$ method requires the use of smaller basis sets in part due to difficulties inverting the overlap matrix. As a result, the largest basis sets that were able to be used were single-$\zeta$ with one polarisation function (SZP).

To generate these basis sets we used the ATOM code (V3) with Troullier – Martins [129] pseudo-potentials, both of which were provided with the SIESTA source code [83]. As we have discussed in chapter 3 and presented in our paper [103], smaller basis sets require a judicious choice of confinement energy when being generated to accurately reproduce bond lengths associated with the pseudo-potential they were generated from. To tune these basis sets such that they reproduced plane-wave bond lengths we found confinement energies of 700 meV for Si/Ge and 300 meV for H to be sufficiently close (approximately 1%) to plane-wave values.

Structures used were generated using an in-house code[2] which included a 13 Å vacuum separation between periodic images of the simulated nanowires[3]. and

[2]Written by Dr Conn O'Rourke.

[3]This was known to be sufficient spacing between images since the largest matrix range (see section 2.7.2) was always smaller than this.

details of specific NW composition and size can be found in table 6.1. Initial structures were built with relaxed bulk silicon bond lengths, and so initial structures are far from equilibrium values. To improve computational time efficiency, structures were first relaxed with SZ basis sets to a force tolerance of approximately 0.26 eV/Å (0.005 Ha/$a_0$) before being completely relaxed with SZP to a force tolerance of 0.026 eV/Å (0.0005 Ha/$a_0$) using the *"fast inertial relaxation engine"* (FIRE) of Bitzek *et al* [179]. To maintain a balance between computational cost and accuracy, we found an *L*-matrix cut-off of 16 $a_0$ and real-space integration grid cut-off of 100 Ha sufficient such that bond lengths of bulk Si and Ge were well reproduced.

## 6.2 Applicability of Vegard's law to nanowires

In our published work, both Si (core) - Ge (shell) and Ge (core) - Si (shell) nanowires[4] were used to study the effect of varying core-shell composition ratios on the relaxed (minimum energy) NW structures found [176]. We test two core and three shell sizes such that a range of strain environments are present; in the case of 3 core layers we gain an understanding of the strain environments passed through under longer shell deposition times and the larger 6 layer core explores the transition from thin shell environment to one comparable with the 3-3 structure.

It is unusual to see Vegard's law applied to chemical environments outside the context of alloys, however, owing to the growth methods employed (VLS) and characterisation methods it is important to quantify such a deviation. Atomistic modelling enables control of simulation composition not otherwise afforded to experimentalists. The results found in this chapter will provide us with a ceiling measurement of the deviation from this simple linear interpolation, and quantify if such usage is unwise.

Misuse of Vegard's law is not without precedent, for example Nduwimana *et al* present a study of core - shell and multishell $\langle 111 \rangle$ nanowires relaxed such that all forces and stresses were minimal [36]. It is well documented that $\langle 111 \rangle$ oriented Si nanowires are only observed beyond 20 nm diameter [22–24] casting

[4]Ge (core) - Si (shell) calculations were carried out by Dr Conn O'Rourke and *will not* be presented in this thesis.

doubt over how physically "correct" these structures are. Furthermore, comparisons were drawn between their structures and those predicted by Vegard's law which they claim "agree with predictions from Vegard's law"; however, these claims were unsubstantiated.

In order to quantify how well Vegard's law predicts the axial length of core-shell NWs, we define the percentage difference between the minimum energy axial length we find and the Vegard's law prediction as follows,

$$\delta l(\%) = \frac{a_0^{min} - a_0^{lin}}{a_0^{min}} \times 100 \tag{6.2}$$

where $a_0^{min}$ is the axial length found by simulations and $a_0^{lin}$ from Vegard's law. This equation represents the percentage difference relative to the optimal structure, however, in the literature it may be found relative to Vegard's law [171]. Thus eq. (6.2) is the percentage that Vegard's law differs from structures found by DFT, and a negative number indcates an overestimation by Vegard's law.

One departure from our published work, summarised in the caption of table 6.2, was to include Vegard predicted axial lengths individually calculated from an equation of state fittings of bulk Si and Ge. This has been done to enable direct comparison between our calculated NWs and Vegard predicted axial lengths since the methods used to find bulk lattice parameters and optimal NW structures are equivalent. Thus we may take advantage of fortuitous error cancellation owing to the identical methods through which our structures were found and will not comment further on the percentage deviation published within our paper.

We present our results in table 6.2. We find that for the NWs with 3 core layers the percentage deviation is approximately 1%, the smallest value attributed to the smallest shell and the largest value to the largest shell. This shows a monotonic increase in the deviation, although the rate of increase is not linear and becomes more rapid with an increasing Ge shell size. The larger 6 layer core NWs show a dramatic increase in the deviation from Vegard predictions from the smallest shell to the next largest although this behaviour is not monotonic and the largest shell, whilst having a significant deviation is marginally smaller than the middle sized

| $N$-core layers | $N$-shell layers | % Ge comp. | $a_0^{min}$ (Å) | $a_0^{lin\dagger}$ (Å) | Dev.$^\dagger$ (%) | $a_0^{lin}$ (Å) | Dev. (%) |
|---|---|---|---|---|---|---|---|
| 3 | 3 | 70 | 5.593 | 5.590 | 0.054 | 5.648 | -0.983 |
| | 5 | 82 | 5.619 | 5.628 | -0.160 | 5.619 | -1.050 |
| | 7 | 88 | 5.624 | 5.631 | -0.125 | 5.692 | -1.209 |
| 6 | 3 | 52 | 5.574 | 5.549 | 0.449 | 5.606 | -0.574 |
| | 5 | 67 | 5.532 | 5.584 | -0.940 | 5.642 | -1.988 |
| | 7 | 76 | 5.565 | 5.604 | -0.701 | 5.663 | -1.761 |

**Table 6.2:** Departure from Vegard's law for Si (core) - Ge (shell) NWs determined through $O(N)$ structural relaxation. Axial lengths of relaxed NWs were found by cubic spline fitting of energy against axial length. Two sets of linearly interpolated results are presented here, $a_0^{lin\dagger}$ and $a_0^{lin}$, with daggered results indicating those presented in our paper. Results produced in our paper used Si and Ge experimental lattice parameters for calculation of $a_0^{lin\dagger}$, using values $a_0^{Si} = 5.432$ Å and $a_0^{Ge} = 5.658$ Å respectively [181]. With hindsight, more suitable lattice parameters to calculate deviations would be those found from equation of states fitting of bulk Si and Ge, using the same basis and calculation parameters as in section 6.1. For reference these are $a_0^{Si} = 5.4807$ Å and $a_0^{Ge} = 5.7202$ Å respectively.

core.

Yano *et al* [180] found that $\langle 110 \rangle$ Ge (core) - Si (shell) NWs also show deviations from Vegard law predictions for NWs with a fixed number of atoms, varying core Ge content, with strong deviations between 40-80%. Recasting the interpretation from a layer based NW size to a fractional composition using information from table 6.1 sheds some light on the behaviour presented in table 6.2. Comparison of the similar NW compositions of 3-3, 6-5 and 6-7; again, the magnitude of deviations for small and large cores do not seem to correlate. It is clear that the deviation from Vegard's law is not a simple function of the number of atoms, but a complex interplay between the number of atoms present and respective core/shell sizes. It is also interesting to note that the thin shelled 6-3 NW show the closest agreement with Vegard's law. This suggests that in the thin shell limit, where the Si-Ge composition is approximately 1 : 1 *and* the effect of a shell half as thick as the core, results in Vegard's law predictions which are close to minimum energy structures, but not completely reliable.

## 6.3 Strain maps of $O(N)$ structures

Our method for representing local strain compares the Si–Si and Ge–Ge bond lengths in NWs to that of their respective relaxed bulk counterparts. Figure 6.1 illustrates a typical NW studied, highlighting two unique bonding directions with components along the radial cross-section. Local strain mapping figures were produced by determining bonding direction, comparing bond lengths to bulk and projected on to a grid such that pixel colouring may be defined according to their local strain data[5]. Figures are separated into core and shell regions to facilitate strain calculation, then further separated by which bonding direction they represent in order to readily present strain anisotropy, see core-centred inset in fig. 6.1 for a visual representation. Bonds oriented in the $\langle 001 \rangle$ exhibit mirror symmetry about the line drawn between $\langle 111 \rangle$-$\langle 111 \rangle$ vertices, so data presented in these strain maps are the bonds oriented from the bottom $\langle 001 \rangle$ facet to the top $\langle 001 \rangle$ facet. Bonds in the $\langle 111 \rangle$ direction are more complex, they too have mirror symmetry about the same line as the $\langle 001 \rangle$ in addition to mirror symmetry about the $\langle 001 \rangle$ bonding direction, thus, the bonds presented in $\langle 111 \rangle$ strain maps are those pointing toward the upper-right $\langle 111 \rangle$ surface. It should be noted that strain maps in equivalent bonding directions are identical to those presented with the exception of the symmetry relations outlined, i.e. they are mirror images of one another. Strains calculated in this section use the experimental lattice parameters as references for bulk Si and Ge, $a_0^{Si} = 5.432$ Å and $a_0^{Ge} = 5.658$ Å respectively [181].

Figure 6.2 shows the strain maps for bonds oriented in the $\langle 001 \rangle$ direction, we note the expansion on the surface of the $\langle 001 \rangle$ facets is a consequence of our methods for determining the local strain and our inclusion of $(2\times1)$ surface reconstruction in our method. Note the absence of tensile strain in the larger (6-X) core sizes as compared to the small core sizes, regardless of shell size. We attribute this to small (3-X) Si core sizes having an equal or larger number of Ge layers, however, the result is not seen in the 6-7 NW where a slightly larger number of Ge shell layers are present. We suggest this different result is due to the interplay of surface and/or

[5]Code used to produce figures in this section was written by Dr Conn O'Rourke. A version, modified by the author, can be found in appendix A.3.

interface effects. It is well known that Ge is elastically softer that Si, at least with respect to the bulk modulus as calculated by the CONQUEST team [103], thus we postulate this effect will resurface in the case of more Ge layers requiring further investigation to verify.

In fig. 6.3 we show the strain maps of the $\langle 111 \rangle$ oriented bonds, the specific bond direction represented here is the bond pointing toward the upper-right $\langle 111 \rangle$ surface. The effect of this high tensile core strain is most striking in the 3-5 structure, having a Ge composition of approximately 82% followed by the 6-7 (76% Ge), 3-7 (88% Ge) and 3-3 (70% Ge) models. These are compositions where the core and shell thickness are approximately equivalent, and their high strain environment will have a significant effect on the resultant electronic structure.

Turning to the core, figs. 6.4 and 6.5 show that for all bonding directions considered they are all under significant tensile strain, in agreement with previous theoretical [182] and experimental [28] works. This effect can simply be explained by the larger bulk lattice parameter of Ge compared to Si, and that increasing shell thickness drives Si core bonds toward bulk Ge lengths. Small core (3-X) NWs show no compelling change in $\langle 001 \rangle$-bonds with increasing core thickness, however, the 6-5 core exhibits a slight reduction in tensile strain as compared to 6-3 and 6-7 NWs. Bonds in $\langle 111 \rangle$ mirror this trend albeit with a smaller reduction in strain for the 6-5 model compared to the $\langle 001 \rangle$-bonds. This indicates a complex strain relaxation where thin shells induce strong tensile strain in the core, most likely due to surface effects. However, this is not conclusive since a fuller description of these effects would require studying significantly more thin shell regimes.

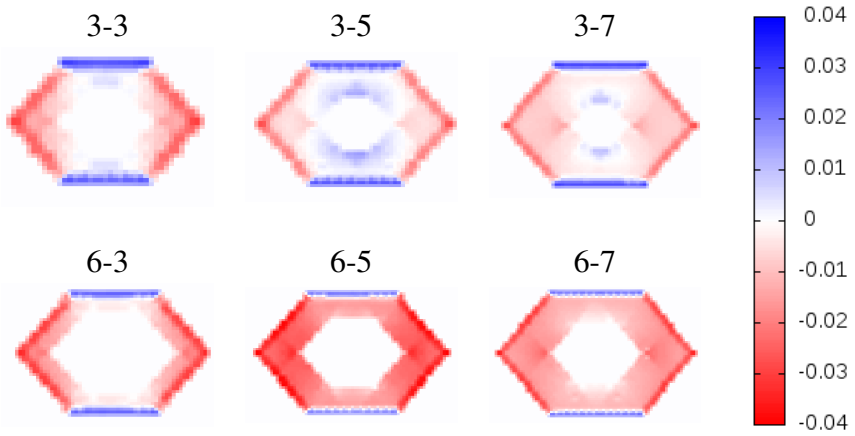


**Figure 6.2:** $O(N)$ structures: Local strain mapping of shell regions: $\langle 001 \rangle$ bond direction. Bonding direction presented here can be found visually on the structure in fig. 6.1 represented by green arrows in the inset.

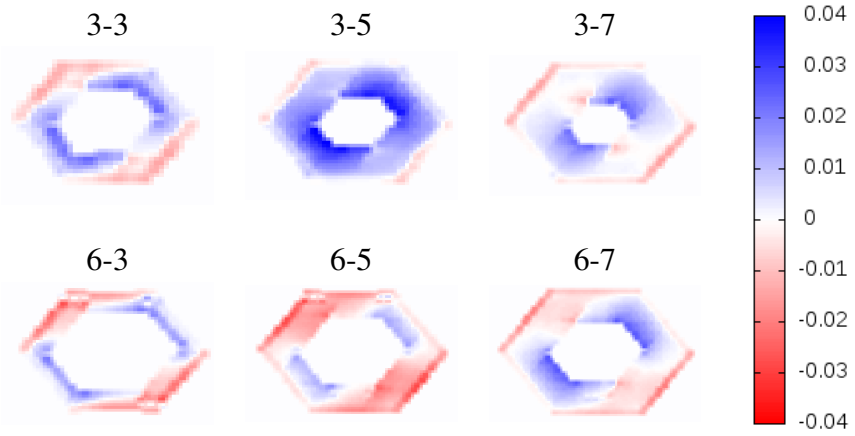


**Figure 6.3:** $O(N)$ structures: Shell map of $\langle 111 \rangle$ bond direction. Bonding direction presented here can be found visually on the structure in fig. 6.1 represented by purple arrows in the inset, although there are four equivalent directions, this figure specifically references the north-eastern pointing arrow.

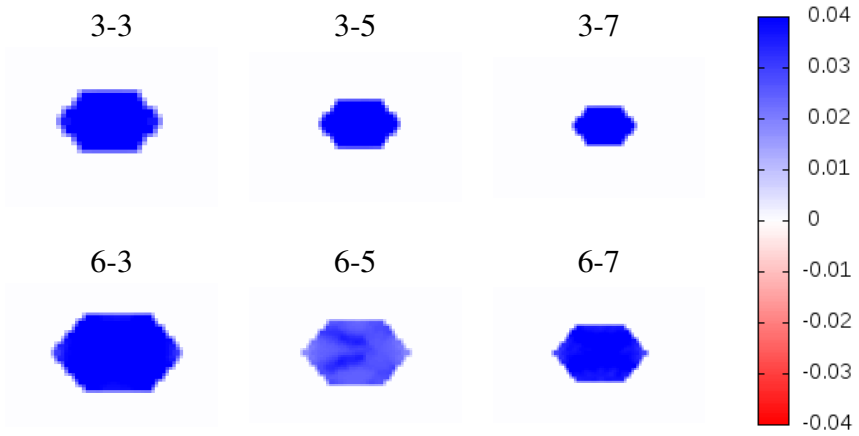


**Figure 6.4:** $O(N)$ structures: Core map of $\langle 001 \rangle$ bond direction. Bonding direction presented here can be found visually on the structure in fig. 6.1 represented by green arrows in the inset.

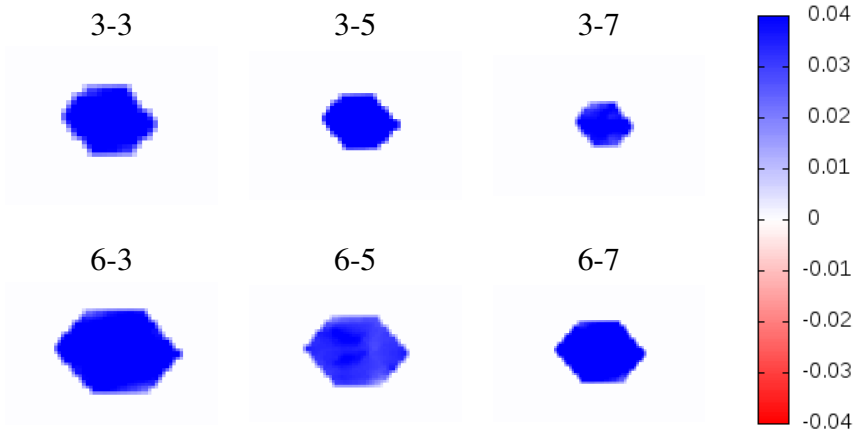


**Figure 6.5:** $O(N)$ structures: Core map of $\langle 111 \rangle$ bond direction. Bonding direction presented here can be found visually on the structure in fig. 6.1 represented by purple arrows in the inset, although there are four equivalent directions, this figure specifically references the north-eastern pointing arrow.

## 6.4 Discussion and concluding remarks

We find that Vegard's law consistently over estimates the axial lattice parameter of Si (core) - Ge (shell) nanowires (as also noted in Ref. [34]) for small $\langle 111 \rangle$ nanowires. Additionally, non-monotonic behaviour of the optimal axial lattice parameter was observed for (6-X) models, as seen for thick-shell NWs in Refs. [182, 183]. We propose this is an interesting transition behaviour where there are competing elastic effects of the surfaces and interfaces, but further work would be required to form a more complete theory. Overall, the deviations from Vegard's law found in this work indicate it is not suitable for use in simulation of nanowires since axial strains would be in the region of 0.5%-2% and would yield quite poor atomic and electronic structure. With regard to the experimental usage of Vegard's law, this is highly dependent on the system studied and error estimated, for which our results represent an upper threshold since they are quite the opposite of the uniformly mixed solution Vegard's law may approximate well.

The results presented in this chapter are essential data for the core-shell regime, particularly due to the highly anisotropic strain distributions presented and lack of data for nanowires above 5 nm in diameter [34]. Developing an understanding of the strain environments present in nanowires is pivotal to the development of nanowire devices, since they will dictate the magnitude of the band gap and charge carrier mobilities [184, 185]. Furthermore, detailed strain mapping could be combined with electronic structure to shed light on the nature of this complex relationship. For example, Meng *et al* used experimental strain mapping to detect shifts in the direct band gap transition energy in the Ge core, resulting in improved optical emission [163].

Stress maps in this chapter demonstrate that Si (core) - Ge (shell) nanwoires show high anisotropy in the shell and nearly isotropic tensile stress in the core. The high strain in the core region suggests that the types of nanowires may become prone to dislocations in the core and diffusion enhanced at the interface. Furthermore, we have identified a bounded compositional region, 75-85% Ge, whereby the strain at the interface is largest in the $\langle 111 \rangle$ direction. Silicon and germanium are

known to be mechanically anisotropic with the Young's modulus of $\langle 111 \rangle > \langle 110 \rangle > \langle 001 \rangle$ [186], so it is interesting that the largest strains in the shell are in the stiffest direction. This suggests the reconstructions on the $\langle 001 \rangle$ surfaces may aid resisting strain.

We have performed structural relaxations on very large systems of nanowires with surface reconstructions on the $\langle 001 \rangle$ facets, necessitating the use of $O(N)$ DFT calculations. We have found the optimal axial lattice parameters of such systems and compared these to predictions made by Vegard's law, from which we have found large deviations that should be considered in future simulation and experimental works. To aid future electronic structure works on core-shell nanowires, we have produced strain maps which may be useful for analysis of electronic structure in addition to further works that would investigate doping of nanowires where dopant location is know to favour particular strain conditions.

# Chapter 7

# Mechanical properties of Si (core) - Ge (shell) NWs

## 7.1 Introduction

The mechanical properties of nanowires are relatively unknown in comparison to studies of their synthesis and electronic properties. Whilst not as obviously useful to electronic devices as studies into electronic properties they are eminently important to their growth and device processing where issues such as delamination, of the core and shell layers, could result in device failure [187]. However, this gap in the literature has little to do with how useful mechanical properties are but how challenging measurements are to perform due to the growth methods.

Estimation of the Young's modulus will require measurement of the nanowire length, cross-sectional area and force applied to achieve some deformation. Since nanowires are generally grown via VLS deposition on surfaces, measuring these properties will require access for AFM tips to measure these properties and apply force. If there is a sufficiently low density of nanowires on the surface, it is possible for the AFM tip to make contact with the substrate and (whilst in contact mode) sweep over the top of the nanowire applying a constant force until discontinuity in AFM tip deflection is detected [188]. That method will require SEM and/or TEM images to estimate the average diameters before AFM takes place and will be a relatively large approximation if the system under study is non-uniform. Other methods

will require nanowires to be cleaved from the substrate, moved, measured and then affixed either to AFM tips (axial deformation) [189] or crossing a trench (lateral deformation) [190] to determine the Young's modulus. Whilst these methods are more accurate than the AFM tip sweeping method they are significantly more time consuming and difficult.

Chapter 6 presents the optimal structures of Si (core) - Ge (shell) nanowires that were obtained through $O(N)$ calculations to build an understanding of the strain fields present and ascertain if usage of Vegard's law is appropriate when applied to nanowire simulation. At the time of conducting that research, $O(N)$ calculations were the only way to do such large calculations within a reasonable time-scale. However, in Chapter 5 we found that quantities based on derivatives of energy (i.e. forces and stresses) can converge slowly with respect to density matrix range. Convergence of stresses and forces have an inverse relationship with the magnitude of the band gap which may not be known *a priori*, i.e. small gaps result in even slower convergence with respect to band gap (discussed in Chapter 5).

This does not undermine the results presented in Chapter 6, although, investigation of the mechanical properties of nanowires would call for the use of Hamiltonian diagonalisation as the density matrix solution method of choice. Studies of the size presented in this thesis (1000-2000 atoms) are possible for plane wave DFT or Hamiltonian diagonalisation with a good *primitive* basis set but are extremely computationally expensive and inefficient. However, development of MSSFs (see Section 2.8.2) reduces the computational cost and increases the efficiency of Hamiltonian diagonalisation to an extent that systems larger than 1000 atoms are achievable within a tangible time-scale.

Whilst DFT studies exist on the mechanical properties of Si, Ge and Si-Ge nanowire systems none have investigated the effects of surface reconstructions of core-shell structures. To obtain the Young's modulus of Si (core) - Ge (shell) nanowires we must define and discuss nanowire volume (Section 7.3.1) and force tolerances (Section 7.3.2) required for accurate calculation of the Young's modulus (Section 7.3.3). In addition to the Young's modulus, we determine another closely

related mechanical property, the Poisson ratio presented in (Section 7.3.4). Finally, we shall circle back to the applicability of Vegard's law (Section 7.3.5) and maps of the strain field (Section 7.3.6) to quantitatively compare results between $O(N)$ and diagonalisation modes of operation.

## 7.2 Computational details: MSSF NW structures

In Chapter 3 we have demonstrated that "primitive" CONQUEST basis sets are able to reproduce mechanical properties with plane-wave accuracy, however, basis sets with a large number of support functions make calculations of greater than 1000 atoms computationally expensive. This is due to the cubic scaling in time and quadratic in memory of the Hamiltonian diagonalisation method with respect to the number of support functions. Multi-site support functions (MSSFs) provide a solution to this issue by reducing the size of the Hamiltonian, converting primitive PAOs to orbitals that factor in neighbouring atoms within a set of specified ranges [84]. The MSSF range defines the distance from the central atom for which the MSSF is constructed, whilst the localised filter diagonalisation (LFD) range defines the range used to update the coefficients of the MSSFs (see section 2.8.2 and references therein). Since the MSSF methodology uses neighbouring atoms to construct support functions, they are free of the point symmetry constraints of PAOs and thus we may contract arbitrarily large PAOs on to a minimal number of multi-site support functions. Whilst this doesn't change the scaling of the methodology we are able to reduce the number of support functions used for calculations in exchange for an overhead in constructing and updating coefficients.

Further developing the MSSF methodology, variational optimisation of the coefficients was later applied to the MSSFs by Nakata, Bowler and Miyazaki [87]. It was found that with small MSSF and LFD ranges this optimisation brings significant gains in accuracy of simulation at the cost of an increase in computational effort. However, with larger ranges accuracy can be close to that of the "primitive" basis, and optimisation brings little improvement to the accuracy of calculations. For calculations presented in this chapter and Chapter 8, LFD and MSSF ranges

were chosen such that variational optimisation of coefficients offers negligible improvement. There is one additional development utilised, with respect to calculations with MSSFs; the introduction of the "mixed SCF-LFD" method. The original MSSF method performs an LFD cycle to completion then progresses to a full SCF cycle, these two full cycles are repeated until the charge density is converged. Mixed SCF-LFD inter-locks *one* step from SCF and *one* step from the LFD cycles, iterating until the charge density is converged. This method greatly reduces the total number of SCF and LFD steps required to find a self consistent charge density and has been employed for the structural calculations presented in this chapter.

All calculations presented in this chapter were performed with optimised norm-conserving Vanderbilt pseudopotentials using ONCVPSP code v3.2.3 [130] and Perdew-Burke-Ernzerhof generalised gradient approximation exchange-correlation functionals [60, 61]. Triple-$\zeta$, triple-polarisation basis sets were generated using the CONQUEST basis generation suite[1] using the equal radii confinement method as detailed in Chapter 3 and Ref. [103]. Using a test system of 276 atoms, representing a small 2-2 core-shell nanowire, we determined LFD and MSSF ranges of 12 $a_0$ agree well with the primitive basis. An integration grid of cut-off 100 Ha and $1\times5\times1$ Monkhorst-Pack k-point mesh[2] offer excellent accuracy for structural relaxation based upon convergence of the forces and total energy. Determination of the axially relaxed NW structures (created as per section 6.1) uses multiple reference structures, scaled along their axis, and their atomic positions are relaxed for fixed simulation cell sizes.

## 7.3 Elastic properties of Si (core) - Ge (shell) ⟨110⟩ nanowires

The growth direction of nanowires are fundamentally important to the mechanical and electronic structure of nanowires; and are strongly correlated to resultant wire diameter. Pure Si nanowires grow almost exclusively along the ⟨110⟩-direction for

[1] A pre-release version which does not include a referenceable version number, but will not affect the results presented.

[2] Approximate k-point spacing 0.081-0.084 $a_0^{-1}$.

wire diameters in the region of 3-10 nm [22] and thermodynamic models suggest this growth direction still dominates over ⟨111⟩ up to a diameter of 20 nm [23, 24]. For elemental Ge nanowires with diameters of 4-30 nm the ⟨110⟩-direction is preferred to ⟨111⟩ or higher index directions [191].

Core-shell Ge (core) - Si (shell) ⟨110⟩ nanowires have been synthesised with diameters ranging from 20-50 nm, where the growth direction of samples was confirmed by high-angle annular dark-field (HAADF) STEM imaging [192]. Theoretical studies using classical potentials typically model wires with diameters around 3 nm [180, 192, 193], although more recently as large as 10 nm [194]. DFT studies are typically of 0.5-4 nm in diameter and focus mainly on the effect of strain on the magnitude of the band gap rather than propertes such as the Young's modulus [182, 183, 195]. In all of the theoretical literature only Deb Nath *et al* [194] have examined structures of a similar size to those found experimentally and none have considered the effects of surface reconstructions. In this section we present the mechanical properties of our ⟨110⟩ Si (core) - Ge (shell) nanowires, with surface reconstructions, for wires between 5-9 nm in diameter.

### 7.3.1 Defining the nanowire volume without ambiguity

Calculation of nanowire cross-sectional area is not unambiguous. Generally, the cross-section is approximated by a circle and the decision to include [196] or exclude [19] the passivation layer have both been presented in the literature. The relative error associated with determining the Young's modulus by circular cross-section has been quantified by Leu *et al* [197]. Consider a nanowire such that the radius is $r_0 + \delta r_0$:

$$Y' \approx Y(1 - \frac{2\delta r_0}{r_0}) \tag{7.1}$$

where $Y$ is the Young's modulus and $Y'$ the modulus associated with $r_0 + \delta r_0$. Thus, in the limit $r_0 \to \infty$ the error is small. However, for the Poisson ratio ($\nu$) with this definition of the radius,

$$v' \approx v(1 - \frac{\delta r_0}{r_0} + \frac{\delta r - \delta r_0}{r - r_0}) \tag{7.2}$$

the second term in brackets tends to zero in large nanowire limit, i.e. $r_0 \to \infty$. The third term will be present regardless of the magnitude of $r_0$ and can be significant in the typical case $r - r_0$ is small.

Whilst approximating the cross-section as a circle is not completely unreasonable, it does introduce an ambiguity; what atoms should be included/excluded from the calculation of the cross-sectional area? Figure 7.1 shows two dashed circles, one chosen to pass through ⟨001⟩-⟨111⟩ vertices and the other passing through ⟨111⟩-⟨111⟩ vertices. In the first case, a number of nanowire atoms are excluded (not just the passivation layer) and in the second case a large amount of vacuum has been included. Both cases will result in a poor approximation to the Young's modulus and Poisson ratio, and any choice of radius between these two could be chosen arbitrarily.

We define the cross-section by fitting the solid blue lines to the surfaces of the nanowires (see Figure 7.1), finding their corresponding equations which are used to find the points of intersection. With this information we divide the cross-section into four triangles and apply Hero(n)'s formula to calculate the cross-sectional area,

$$s = \frac{a+b+c}{2} \tag{7.3}$$

$$A = \sqrt{s(s-a)(s-b)(s-c)} \tag{7.4}$$

where $s$ is the *semi-perimeter* of the triangle with side lengths $a, b, c$ and $A$ the area of such a triangle. From this point, volume calculation is the sum of the triangle areas scaled by the length of the simulation cell. Our method calculates the area more precisely, compared to that of Leu *et al* [197] and is unambiguous in the choice atoms included. Our calculations presented in Sections 7.3.3 and 7.3.4 exclude the passivating H atoms since the bond angle made between the H atom and surface species varies as we traverse the surface, in particular the ⟨111⟩ surfaces.

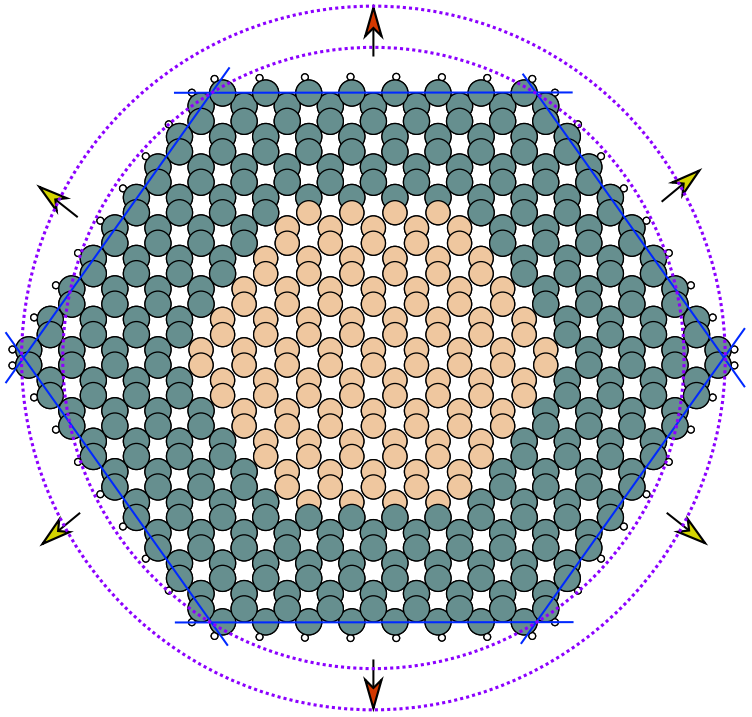

**Figure 7.1:** View along the axial direction of a ⟨110⟩ nanowire, illustrating the planes which were fit to the atoms in the surface (solid blue lines). Planes were determined from the atomic coordinates of three atoms in that specific surface. Note that planes bisect the outer-most circles representing the atoms in the surface, this is due to the planes being defined by atomic coordinates. Purple dashed lines indicate the method used by Leu *et al* [197] to determine the error in the Young's modulus. Yellow filled arrows indicate the ⟨111⟩ direction and red arrows the ⟨001⟩.

This would reintroduce some arbitrary choices about which of the passivating atoms to use for our methodology, contrary to the objective of our method.

### 7.3.2 Quantifying convergence of nanowire structures

Finding the relaxed axial length of our nanowire structures is the ultimate goal of this chapter to facilitate the electronic structure calculations in chapter 8 of axially relaxed structures. To find these axially relaxed structures we scale a structure along its axis to create a sample point, and using many sample points, relax the atomic positions with a fixed axial length. During initial analysis of stress and strain data used to find the Young's modulus (methodology details in Section 7.3.3), we found that the conventional force tolerance of 0.02 eV/Å resulted in poor fitting to stress-strain curves, predicting optimal nanowire lengths which had residual axial stresses

of more than 0.1 GPa. Further investigation elucidated oscillatory fluctuations in the total energy and volume of our axially strained wire models, suggesting that either further convergence metrics or tighter force tolerances are required to obtain optimal structures with the desired axial stress threshold, indicating poor structural convergence.

We proposed a simple volume residual, i.e. $V_i^{res} = |V_{i+1} - V_i|$ where $i$ is the step number, could be a suitable candidate for an additional metric to the maximum force (see Figure 7.2(a)). However, we found no clear value of the residual that resulted in a more accurate stress-strain curve, indicating this is not a suitable additional metric for core-shell NW structure prediction. In order to obtain the final structures to calculate the Young's modulus in Section 7.3.3 simply requires the use of tight force tolerances, $0.19 \times 10^{-3}$ Ha/$a_0$ (0.01 eV/Å) to obtain the fitting accuracy achieved in see Figure A.2.

As a diagnostic measure we tried plotting the difference between the $i^{th}$ step and the final step volume, i.e. for $n$-steps to reach a force tolerance $V_i^{res} = |V_i - V_n|$, see Figure 7.2(b), we find nanowires with axial lengths close to the optimal value converge in fewer conjugate gradient steps. Input structures (step 0) were constructed by scaling a single nanowire structure with bond lengths equal to relaxed bulk silicon, where scaling of atomic positions was only applied in the axial direction. Whilst it is not possible to know the optimal axial length of a zero stress nanowire *a priori*, we may be able to precondition the initial structures of future nanowire calculations using the Poisson ratios presented in Section 7.3.4. However, we conclude that the data in Figure 7.2(b) does nothing more than illustrate that our initial scaled nanowire structures converge most quickly when their axial lattice parameter is closest to the *ideal* axial length.

### 7.3.3 Young's modulus of core-shell nanowires

At least four factors affect the Young's modulus of core-shell nanowires: (i) diameter; (ii) composition; (iii) growth direction; and (iv) the presence of an oxide surface layer. The presence of an oxide surface layer reduces the Young's modulus since Si or Ge oxides are elastically softer than pure elemental crystals [198, 199], how-

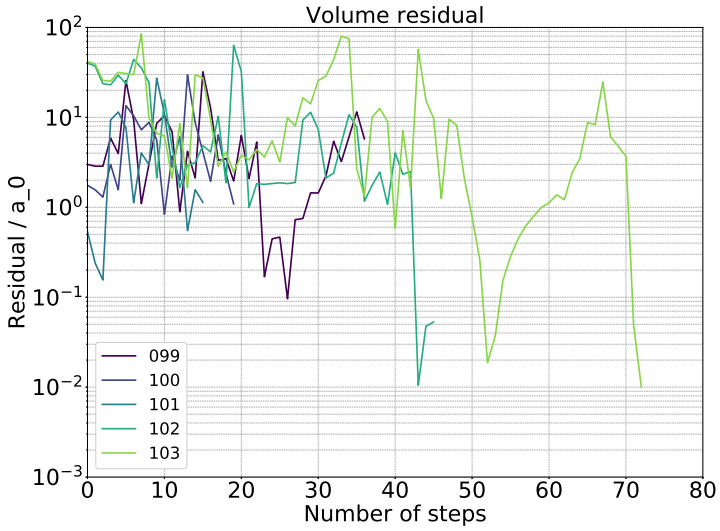


**(a)**

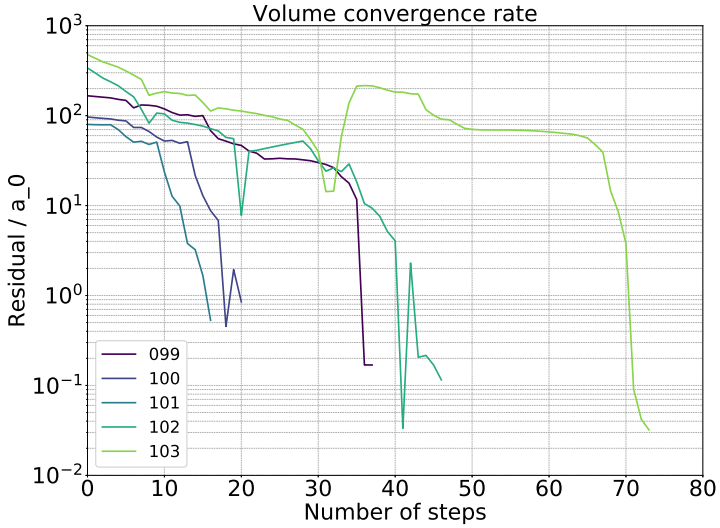


**(b)**

**Figure 7.2:** Proposed volumetric metrics for identifying the ground state: (a) simple volumetric difference between concurrent steps; (b) the difference between volumes of the $i^{th}$ step and the final step. The data shown is for the 4-4 *axially scaled* NW models and the legend labels are related to the percentage scaling of the initial NW axial length ($a_0^{Si} \times \sqrt{2}$ where $a_0^{Si} = 5.5002$ Å).

ever, we shall not be investigating this. The growth direction also plays a significant role in the resultant nanowire stiffness, where $\langle 111 \rangle > \langle 110 \rangle > \langle 001 \rangle$ [200, 201]. Whilst the growth direction and presence of an oxide layer present interesting opportunities for future research of core-shell nanowires, they are beyond the scope of this thesis.

Single element nanowire diameters in the range of theoretical study, less than 10 nm, have a strong effect on the Young's modulus generally becoming stiffer with increasing diameter [19, 184, 196, 197]. However, the majority of the experimental literature, wires between 50-100 nm in diameter, show the Young's modulus is independent of diameter [20, 202, 203]. Studies on core-shell nanowires are limited to theoretical calculations using empirical (Stillinger-Weber and Tersoff) potentials and focus on the effects of composition on *fixed* diameter wires around 3 nm in diameter [180, 193]. The issue with these two studies are: (i) wire diameters considered require most core widths to be smaller than those experimentally possible; (ii) in the case of Yano *et al* [180] the $\langle 110 \rangle$ wires have unreconstructed surfaces; and (iii) made use of Tersoff or Stillinger-Weber empirical potentials. A study of Si $\langle 001 \rangle$ nanowires using both DFT and Stillinger-Weber (SW) potentials found SW potentials underestimate the Youngs modulus at larger diameters, and overestimate at smaller ones, compared to DFT [196].

The objective of this chapter is to understand the effects of increasing shell and core size on the Young's modulus of $\langle 110 \rangle$ core-shell nanowire structures with surface reconstructions. Both the core and core-shell sizes were chosen such that they are representative of those found in pure elemental experimental structures. Simulation cells for our calculations have a minimum of 26 Å vacuum present[3] between periodic images to inhibit spurious interactions of periodic images. In Chapter 4 we report our stress implementation, and to further test our stress implementation we have used two methods to calculate the Young's modulus. The first method uses central finite differences[4] to estimate the force along the nanowire axis $F_{ax} = \delta E_{tot}/\delta L$, where $L$ is the axial length and $E_{tot}$ the total energy. Approx-

[3] Measured between the two nearest atoms.

[4] Calculated using the NumPy function `gradient` [204].

imate axial stress is calculated by $\sigma_{ax} = F_{ax}/A_{cs}$, where $A_{cs}$ is the cross-sectional area of length $L$. Strain along the NW axis is defined by $\frac{L-L_0}{L_0}$ where $L_0$ is the axial length of the optimal nanowire structure. The Young's modulus is then estimated by fitting a straight line[5] and finding the gradient using the Levenberg-Marquardt algorithm [205, 206] as implemented in SciPy [155, 207]. The second method directly plots calculated stress, scaled by $1/V_{NW}$ (nanowire volume), against strain and using the same fitting procedure to find the gradient (Young's modulus).

Stress-strain curves in Figure 7.3 were used to find the Young's modulus results presented in Table 7.1 via our second method outlined above. This method is preferred to deriving the axial force by finite differences ($1^{st}$ method) since it is less sensitive to fluctuations in the total energy and more accurate since it does not rely on derivatives produced by finite differences. For completeness we present stress-strain curves found by finite differences in Figure A.2. Whilst curves from finite differences yielded the same trend as those found directly from calculated stress, they consistently underestimated the Young's modulus as compared to our more accurate method.

Results in Table 7.1 show a monotonic decrease of the Young's modulus for Si (core) - Ge (shell) nanowires under increased shell deposition (4-X models). Nanowires of equivalent core and shell thickness, 4-4 and 6-6 models, show a slight decrease in stiffness as the diameter increases but this is within the expected error. We attribute these effects to differences in their composition, about a 1% increase in the Ge content with similar decrease in stiffness. Comparing models with the same shell thickness, 4-6 and 6-6, the increase in core size results in a stiffer nanowire in agreement with trends in the work of Deb Nath *et al* [194].

Our results suggest that the Young's modulus of Si (core) - Ge (shell) nanowires is very strongly correlated to the composition of the nanowire. In an attempt to decouple the observed behaviour of the Young's modulus in our nanowire models it is useful to draw comparisons to single element nanowires. Single element nanowires become stiffer with increasing diameter, tending to their bulk[6]

[5] Elastic region of nanowire stretching is assumed.

[6] DFT values calculated for this chapter can be found in the caption of table 7.3.

| | 4-4 | 4-6 | 4-8 | 6-6 |
|---|---|---|---|---|
| $N^{Si}$ atoms | 260 | 260 | 260 | 532 |
| $N^{Ge}$ atoms | 640 | 1104 | 1664 | 1392 |
| Frac. Ge comp. | 0.711 | 0.809 | 0.865 | 0.723 |
| Young's modulus (GPa) | 145.8 | 139.3 | 134.1 | 142.7 |
| Fitting error (GPa) | (0.9) | (1.0) | (1.8) | (2.2) |

**Table 7.1:** Young's modulus of Si (core) - Ge (shell) nanowires with error of fitting given in brackets. Error from fitting is the standard deviation in the gradient of the line of best fit in Figure 7.3.

values [20, 184]. The rate at which our Young's modulus values decrease with the thicker shell nanowires suggests the Young's modulus of core-shell nanowires is bounded by equivalent sized elemental nanowire counterparts, where Si the upper and Ge the lower limit. This implies that core-shell nanowires can be manufactured such that the Young's modulus may be tailored to the application, within the confines of bulk Si or Ge limits, regardless of the wire diameter by control of composition during manufacture.

### 7.3.4 Poisson's ratio of nanowires

The Poisson ratio is a measure of the deformation (expansion or contraction) in the directions perpendicular to the direction of loading, see Equation (7.5). It is a useful quantity for the calculation of the thermal conductivity in nanowires (related to the speed of sound in the medium) [208] and serves as a useful reference for finite element modelling to ascertain elastic constants [93]. No prior results have included the measurement of the Poisson ratio of core-shell nanowires. There are two main reasons for this: (i) approximations of an average wire radius lead to large changes in the calculated Poisson ratio [197]; and (ii) obtaining adequately converged structures is challenging.

$$\nu = -\frac{d\,\epsilon_{trans}}{d\,\epsilon_{axial}} \tag{7.5}$$

Since there are well defined surfaces present in our nanowire structures we calculated the Poisson ratio as the strain of the distance between opposing facets, i.e.

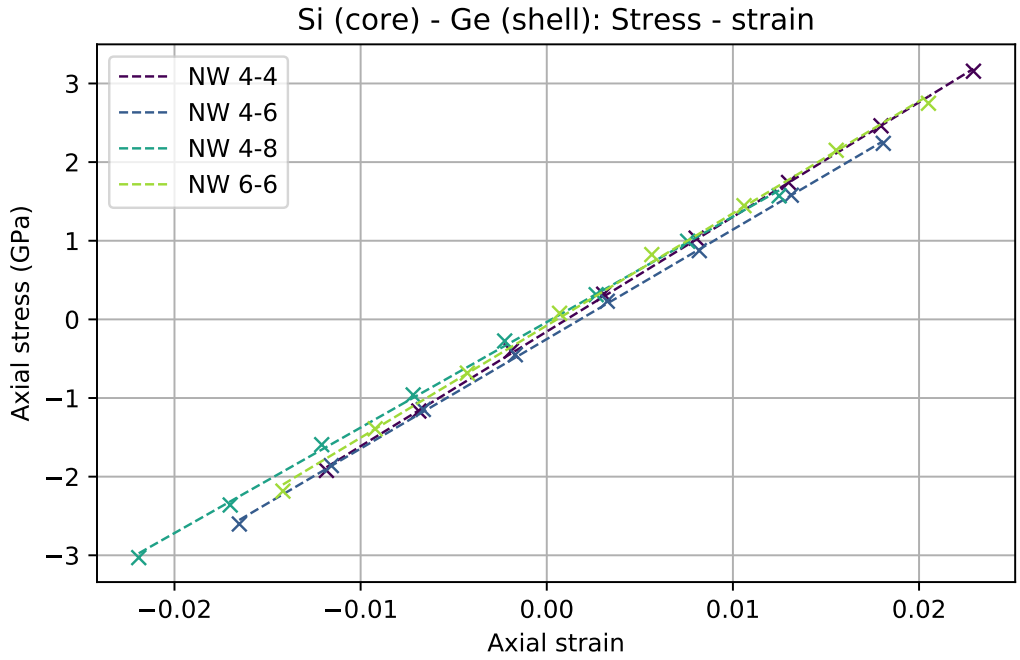


**Figure 7.3:** Plots of stress against strain, in the axial direction for Si (core) - Ge (shell) nanowires. Young's modulus is determined by the gradient of the line of best fit of the data, where stress values are those as implemented in CONQUEST divided by the volume of the nanowire found by our method in Section 7.3.1 for each strained nanowire in its respective 4-X/6-6 NW model.

⟨001⟩ or ⟨111⟩, described in Section 7.3.1. Results are presented in Table 7.2, where we find that the Poisson ratios in each direction are highly anisotropic and uniformly increase with an increasing shell thickness. The magnitude of Poisson ratios for 4-4 and 6-6 nanowire models are very close, within the error of fitting, while 4-X models indicate a strong positive correlation between increasing Ge composition and Poisson ratio. A similar study of pure Si ⟨110⟩ nanowires [197] found $\nu_{[110],[001]}$ and $\nu_{[110],[111]}$ to decrease with increasing nanowire diameter, with $\nu_{[110],[111]}$ decreasing at a lower rate. No significant influence of the nanowire diameter appears here, however, further work will be required to ascertain if nanowire diameter affects the Poisson ratio.

| | 4-4 | 4-6 | 4-8 | 6-6 |
|---|---|---|---|---|
| Avg. opt. dia. (nm) | 5.91 | 7.38 | 8.84 | 8.81 |
| Frac. Ge comp. | 0.711 | 0.809 | 0.865 | 0.723 |
| Cross-section | 0.190 | 0.290 | 0.400 | 0.183 |
| | (0.023) | (0.018) | (0.029) | (0.016) |
| ⟨001⟩ surface | 0.136 | 0.208 | 0.270 | 0.130 |
| | (0.016) | (0.014) | (0.016) | (0.012) |
| ⟨111⟩ surfaces | 0.075 | 0.118 | 0.168 | 0.073 |
| | (0.009) | (0.007) | (0.014) | (0.006) |

**Table 7.2:** Poisson ratios for Si (core) - Ge (shell) nanowires. We determine three different values for Si (core) - Ge (shell) nanowires: (i) the cross-sectional area; (ii) the ⟨001⟩ direction; and (iii) the ⟨111⟩ direction. These are gradients of the line of best fit shown in Figure 7.4 and the values in brackets are the standard deviations of the fitting. N.B. The first row in this table indicates the average diameters of the optimal nanowire structures.

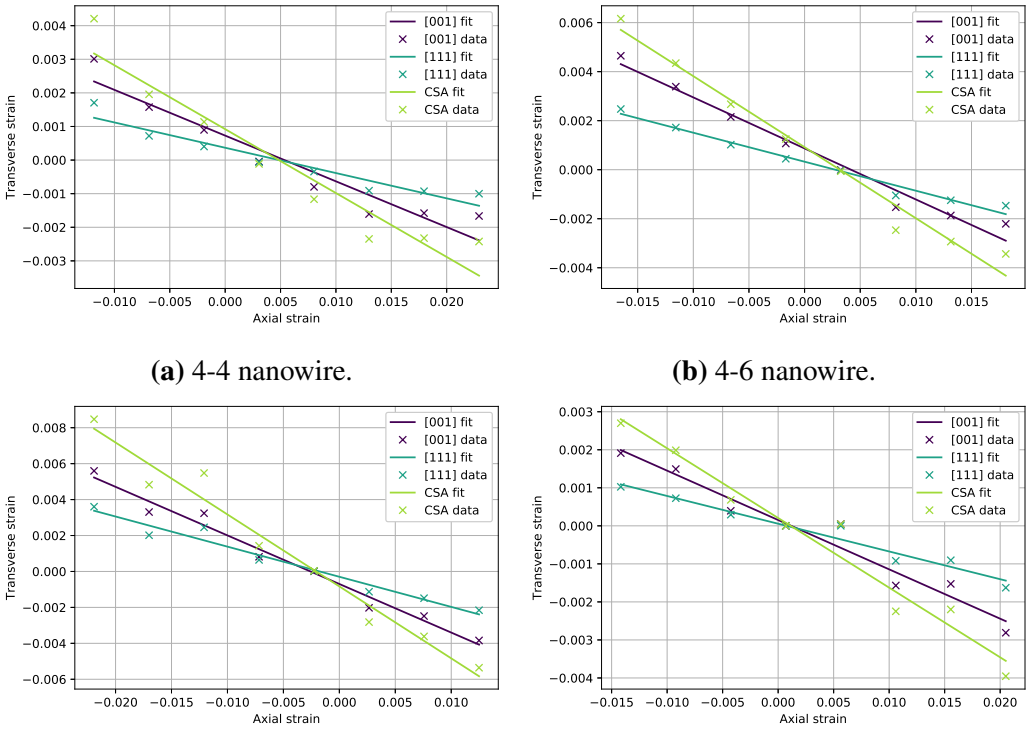


**(a)** 4-4 nanowire.

**(b)** 4-6 nanowire.

**(c)** 4-8 nanowire.

**(d)** 6-6 nanowire.

**Figure 7.4:** Axial strain against transverse strain for Si (core) - Ge (shell) nanowires. Transverse strains are found by computing the shortest distance between planes of the given direction, illustrated in Figure 7.1 and described in Section 7.3.1.

### 7.3.5 Comparison of Vegard's law with structures from diagonalisation

In Chapter 5 we showed there are discrepancies between total energy and derived properties, i.e. stress/pressure, between $O(N)$ methods and those found with Hamiltonian diagonalisation. These discrepancies are related to the reduced sampling of the full density matrix, i.e. a finite $L$-matrix range necessary for practical $O(N)$ DFT, and are additionally inversely proportional to the band gap of the material being simulated. The bulk modulus of the the materials presented in that chapter showed that materials with small band gaps would be poorly approximated by $O(N)$. Band gaps of our nanowire structures are not known *a priori* and we expect elastic properties to have significant effects on the final structures obtained, as in Chapter 6. In light of the approximations within $O(N)$ DFT it would be prudent to qualitatively assess any differences in the validity of Vegard's law using Hamiltonian diagonalisation with a multi-site support function basis and those results presented in Chapter 6, but with different sized wires.

Comparing results for 4-X nanowires in Table 7.3 with 3-X nanowires in Table 6.2 we find the $O(N)$ results showing an opposing trend, i.e. more disagreement with Vegard's law with an increasing shell thickness. There are several factors we need to consider when drawing a conclusion between these two results. First, increasing the Ge shell thickness will cause a reduction of the band-gap resulting in an overestimation of bondlengths due to the relatively small $L$-matrix range (see Chapter 5). Basis set size is another contributing factor. SZP basis sets were used in Chapter 6 and shown to be a good first approximation in Chapter 3. Although, systems studied in Chapter 3 were computed using the diagonalisation method, $O(N)$ results in Chapter 6 were tuned to reproduce the optimal bond lengths of Si and Ge respectively. As shown in Chapter 5, the elastic properties may be ill-described due to a finite $L$-matrix range, by proxy of bulk modulus results in that chapter, and would likely result in structures that are further away from the ground state found by Hamiltonian diagonalisation. Finally, the force criterion used in Chapter 6 will most likely have fallen short of those required for structural convergence, brought

| | 4-4 | 4-6 | 4-8 | 6-6 |
|---|---|---|---|---|
| $N^{Si}$ atoms | 260 | 260 | 260 | 532 |
| $N^{Ge}$ atoms | 640 | 1104 | 1664 | 1392 |
| Frac. Ge comp. | 0.711 | 0.809 | 0.865 | 0.723 |
| $a_0^{min}$ (Å) | 7.9876 | 8.0256 | 8.0700 | 8.0114 |
| $a_0^{lin}$ (Å) | 8.0221 | 8.0558 | 8.0748 | 8.0264 |
| Dev. (%) | -0.432 | -0.376 | -0.059 | -0.187 |

**Table 7.3:** Deviations from Vegards law for Si (core) - Ge (shell) nanowires, where optimal structures are found with diagonalisation using multi-site support functions. Bulk lattice parameters determined by Birch-Murnaghan equation of states fitting and input parameters as described in Section 7.2; $a_0^{Si} = 5.5002$ Å and $a_0^{Ge} = 5.7425$ Å. Our nanowires are oriented in the ⟨110⟩ direction, thus bulk lattice values are scaled by a factor of $\sqrt{2}$ to give the Vegard predicted NW axial lengths.

to our attention in Section 7.3.2.

For fixed core size, 4-X models, there is a gradual shift towards agreement with Vegard's law as the thickness of the shell increases, see Table 7.3. This is to be expected since Vegard's law is a simple linear interpolation of lattice parameters, so as the fractional composition of the nanowire tends to majority Ge, the effects of averaging work in favour of Vegard's law. Comparison of similar fractional compositions, 4-4 and 6-6 nanowires, exhibit a significant drop in the relative overestimation indicating a strong dependence on the effects of the interfacial and surface regions. Thus, the validity of Vegard's law in nanowires is highly dependent on the surface-to-volume ratio and is *not* a reliable model for use in nanowires. This is further evidenced by comparison of similar shell sizes, 4-6 and 6-6, where there is a similar drop in the relative overestimation of the axial length.

### 7.3.6 Strain mapping: Diagonalisation with MSSFs

We present the effective axial core and shell strains of Si (core) - Ge (shell) nanowires in Table 7.4 along with average strain values in Figure 7.5. These results show the axial core strain, for 4-X nanowires, increases as the shell becomes thicker. Figure 7.5(a) shows a similar increase in core strain for bonds along the ⟨001⟩ direction with increasing shell deposition (i.e. 4-X structures), about 0.2%

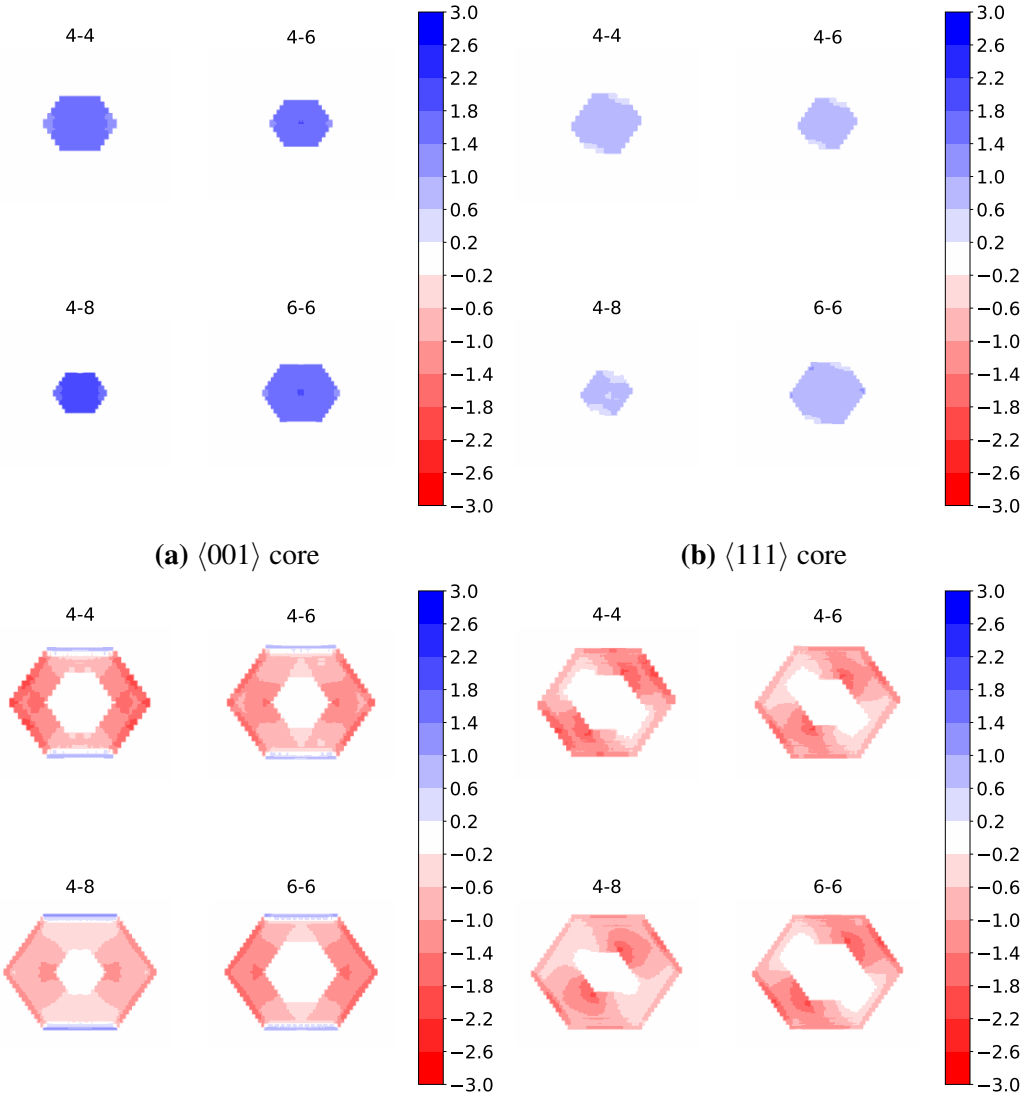


**(a)** ⟨001⟩ core **(b)** ⟨111⟩ core

**(c)** ⟨001⟩ shell **(d)** ⟨111⟩ shell

**Figure 7.5:** Strain mapping of Si (core) - Ge (shell) nanowires. Contours are drawn for increments of stress of 0.4%.

increase of the maximum strain. Figure 7.5(b) shows bonds along the ⟨111⟩ direction having a constant maximum strain in the core whilst there is a slight reduction in the 4-8 model. Conversely, the shell of 4-X models all exhibit a reduction in compressive strain along the axial, ⟨001⟩ (Figure 7.5(c)) and ⟨111⟩ (Figure 7.5(d)) bond directions. The magnitude of the ⟨111⟩ is largest but has a decreasing rate of change under shell deposition which we expect considering the ⟨111⟩ is the stiffest (see Table 7.4). However, the rate of change of ⟨001⟩ and axial directions increases under shell deposition. It appears ⟨111⟩ Ge bonds in the shell are competing with the stiffer ⟨111⟩ Si bonds in the core and strain relaxation in the shell is a function of more Ge being deposited.

The increase in the rate of change of axial and maximum ⟨001⟩ strains corresponds to these being the most elastically soft when considering the other bonding directions and elements. Our results indicate strain relaxation in 4-X models is primarily mediated by the bonds in the axial direction since these exhibit the greatest magnitude and rate of change in strain. These results are unexpected since the Young's modulus ordering is $\langle 111\rangle > \langle 110\rangle > \langle 001\rangle$ for both bulk Si and Ge [186]. So, the effects due to ⟨111⟩ interfaces and surfaces force strain relaxation along the nanowire axis and reduce the more elastically soft ⟨001⟩ oriented bonds ability to absorb strain.

Comparing 4-X model results Figures 7.5(a) and 7.5(b) to 3-X models in Figures 6.4 and 6.5, our results for the core agree in so much as they find tensile strain. However, 3-X models do not show a significant difference in the magnitude of the strain when considering either bond direction as they do in the results presented in Figure 7.5. Figures 6.2 and 7.5(c) agree reasonably well exhibiting similar trends in strain under shell deposition, except that $O(N)$ results show a slight tensile strain at the ⟨001⟩ Si-Ge interface which is not present in Figure 7.5(c). Bonds in the shell oriented along ⟨111⟩ (Figure 6.3) predict the existence of both tensile and compressive strain, in sharp contrast to those in Figure 7.5(d). $O(N)$ results for these ⟨111⟩ shell bonds do not even exhibit the same trend as those presented in this chapter. Discrepancies between results in Figure 7.5 and Figures 6.2 to 6.5 can be attributed

| | 4-4 | 4-6 | 4-8 | 6-6 |
|---|---|---|---|---|
| Relaxed axial length (Å) | 7.9876 | 8.0256 | 8.0700 | 8.0114 |
| Axial core strain (%) | 2.69 | 3.18 | 3.74 | 2.99 |
| Axial shell strain (%) | -1.64 | -1.18 | -0.62 | -1.35 |
| Avg. core $\langle 001 \rangle$ strain (%) | 1.54 | 1.70 | 1.91 | 1.70 |
| Avg. core $\langle 111 \rangle$ strain (%) | 0.79 | 0.75 | 0.61 | 0.82 |
| Avg. shell $\langle 001 \rangle$ strain (%) | -1.19 | -0.96 | -0.72 | -1.06 |
| Avg. shell $\langle 111 \rangle$ strain (%) | -0.98 | -0.82 | -0.82 | -0.90 |

**Table 7.4:** Axial strain and average radial strain values for core and shell regions of relaxed $\langle 110 \rangle$ Si (core) - Ge (shell) nanowires. Axial strain is computed as $\frac{a_0^{NW} - a_0^{Si/Ge}}{a_0^{Si/Ge}} \times 100$, where $a_0^{NW}$ is the relax nanowire axial length and $a_0^{Si/Ge}$ are the reference bulk values of $\langle 110 \rangle$ oriented Si or Ge. These reference values were found by DFT using the same calculation parameters as those in Section 7.2 which yields $a_0^{Si} = 7.7785$ Å and $a_0^{Ge} = 8.1211$ Å.

to 3 factors. First, $O(N)$ performs poorly for small band-gap materials with finite $L$-matrix ranges (Chapter 5). Second, 0.02 eV/Å is not a tight enough force tolerance to achieve structural convergence, as shown in Section 7.3.2. Finally, a small SZP basis lacks the variational freedom afforded by a larger basis set, the subject of Chapter 3, but for now this is the largest size possible with $O(N)$.

## 7.4 Conclusion

The mechanical properties of Si (core) - Ge (shell) nanowires are of significant interest to device manufacture, for example, tuning the band gap through applied strain and how the intrinsic strain may affect dopant location. Computational literature of similar nanowires, without surface reconstructions, have methodological flaws such as how the volume is calculated and inappropriate force tolerances for structural optimisation [184]. We presented our methodology for the determination of nanowire volume such that there is no ambiguity in its definition and will consistently produce reliable volume derived properties such as Poisson's ratio and the Young's modulus. Furthermore, we have found that the minimum force tolerances quoted in the literature (0.02 eV/Å) were not sufficient in determining the ground-state structures of our nanowires, suggesting other computational works may not

necessarily be well represented in experimental studies and require revision in the near future.

We have determined the Young's modulus and Poisson ratio of surface reconstructed, experimentally complementary nanowires with great accuracy and clearly defined methods. Young's modulus data has shown us that increasing the Ge shell thickness of our structures results in a reduction of nanowire stiffness, bounded by the Young's modulus of similarly sized Si (upper) and Ge (lower) elemental nanowires. Therefore, it is possible to tailor nanowire stiffness with regardless of diameter contrary to simple elemental nanowires. Poisson ratio data shows that increasing shell thickness results in an increase in the Poisson ratio whilst nanowires of similar composition, but different diameters, will have similar ratios. The Poisson ratio is anisotropic depending on the surfaces considered with $\langle 111 \rangle$ surfaces having a smaller ratio than $\langle 001 \rangle$ surfaces.

Large-scale simulations with DFT embody huge theoretical progress of the field of materials simulation, although they are not without issue. Revisiting the subject of our previous chapter and paper [176], on the suitability of Vegard's law and strain mapping, we have found that approximations within $O(N)$ result in some disagreement between previous results and those presented in this chapter. Results in Section 6.2 suggest Vegard's law becomes less appropriate as Ge shell thickness increases, opposing those results found in Section 7.3.5, with the disagreement easily explained by the reduction in band gap due to increased Ge content.

Quantitatively, core strain maps produced in both $O(N)$ and diagonalisation methods are similar. However, nanowire shells found through $O(N)$ exhibit both tensile and compressive strain whilst diagonalisation shows compression only. Unlike results pertaining to Vegard's law, this may not be so easily explained by band-gap reduction being the cause of this discrepancy since it is present in all $O(N)$ structures. These issues may be explained by incomplete relaxation due to a larger force tolerance or due to the effect of fitting basis sets to reproduce bulk bond lengths which may negatively affect the description of elastic properties.

Moving forward, the simplest possible extension to this chapter is to provide

data on the reverse core-shell composition and is currently being undertaken. However, two further simple considerations may be done: (i) a fuller description of similar nanowire core-shell widths (i.e. 5-5, 7-7 etc) would more fully describe the Young's modulus variation as core-shell nanowires become large; and (ii) models whose shell thickness is smaller than the core. Core-shell nanowire structures are time consuming to reach convergence, part of this issue is due to volume oscillations related to the "long-wavelength" relaxations. Due to the interfaces and surfaces present in our structures these regions will tend to have large forces on the atoms, whilst those furthest away from these regions will tend to have small/zero for on them. Traditional energy minimisation algorithms, such as conjugate gradients, will move the atoms near the surfaces/interfaces first, which will initiate a wave of displacement, travelling iteration to iteration only to be reflected at the next surface/interface, and slowly decaying to zero [209]. This issue could be reduced with the introduction of a hybrid structure solver similar to that to Goedecker *et al* [210] where the optimisation problem is transformed from an atomistic model to elastic theory.

# Chapter 8

# Electronic structure of NWs

## 8.1 Introduction

Heterojunctions are crucial to the modern world and prevalent in many devices such as: lasers; photovoltaics; and transistors. Bandstructure engineering is central to the advancement of heterojunctions leading to the formation of electron gases in GaAs/AlGaAs [211] and hole gases in Ge/SiGe [212] *planar* systems. Core-shell nanowire heterojunctions offer a greater potential for the strain engineering as strain may be modulated varying the core and shell thickness, as demonstrated in Chapter 7.

Compared to elemental nanowires, core  shell structures have some major advantages, such as: better conductance [213]; and higher mobility of charge carriers due to band offsets (illustrated in fig. 1.1(a)) which reduce carrier scattering due to charged dopant atoms in doped NWs [183]. Previous calculations of electronic structure have, in general, been performed on core-shell nanowires which are far smaller than those experimentally observed [34–36, 158, 214, 215]. Whilst the electronic structure effects due to surface reconstructions have been studied in Si nanowires [216–218], similar studies for core-shell nanowires have yet to be characterised.

In lieu of the calculations comparable to experiment, studies of strained core-shell nanowires represent a first approximation to the control of strain due to deposition, to which results presented in this chapter will be compared. In this chapter

we shall find the bandstructures of the relaxed nanowires determined in the previous chapter (section 8.3.1) and effective carrier masses calculated. Determination of band offsets are presented in section 8.3.2 via calculation of band densities cross-referenced with the bandstructure plots. Finally, we investigate how local strain environments affect the electronic structure at an atomic level via projected densities of states in section 8.3.3.

## 8.2 Computational details

Performing highly accurate electronic structure calculations on very large structures is extremely difficult owing to the size of the matrices needing to be diagonalised. One method to circumvent this issue is to reduce the size of the matrices used for the calculation of such properties. The method we use for doing so is using multi-site support functions (MSSFs), the theoretical background for this can be found in Section 2.8.2. Nakata *et al* have demonstrated that for a large enough MSSF and local filter diagonalisation (LFD) range, the DOS and bandstructures close to the Fermi level are quite close to the primitive basis set size [84, 87]. These works show how the electronic properties for occupied states and unoccupied states near the Fermi level are reasonably reproduced, however, it is instructive to quantify the approximation of this method. To do so we compare the total DOS and bandstructures of our smallest nanowire using a primitive basis set and one made from multi-site support functions, see fig. 8.2. Our results for 12 Bohr MSSF and LFD ranges show excellent agreement with the reference *primitive* basis set results for the valence band and conduction band up to about 2 eV. Results beyond 2 eV are not presented in this thesis due to the lack of trustworthiness of unoccupied states calculated using MSSFs, as reported in other CONQUEST publications [84, 87]. The poor description of unoccupied states are attributed to the minimal basis size of the current MSSF implementation in CONQUEST (4 support functions for Si/Ge and 1 for H) and the optimisation process which only considers for the occupied states [219].

Within this chapter all calculations were done with an integration grid cut-off of 100 Ha and the GGA functional parameterised by Perdew, Burke and Ernzer-

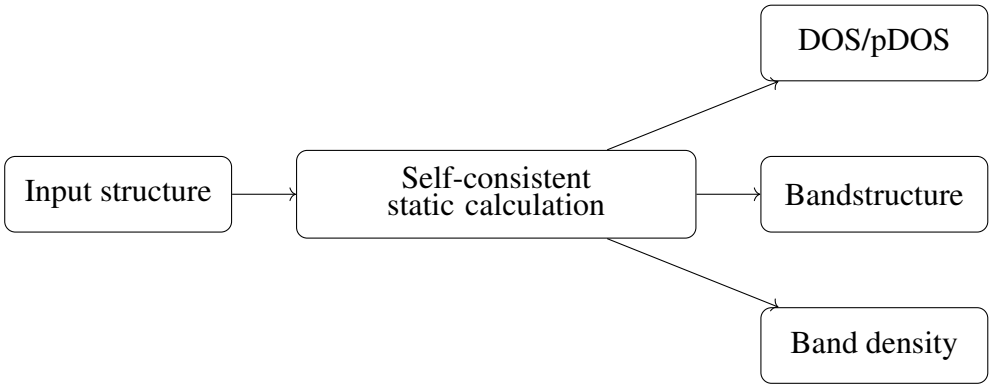


**Figure 8.1:** Flow diagram for the production of results within this chapter. In all calculation steps the same basis sets and integration grid cutoffs were used.

hof (PBE), with the explicit treatment of H ($1s^1$), Ge ($4s^2 4p^2$) and Si ($3s^2 3p^2$) electrons. A basis set size of triple-$\zeta$, triple-polarisation was used since these are the most accurate basis sets due to the many degrees of freedom offered during optimisation [45]. Converged charge densities with respect to Brillouin zone sampling (see fig. 8.1) are required for production of density of states (DoS), atomically-projected density of states, bandstructures and band densities. Production of the well converged charge densities used CONQUEST v0.51-455 with a $\Gamma$-centred $1\times7\times1$ Monkhorst-Pack k-point mesh[1], with input structures being the axially optimised final structures found in Chapter 7. DoS and atom projected DoS used an energy sampling bin width of approximately 0.07 mHa and a smearing factor of 0.2 mHa; and were calculated using the new CONQUEST post-processing code. Band structures were calculated using a 31 $k$-point sampling line from $\Gamma \rightarrow X$ to enable the most accurate estimation of effective carrier masses. Finally, band densities were also produced using the new CONQUEST post-processing tool, with band densities written for each of the $k$-points used to determine the converged charge densities.

[1] An increased k-point sampling is used for the production of the electronic structure as compared to Chapter 7. This is because the *total energy* is an integral over all bands and k-points, which are converged before structural relaxation begins. So, the fine detail of the Brillouin zone and resulting charge density are relatively unimportant for structural relaxation, however, the electronic properties such as the shapes of bands and DoS are more sensitive to these fine details. Therefore, we have chosen to increase the k-point sampling used to produce the input charge density for electronic structure results presented in this chapter.

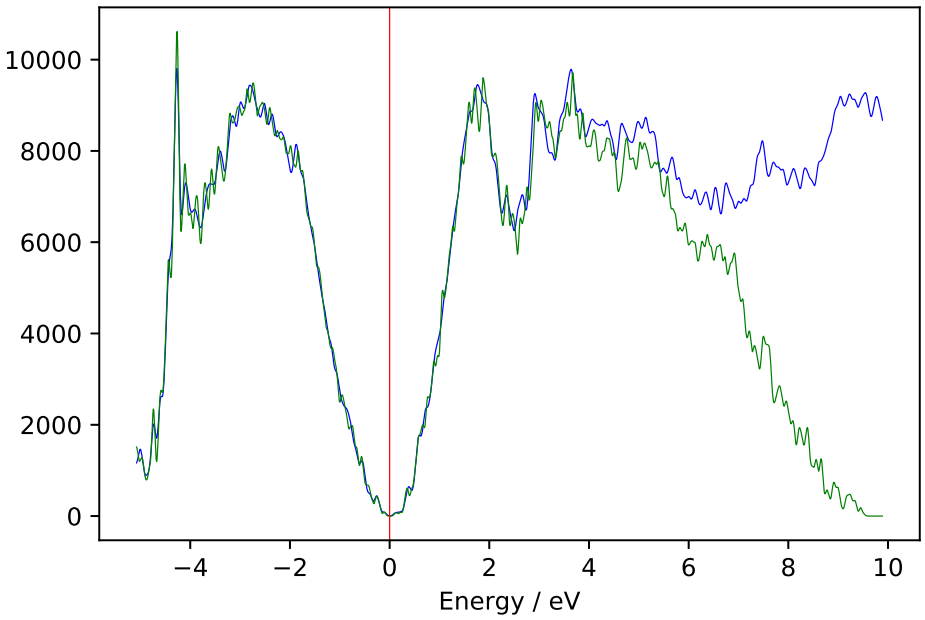


**Figure 8.2:** Comparison of the total DOS for primitive basis set in blue and MSSF in green. 12 Bohr MSSF and LFD ranges used.

## 8.3 Results

### 8.3.1 Bandstructures

Band gaps presented in table 8.1 decrease monotonically in 4-X models with increasing shell deposition, an expected result given that the band gap of Ge is much smaller than Si and widely reported to be a function of composition [34]. Figure 8.3 illustrates that band gaps of the 4-4, 4-6 and 6-6 nanowires are all clearly direct gap semiconductors, however, we note that the valence band maximum of the 4-8 nanowire looks extremely flat in comparison to the other structures. Whilst not easily discerned by inspection, the valence band maximum of our 4-8 structure is not situated at the Γ-point upon vigorous examination of the data. Measurement of the difference in $k$-space between the valence band maximum (VBM) and Γ-point results in a phonon wavevector of magnitude $k \approx 0.0103 a_0^{-1}$ ($1.95 \times 10^6 cm^{-1}$) required to conserve momentum for excitation of an electron to the conduction band minimum (CBM).

Indirect band gaps have previously been observed in theoretical studies of

$\langle 110 \rangle$ Si (core) - Ge (shell) nanowires, but only under the influence of significant *applied* uniaxial strain for small (2.5-4.7 nm) nanowires [182, 183]. More recent calculations of elemental Ge [220] and Si [185] $\langle 110 \rangle$ nanowires (8 nm in diameter) have revealed that under an *applied* uniaxial tensile strain the valence band edges flatten, eventually becoming indirect gap materials. In all of the aforementioned works none have considered the *intrinsic* strain present in nanowires.

Radial strain environments were thoroughly mapped in fig. 7.5 and axial strains in table 7.4; which indicate Ge is always under compressive strain whilst Si is always under tensile strain. It should be noted that the strains present in our nanowires are *intrinsic* and fundamental to these minimum energy structures. To enable comparison between our work and that of Niquet *et al* [185, 220] we must find the uniaxial strain using the definition in Niquet *et al*[2];

$$\epsilon_{uni} = \epsilon_{\parallel} - \epsilon_{\perp} \tag{8.1}$$

where $\epsilon_{\parallel}$ is the strain parallel to the nanowire axis and $\epsilon_{\perp}$ perpendicular. If we consider $\epsilon_{uni}$ may be well represented by the average strain, then it is possible to determine $\epsilon_{\perp}$ from the data in fig. 7.5 and presented in table 8.1. Only bonds in the $\langle 001 \rangle$ and $\langle 111 \rangle$ directions have components perpendicular to the axial direction, and for any Si or Ge atom two bonds are $\langle 111 \rangle$ oriented and one is $\langle 001 \rangle$ (see core inset of fig. 6.1). Thus, $\bar{\epsilon}_{\perp}$ is found by;

$$\bar{\epsilon}_{\perp} = \frac{\bar{\epsilon}_{\langle 001 \rangle} + 2 \times \bar{\epsilon}_{\langle 111 \rangle}}{3} \tag{8.2}$$

where $\bar{\epsilon}_{\langle 001 \rangle}$ is the average strain in the $\langle 001 \rangle$ direction and $\bar{\epsilon}_{\langle 111 \rangle}$ the average in the $\langle 111 \rangle$ direction; determined from the source data in our strain maps (fig. 7.5). Using values for the strain in the axial direction (see table 7.4) we are able to determine $\bar{\epsilon}_{uni}$ for the core and shell regions. An atomic weighted average of $\bar{\epsilon}_{uni}^{core}$ and $\bar{\epsilon}_{uni}^{shell}$, according to nanowire composition values in table 7.3, yields the average total uniaxial strain on the nanowire.

[2]Further details of the uniaxial strain definition can be found in the Supplementary Information of Ref. [185].

Correlating the total uniaxial strains presented in table 8.1 with the bandstructures in fig. 8.3, it is clear that *intrinsic* tensile (positive) uniaxial strain does result in a similar flattening of the valence band maxima (VBM), and in the case of our 4-8 NW, a direct to indirect gap transition. This complements the results of Niquet *et al*. Furthermore, looking at contributions to the total uniaxial strain from core and shell regions (in table 8.1), these electronic structure changes are driven by the deposition of thicker Ge shells. The effect is two-fold: (i) thicker Ge shells exert increasing uniaxial strain on the Si core; and (ii) uniaxial shell strain transitions from negative to positive. Recall that Niquet *et al* found *applied* tensile (positive) uniaxial strain flattens valence band edges, eventually resulting in a direct to indirect gap transition for elemental nanowires of 8 nm diameter. A third, more subtle point, is the change in the quantum confinement that usually results in the direct band gap of $\langle 110 \rangle$ nanowires. However, qualitative description of the change in the confinement potential requires the calculation of the exciton Bohr radius, and would require methods beyond DFT to calculate accurately, far beyond the scope of this thesis.

Effective carrier masses were obtained by fitting of a second-order polynomial to the band maxima, and further $k$-points either side, using the Levenberg-Marquardt [205, 206] implementation of the `curve_fit` function of SciPy [155, 207] and computing $m^* = \left(\frac{\partial^2 E}{\partial k^2}\right)^{-1}$. Effective electron masses change very little across our nanowire samples, but the differences represent a negative correlation with the average uniaxial core strain. Comparing $m_e^*$ of 6-6 to the 4-4 model we note the discrepancy and attribute it to size effects of the nanowire since their compositions are similar and $m_e^*$ for 6-6 is still slightly heavier than that of the 4-4 nanowire. Hole masses correlate well with the total intrinsic strain, primarily because the total intrinsic strain mixes in the compositional effect, although the nature of the valence band in the 4-8 is not directly comparable since the nature of the band is fundamentally different to those near the $\Gamma$-point.

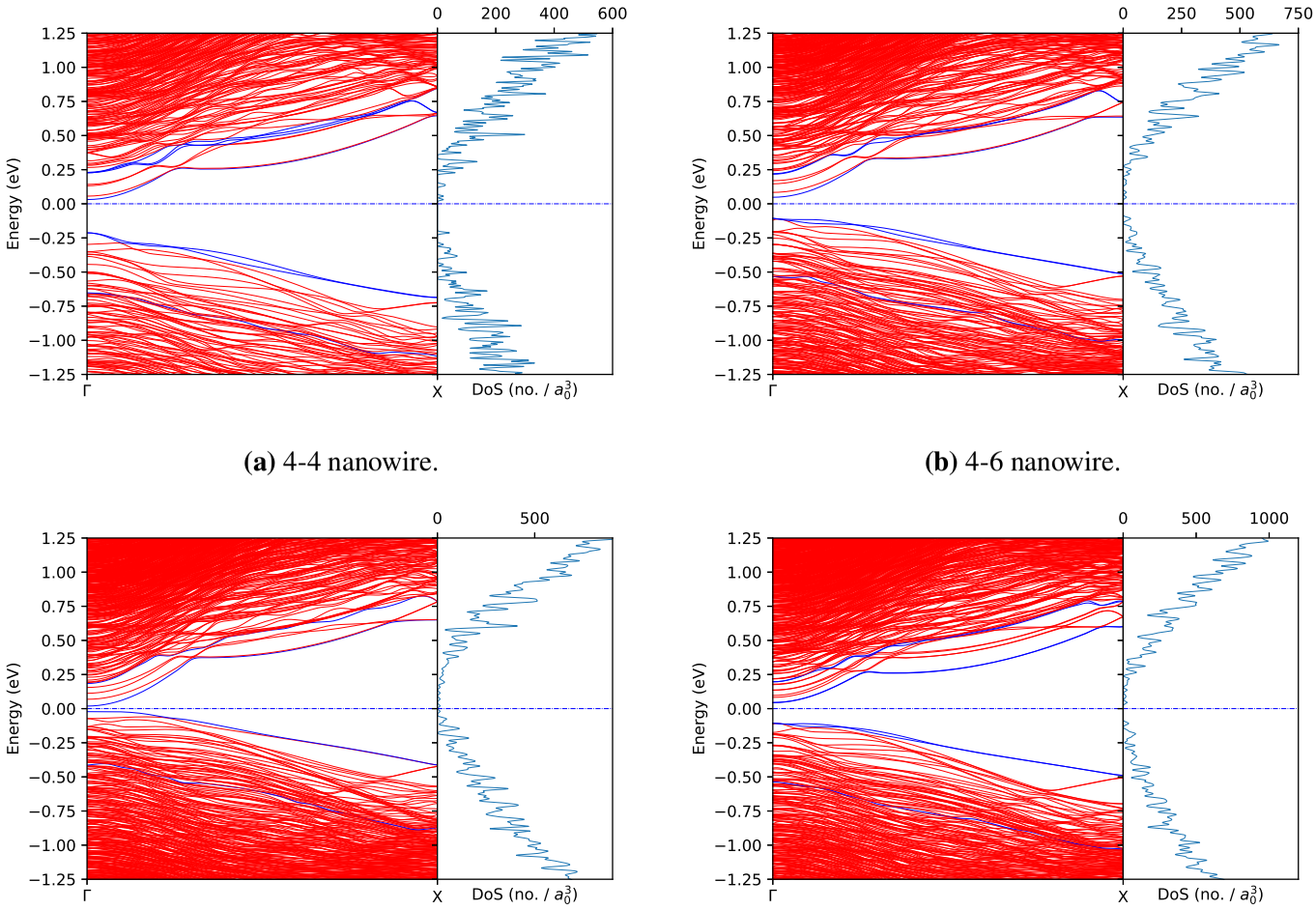


**(a)** 4-4 nanowire.

**(b)** 4-6 nanowire.

**(c)** 4-8 nanowire.

**(d)** 6-6 nanowire.

**Figure 8.3:** Band structure and total density of states for: (a) 4-4; (b) 4-6; (c) 4-8; and (d) 6-6 Si (core) - Ge (shell) nanowires. Horizontal dashed blue line at 0.0 eV represents the Fermi energy. Bands in blue correspond to bands localised within either the core or shell of our nanowires, the densities which will be presented and discussed in section 8.3.2.

| | 4-4 | 4-6 | 4-8 | 6-6 |
|---|---|---|---|---|
| Band gap (eV) | 0.244 | 0.154 | 0.041 | 0.150 |
| $m_h^*$ | -0.086 | -0.095 | -0.674 | -0.100 |
| $m_e^*$ | 0.140 | 0.132 | 0.131 | 0.141 |
| $\bar{\epsilon}_{uni}^{core}$ | 1.65 | 2.11 | 2.70 | 1.88 |
| $\bar{\epsilon}_{uni}^{shell}$ | -0.588 | -0.313 | 0.169 | -0.395 |
| $\bar{\epsilon}_{uni}^{total}$ | 0.0578 | 0.149 | 0.511 | 0.233 |

**Table 8.1:** Uniaxial strains: Effects on the band gaps, effective hole mass ($m_h^*$) and effective electron mass ($m_e^*$). Average uniaxial strain in the core ($\bar{\epsilon}_{uni}^{core}$), shell ($\bar{\epsilon}_{uni}^{shell}$) and atomic weighted average ($\bar{\epsilon}_{uni}^{total}$) for Si (core) - Ge (shell) nanowires.

### 8.3.2 Band densities and offsets

A fundamental property of radially heterostructured nanowires are the existence of band offsets (see fig. 1.1(a)), resulting in the formation of potential wells in conduction and valence bands under shifting of the Fermi level. Undoped systems have shown the existence of hole gas formation in the valence band [30, 221, 222], although this zero bias hole gas arises due to source/drain electrodes making contact with the wire [222]. Confinement of carriers to either the core or shell is a highly desirable property when doping nanowires, enhancing carrier concentration, since it is possible to choose doping location (core or shell) at growth time and judicious dopant choice will enable carriers to become separated from charged dopant atoms, i.e. modulation doping. Typically Si is chosen to be *p*-type doped (fig. 1.1(c)) and Ge *n*-type doped (fig. 1.1(b)) in order to take advantage of the carrier separation from charged dopant atoms [28, 223–225].

Characterisation of the band offset is important to experimental work since calculations are often used as an estimate for analyses [37]. It is often assumed to be 500 meV in [30, 213, 221], however, the work attributed to this figure used LDA DFT to simulate an idealised *bulk* interface [226] and may be considered not entirely relevant to nanowires considering: (i) the reduced dimensions of nanowires; and (ii) the progress in DFT calculations since 1986! For example, Yang *et al* found both the valence ($E_{VBO}$) and conduction ($E_{CBO}$) band offsets to be $\sim 0.2$ eV [37] for $\langle 110 \rangle$ Si (core) - Ge (shell) nanowires with $d = 4.1$ nm. Huang & Yang studied similar

nanowires with $d = 2.5$ nm [227], finding: (i) $E_{VBO} \approx 0.8$ eV and $E_{CBO} \approx 0.3$ eV; and (ii) $E_{VBO} \approx 0.3$ eV and $E_{CBO} \approx 1.0$ eV[3].

Band offsets presented in this chapter were found by calculation of the band densities at the Γ-point and plotting these densities in real-space with VESTA [228] to ascertain charge localisation in either the core or shell regions. Images of the band density isosurfaces and cross-sections used can be found in: fig. 8.4 for core-localised valence; fig. 8.5 shell-localised valence; fig. 8.6 core-localised conduction; and fig. 8.7 shell-localised conduction bands respectively. After finding the appropriate bands by inspection, energies can be read off the bandstructure plots in fig. 8.3 (blue bands) to ascertain the offsets presented in table 8.2.

Conduction band offsets for 4-X nanowires monotonically decrease with increasing shell deposition, although the rate of change does slow. A sudden decrease in $E_{CBO}$ of the 6-6 nanowire, as compared to the 4-8, is indicative of a non-trivial effect, since: (i) 4-4 and 6-6 nanowires have similar composition (see table 7.3); (ii) 4-6 and 6-6 have identical shell size; and (iii) 4-8 and 6-6 are of similar total diameter. The similarity between 4-6 and 4-8 nanowire $E_{CBO}$ is our first clue to understanding this change since they have vastly different compositions, total diameter and strain environments. Only the core and shell sizes remain to offer an explanation. We can see in fig. 8.6 that all 4-X nanowires have a significantly higher charge density in the core as compared to the 6-6 with the only difference being core size. Furthermore, fig. 8.7(a) demonstrates charge in the shell *and* core, whilst figs. 8.7(b) to 8.7(d) are all strongly localised in the shell. These two observations imply absolute sizes of the core and shell regions, respectively, play an important role in determining the conduction band offset. The increasing shell size results in a shift of the shell-localised conduction band edge toward the Fermi level, whilst an increase in core size a shift away from the Fermi level (see table 8.2).

In contrast to conduction band offsets, valence band offsets do not appear to be as strongly influenced by changes in the sizes of the core and shell. Examination of the core localised valence band edges in table 8.2 demonstrate 4-X model band

[3]It should be noted that structure (i) is similar in composition to our 4-4 structure whilst their structure (ii) probes a very thin shelled structure.

| | 4-4 | 4-6 | 4-8 | 6-6 |
|---|---|---|---|---|
| Core localised VBM (eV) | -0.652 | -0.534 | -0.405 | -0.537 |
| Shell localised VBM (eV) | -0.213 | -0.106 | -0.0220 | -0.106 |
| Valence band offset (eV) | 0.439 | 0.428 | 0.383 | 0.430 |
| Core localised CBM (eV) | 0.0310 | 0.0479 | 0.0188 | 0.0454 |
| Shell localised CBM (eV) | 0.227 | 0.216 | 0.184 | 0.196 |
| Conduction band offset (eV) | 0.196 | 0.169 | 0.166 | 0.151 |

**Table 8.2:** Band edges and offsets for core/shell localised valence/conduction band states. Localisation for identifying offsets in core/shell regions found using band densities in figs. 8.4 to 8.7, with energies taken from fig. 8.3 and method illustrated in fig. 1.1(a). Values presented to 3 significant figures but calculated from data precision.

edges shift toward the Fermi level as shell size increases, and considering the band edge energy of the 6-6 model is very close to that of the 4-6 model, follows $\bar{\epsilon}^{core}_{uni}$ trends in table 8.1 very well. Shell localised valence band edges across all nanowire models follow the same reasoning and correlations as the core localised band edges, showing almost no dependence on size and near perfect correlation with $\bar{\epsilon}^{shell}_{uni}$. One small indication of size dependence in $E^{shell}_{VBE}$ are 4-6 and 6-6 model edge energies and shell strains, where the 6-6 has a slightly larger compressive but identical edge energies (to 3 significant figures), although the effect is so small it may be considered negligible.

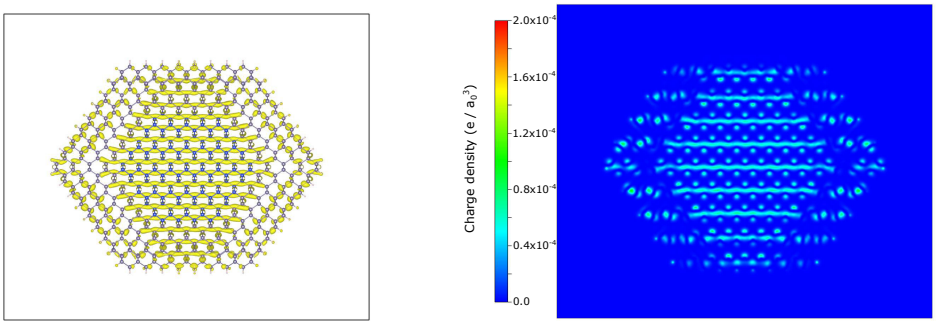


**(a)** 4-4 nanowire

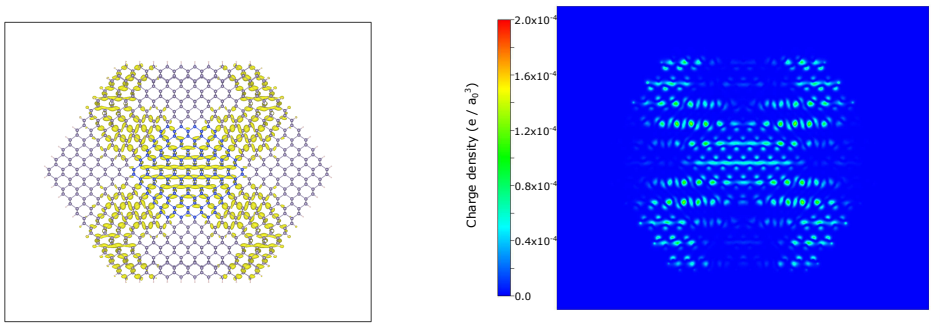


**(b)** 4-6 nanowire

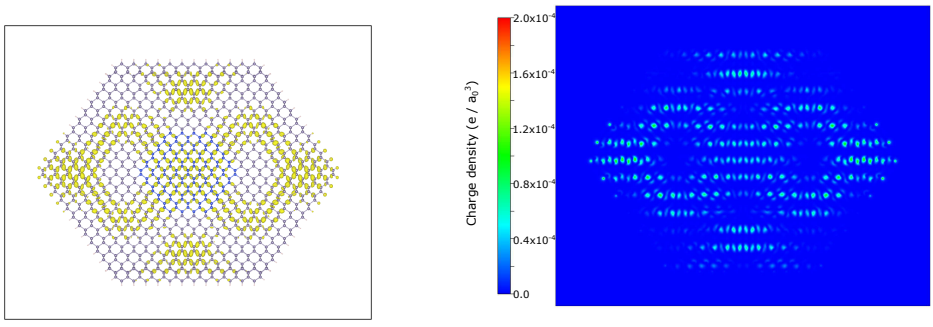


**(c)** 4-8 nanowire

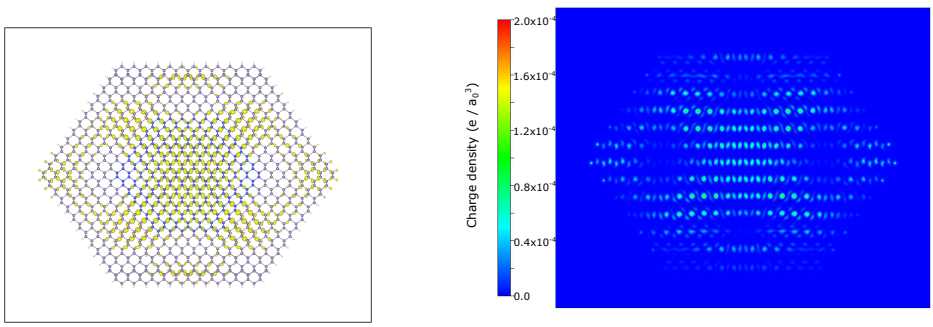


**(d)** 6-6 nanowire

**Figure 8.4:** Valence band densities exhibiting significant charge density in the core region of Si (core) - Ge (shell) nanowires. Left images represent the charge isosurface in relation to the structure, whilst right images represent a planar section through the isosurface. All isosurfaces in this figure were prepared using the same isosurface value of $2 \times 10^{-5}(e/a_0^3)$.

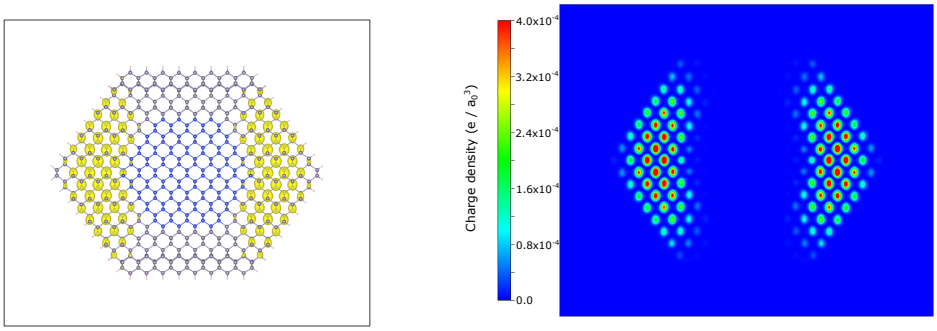


**(a)** 4-4 nanowire

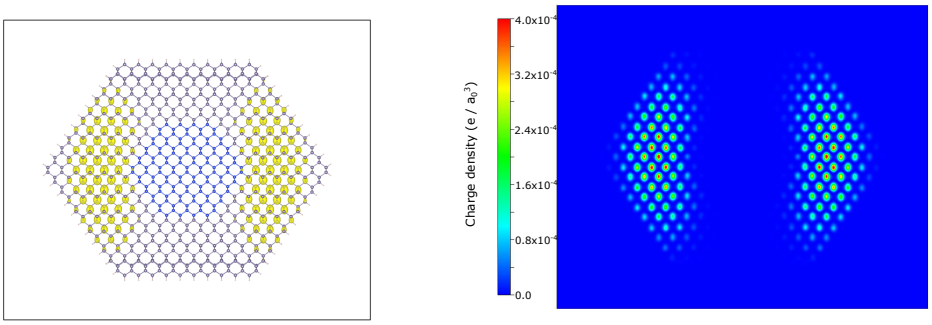


**(b)** 4-6 nanowire

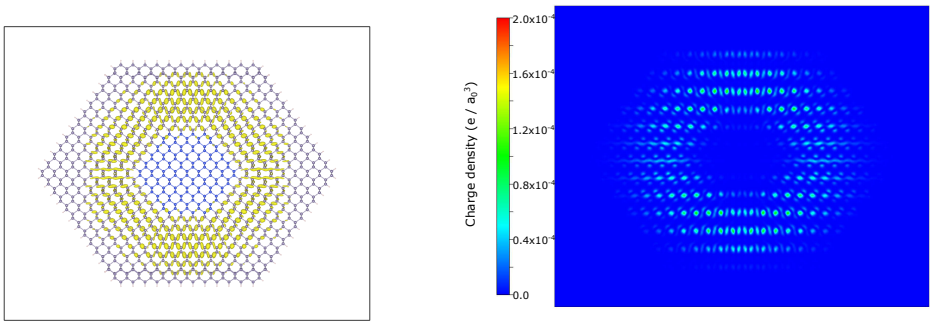


**(c)** 4-8 nanowire

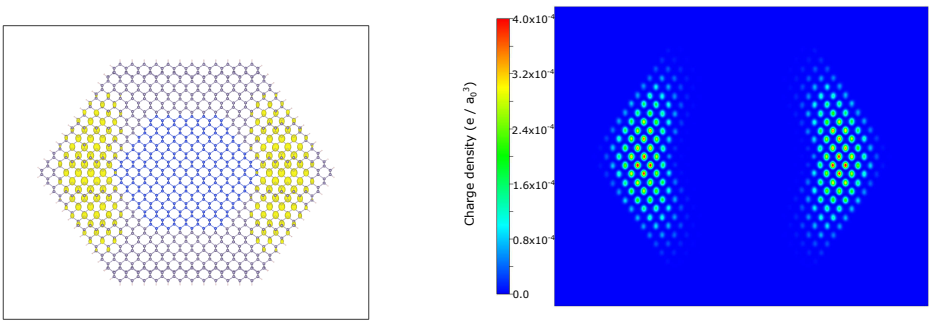


**(d)** 6-6 nanowire

**Figure 8.5:** Valence band densities exhibiting strong shell charge localisation in Si (core) - Ge (shell) nanowires. Left images represent the charge isosurface in relation to the structure, whilst right images represent a planar section through the isosurface. Figures (a), (b) and (d) all represent doubly degenerate bands, so an isosurface value of $4 \times 10^{-5}(e/a_0^3)$ was used for these, twice that of the non-degenerate band in (c).

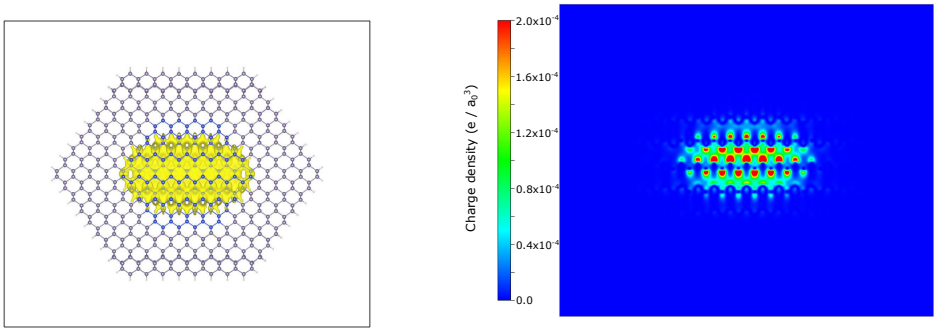


**(a)** 4-4 nanowire

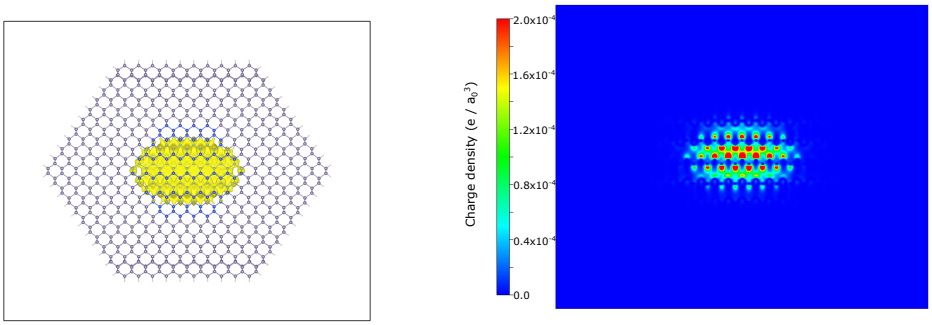


**(b)** 4-6 nanowire

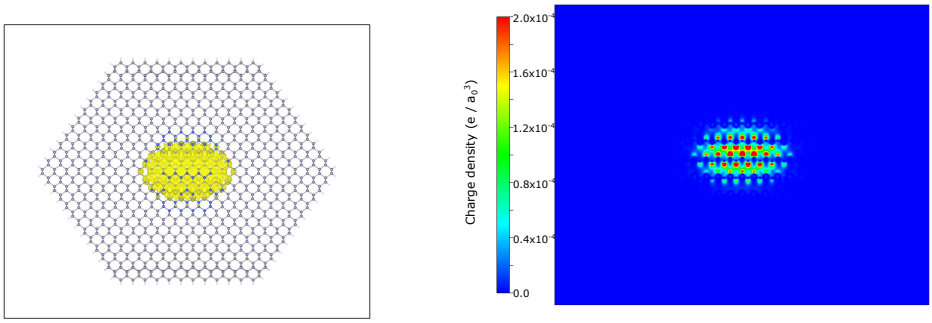


**(c)** 4-8 nanowire

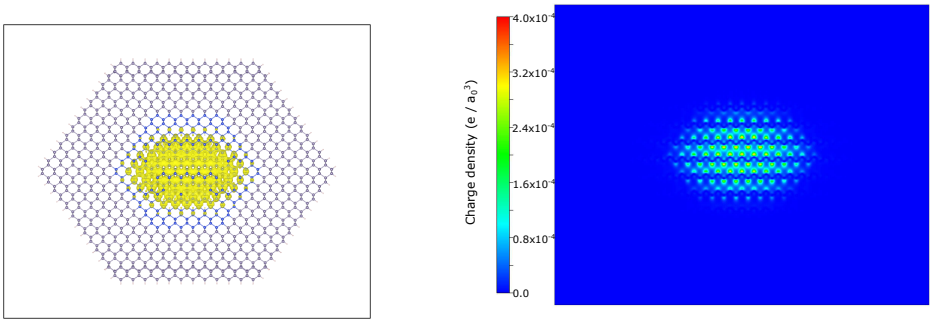


**(d)** 6-6 nanowire

**Figure 8.6:** Conduction band densities confined within the core region of Si (core) - Ge (shell) nanowires. Left images represent the charge isosurface in relation to the structure, whilst right images represent a planar section through the isosurface. Bands in figs. (a), (b) and (c) use an isosurface value of $2 \times 10^{-5}(e/a_0^3)$, whilst fig. (d) is doubly degenerate and uses an isosurface value of $4 \times 10^{-5}(e/a_0^3)$.

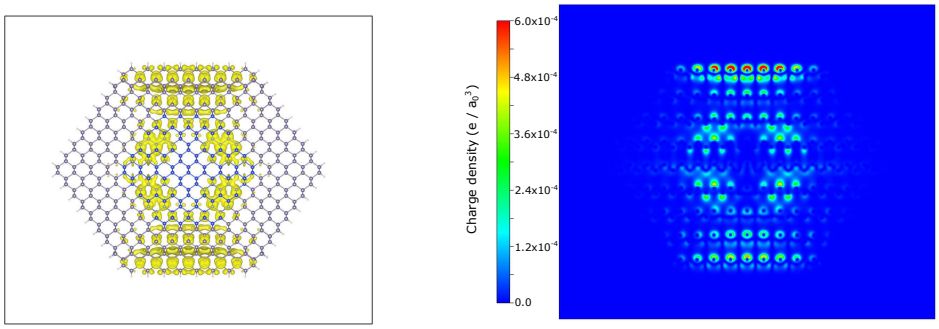


**(a)** 4-4 nanowire

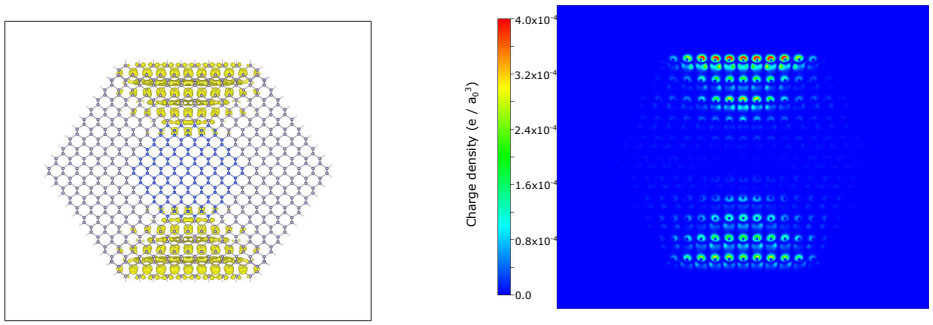


**(b)** 4-6 nanowire

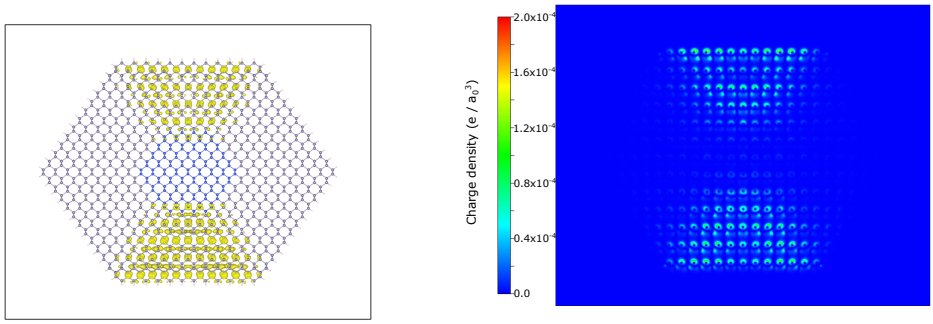


**(c)** 4-8 nanowire

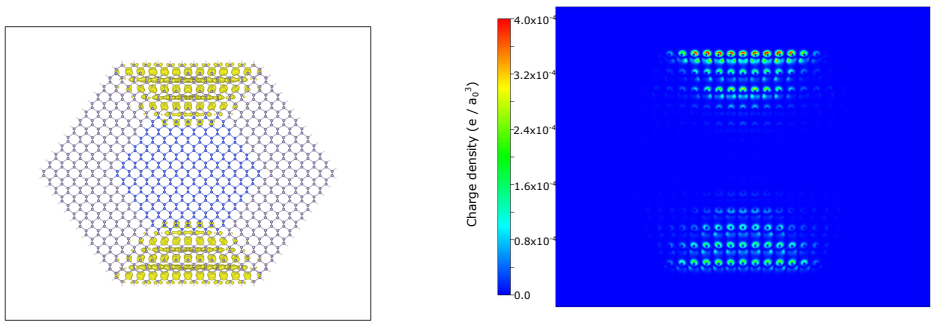


**(d)** 6-6 nanowire

**Figure 8.7:** Conduction band structures with significant charge localisation in the shell region of Si (core) - Ge (shell) nanowires. Left images represent the charge isosurface in relation to the structure, whilst right images represent a planar section through the isosurface. Figure (a) is triply degenerate and uses an isosurface value of $6 \times 10^{-5}(e/a_0^3)$, whilst figs. (b) and (d) are doubly degenerate and use an isosurface value of $4 \times 10^{-5}(e/a_0^3)$. Figure (c) is non-degenerate and thus uses a value of $2 \times 10^{-5}(e/a_0^3)$.

### 8.3.3 Atom projected density of states

In fig. 7.5 we presented a map of the local strain environments in our nanowire models, isolating the bond direction and core/shell contributions. To further our understanding of the local strain effects on the electronic structure we have grouped the atom projected densities of states by their respective nanowire sizes: (i) 4-4 in fig. 8.9; (ii) 4-6 in fig. 8.10; (iii) 4-8 in fig. 8.11; and (iv) 6-6 in fig. 8.12. A generalised schematic of the relative atomic positions is presented in fig. 8.8 to aid the reader with atom location responsible for the DoS presented in figs. 8.9 to 8.12.

Silicon atoms located in the centre of the nanowires (site O in figs. 8.9 to 8.12) are expected to be the most isolated from the effects of surfaces and interfaces, enabling us to understand changes dominated by the anisotropic strain environment. Changes to the projected DoS with respect to size and composition at the centre of the core are very limited, with a slight shift of the valence band toward the

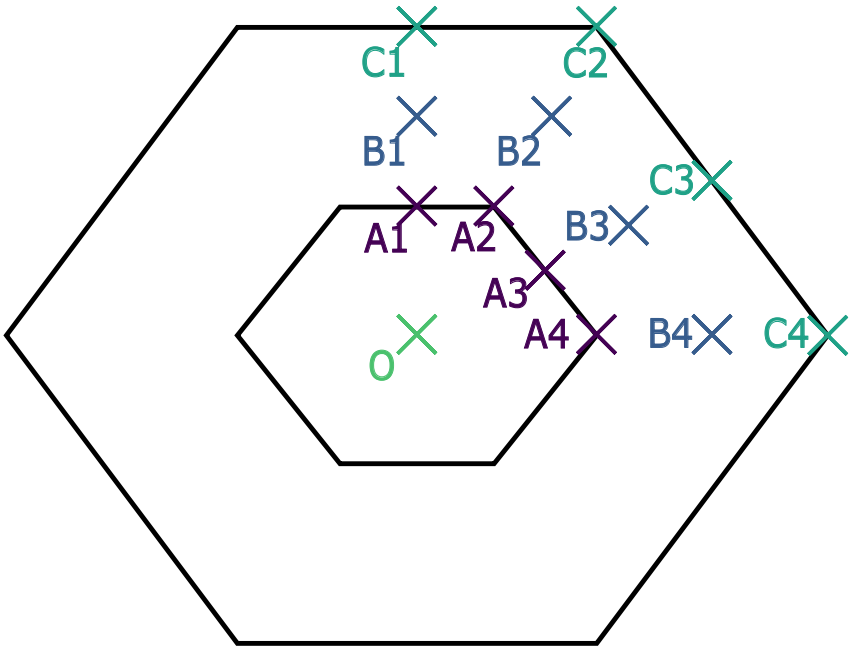


**Figure 8.8:** Scematic diagram illustrating the relative positions of atoms used to produce projected DoS. The O and A sites represent Si atoms, whilst B and C sites represent Ge. Colours used to represent the points are matched to those in the DoS figures. Site O marks the central core atom, lines drawn from: O $\rightarrow$ C1 are parallel to $\langle 001 \rangle$ bonds; O $\rightarrow$ C2 lie along the intersection of the $\langle 001 \rangle - \langle 111 \rangle$ interface/vertex; O $\rightarrow$ C3 are parallel to $\langle 111 \rangle$ bonds; and O $\rightarrow$ C4 lie along the intersection of the $\langle 111 \rangle - \langle 111 \rangle$ interface/vertex.

Fermi level. Tensile strain increases in the axial (table 7.4) and $\langle 001 \rangle$ (fig. 7.5(a)) directions for 4-X nanowires with very little change in the strain of $\langle 111 \rangle$ bonds (fig. 7.5(b)) implying this upshift of the valence band is driven by increases in axial and $\langle 001 \rangle$ tensile strains.

Silicon atoms at the interface (sites A1-4 in figs. 8.9 to 8.12) are subject to both changes in the local strain environment and chemical environment since they share bonds with the germanium shell. Atoms at the $\langle 001 \rangle$ interface (site A1) and $\langle 001 \rangle - \langle 111 \rangle$ interfacial vertex (site A2) exhibit nearly identical DoS, even comparing across all nanowire sizes. Both of these sites show little change in the conduction band energy range and most of the change comes from the upshift in the valence band region of the DoS with increasing shell thickness. We attribute these changes to increasing tensile strain in the $\langle 001 \rangle$ bonds (fig. 7.5(a)) and axial direction (table 7.4), however, one must account for the reduced $\langle 111 \rangle$ strain at the interface (fig. 7.5(b)) which leads to a reduced difference between 4-6/6-6 and 4-8 valence band edges. DoS for atoms at the centre of the $\langle 111 \rangle$ interface (site A3) have very similar valence band shifts compared to those A1-2, i.e. shifts due to the strain environment, with the most significant difference being the introduction of states in the conduction band near the Fermi level of site A3 DoS. Atoms at the $\langle 111 \rangle - \langle 111 \rangle$ interfacial vertex (site A4) exhibit much stronger shifts in the valence band as compared to sites A1-3 owing to the reduced effect of strain relaxation in $\langle 111 \rangle$ bonds in the core (fig. 7.5(b)).

Germanium atoms in the middle of the shell at sites B1-2 (figs. 8.9 to 8.12)) exhibit an upshift of valence band states toward the Fermi level, demonstrating their responsibility in closing the band gap of our nanowire models under increasing shell deposition. Furthermore, conduction band states show a relatively small downshift due to a reduction in compressive strains in the shell with increasing shell deposition. Comparison of the conduction states at sites B1-2 for the 4-8 (fig. 8.11) and 6-6 (fig. 8.12) nanowire models reveals their relative insensitivity to the shell size, whilst there is a marked increase in the axial (table 7.4) and $\langle 111 \rangle$ (fig. 7.5(d)) strain environments. For all B3 sites we find a slight upshift in the valence band and down-

shift in conduction band states under increasing deposition, implying these effects are primarily due to the increasingly Ge rich environment. Atoms at site B4 exhibit a slight upshift in the valence states with increasing deposition and most interestingly the conduction states shift away from the Fermi level with the shift correlated to the interplay between core size and strain.

Germanium atoms at the $\langle 001 \rangle$ nanowire surface (site C1) show very little shifting of either the conduction or valence states. However, we do see a shifting of two localised states (between -1.2 and -1.1 eV in the 4-4 nanowire) toward the Fermi energy in the 4-6, 4-8 and 6-6 nanowire models consistent with changes in the tensile strain at the surface reconstructions (fig. 7.5(c)). Atoms at the $\langle 001 \rangle - \langle 111 \rangle$ surface vertices (site C2) exhibit a downshift of localised conduction band states (around 0.25 eV in the 4-4 model) with the states merging under increasing shell size, corresponding to a decrease in the compressive strain in $\langle 111 \rangle$ bonds (fig. 7.5(d)). The strain environment in the $\langle 001 \rangle$ and $\langle 111 \rangle$ bond directions (figs. 7.5(c) and 7.5(d) respectively), as well as the axial strain in the shell (table 7.4), show a reduction in the compressive strain at site C3. Atoms at the $\langle 111 \rangle$ surface (site C3) show an upshift in the valence states and downshift in the conduction states, implying these atoms are partially responsible for the closing of the band gap which is due to the diminishing compressive strain with increasing shell deposition and NW size. Examination of the DoS close to the valence band edge for site C4 shows a reduction in the number of states with increasing shell deposition and increasing NW size, signifying the states at this vertex play a diminishing role in the total electronic structure.

So far we have primarily analysed the results of single sites over all nanowire model sizes, however, it is useful to briefly discuss trends of all sites within a single nanowire size. The 4-4 NW (see fig. 8.9) demonstrates similarities between the DoS of sites along the same sampling direction, e.g. A1 and A2 are very similar as are B1 - B2, C1 - C2 and A3 - A4. However, comparisons between sites that lie along $\langle 001 \rangle$ (sites X1) and $\langle 111 \rangle$ (X3) bond directions show there are two distinct sets of DoS that differ based on the influence of surface/interface proximity. DoS for the

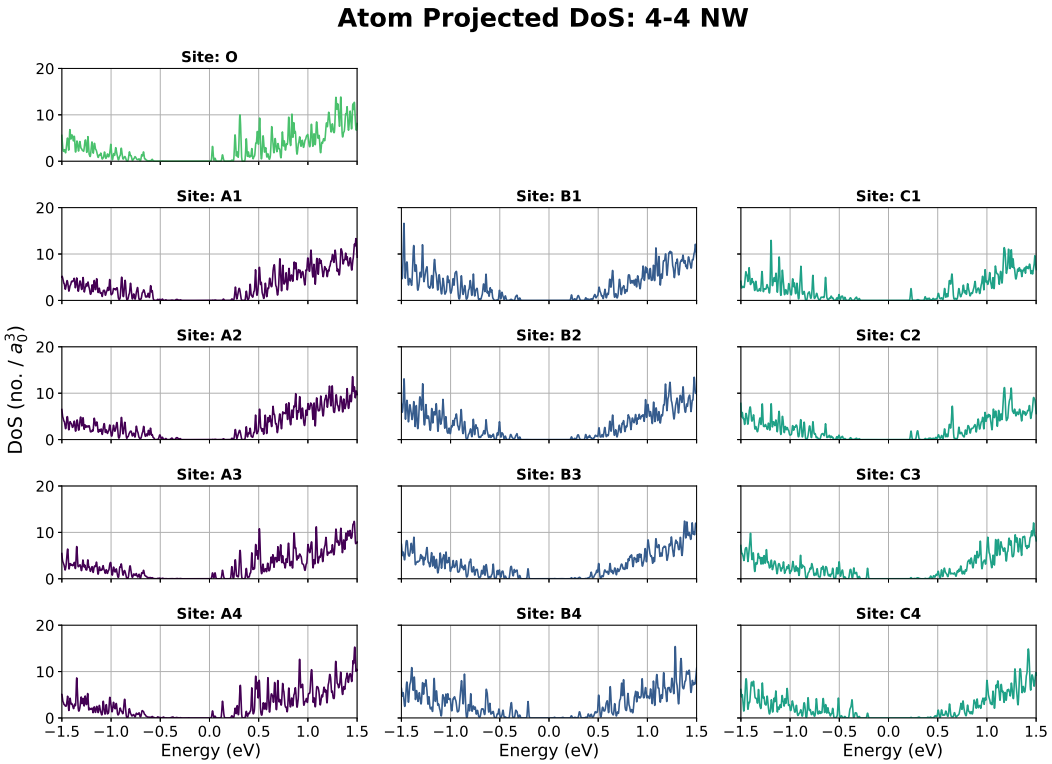


**Figure 8.9:** Atom projected DoS for a curated selection of atoms in our relaxed 4-4 Si (core) - Ge (shell) NW model. A generalised map of the relative atomic positions can be found in fig. 8.8 where the colours represent the region of the NW occupied by the atoms.

4-6 NW (fig. 8.10) are very similar to the 4-4 case, whilst the 4-8 NW (fig. 8.11) *do not* share this similarity. For the 4-8 NW the similarities seem to be region dependent, i.e. whether they're at the interface (AX sites), in the shell (BX) or at the surface (CX). Looking back at the strain maps in fig. 7.5 this can be understood as an effect due to the shallower gradients of strain along the bond directions. The 4-4 NW has very little material between the interfaces and surfaces, whilst the 4-8 has a large amount of shell material and has a smaller compressive strain in the shell, especially in the $\langle 001 \rangle$ bond direction. The 6-6 NW model (fig. 8.12) exhibits both of the trends seen in the 4-X NWs, and examination of the strain environment indicates a very similar strain environment to the 4-6 NW model. This indicates that the effects of the surfaces/interfaces do indeed become less important to the total electronic structure of larger nanowires, however, the effects of composition offer a method to tune the electronic structure of these large nanowires.

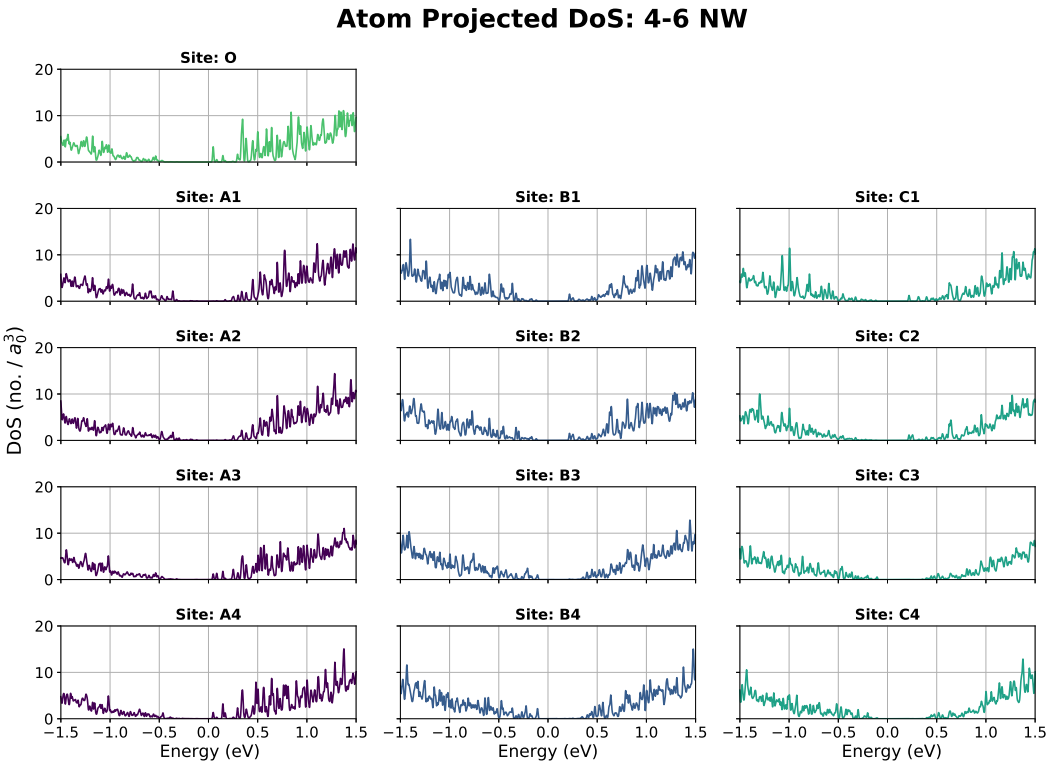


**Figure 8.10:** Atom projected DoS for a curated selection of atoms in our relaxed 4-6 Si (core) - Ge (shell) NW model. A generalised map of the relative atomic positions can be found in fig. 8.8 where the colours represent the region of the NW occupied by the atoms.

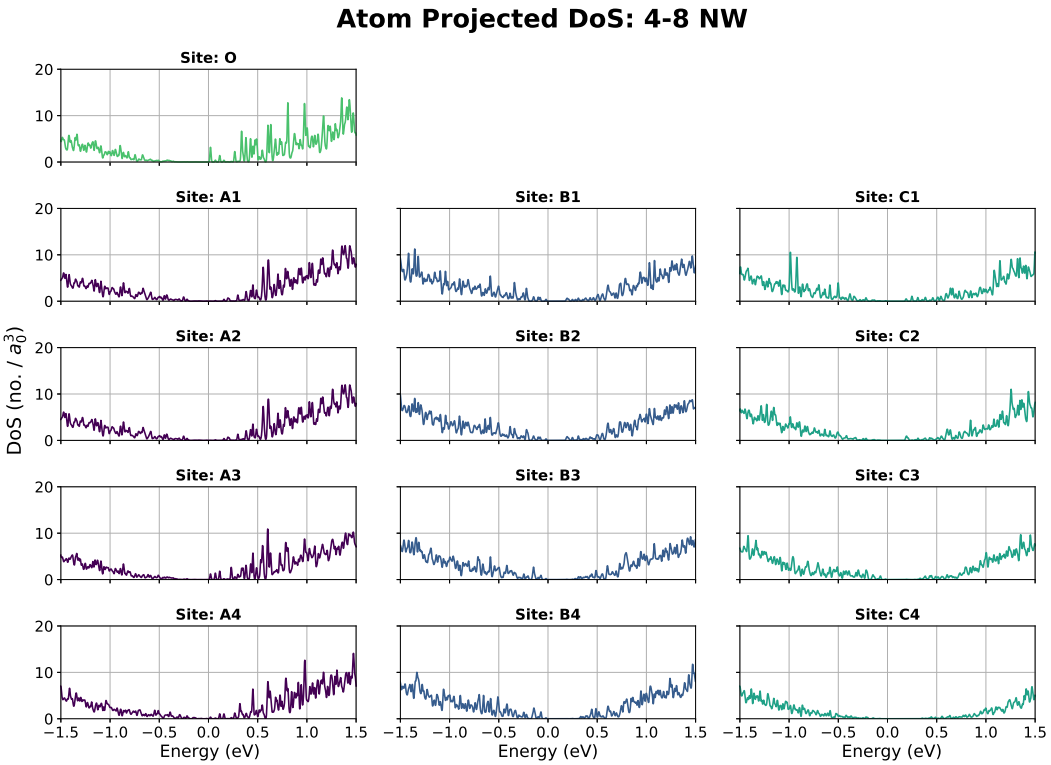


**Figure 8.11:** Atom projected DoS for a curated selection of atoms in our relaxed 4-8 Si (core) - Ge (shell) NW model. A generalised map of the relative atomic positions can be found in fig. 8.8 where the colours represent the region of the NW occupied by the atoms.

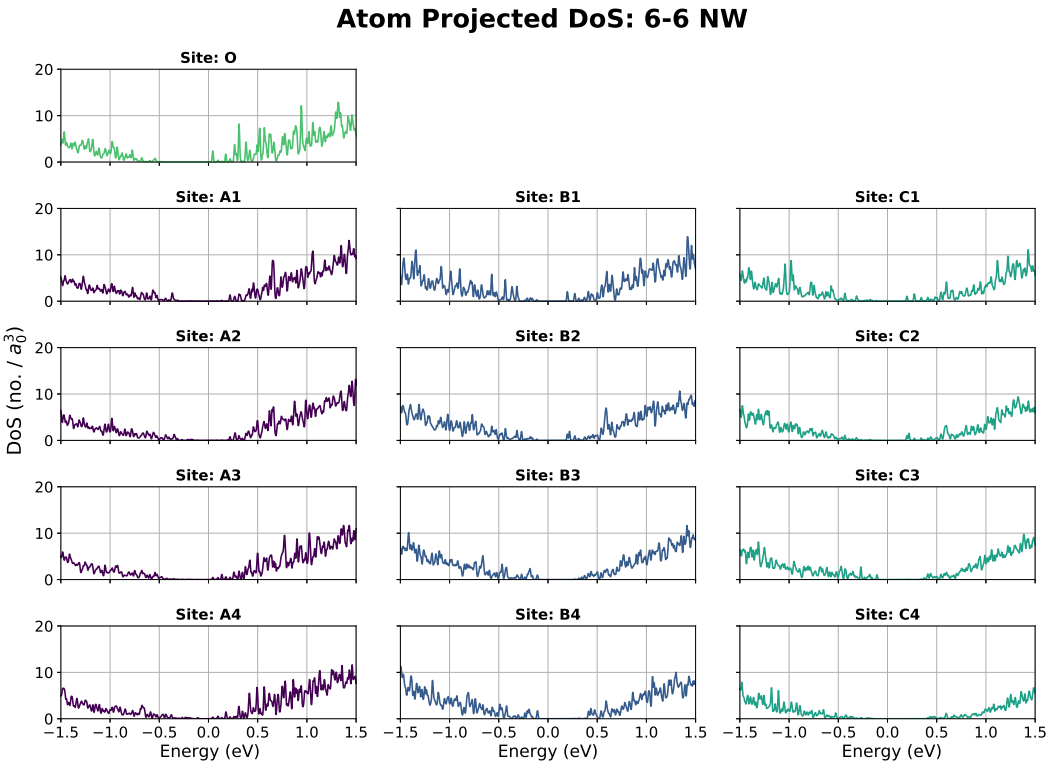


**Figure 8.12:** Atom projected DoS for a curated selection of atoms in our relaxed 6-6 Si (core) - Ge (shell) NW model. A generalised map of the relative atomic positions can be found in fig. 8.8 where the colours represent the region of the NW occupied by the atoms.

## 8.4 Conclusion

Building an understanding of the electronic structure of core-shell nanowires and the physical properties which affect it are paramount to further development of devices. We have found that the size of nanowire models offers a crucial insight to the direct to indirect band gap transition of Si (core) - Ge (shell) nanowires, which has been observed in the literature [183], but for small nanowires using applied uniaxial strain. Whilst these models are useful for ascertaining the existence of such a transition, they do not take in to consideration the effects due to larger size of experimentally observable nanowires and have failed to characterise the *intrinsic* strain contributions which determine this transition for relaxed structures. However, our findings for the effective electron masses match very well with the literature, whilst effective hole masses exhibit similar trends but are actually smaller than reported in the literature which we attribute to the effects of surface reconstructions [183].

Band offsets presented in section 8.3.2 agree with the general trends found in the literature [37, 227]. Whilst the conduction band offsets of our models are reassuringly close to those found by Yang *et al* [37], the valence band offsets are found to be almost double that of Yang *et al*. Comparison of the Yang *et al* and Huang & Yang papers reveal the latter paper uses *much* smaller nanowire models and finds much *larger* band offsets. Thus, we are safe to conclude that the larger valence band offsets found in our work, as compared to Yang *et al*, are due to surface reconstructions and highlight the importance of larger scale electronic structure calculations.

# Chapter 9

# Conclusions

Core-shell nanowires have provided us with *both* outstanding physical properties to model and an ideal testbed to push the usage and development of CONQUEST. From the start of this PhD we have been simultaneously modelling using the best methods available to us whilst pushing the testing and development of more accurate methods and useful features for materials characterisation. In this final chapter we shall summarise the key results from each chapter to paint the "bigger picture" and aid in more broad suggestions of future research directions.

We start the results portion of this thesis with the testing of CONQUEST's own basis set generation code[1] in Chapter 3. This allowed us to use the pseudopotentials of Hamann [130] as per the `PseudoDojo` framework [109] which have been shown to be the most accurate norm-conserving pseudopotentials as evidenced in the Δ-study [96]. Two methodologies for the determination of basis function extent were presented and we tested these against plane-wave calculations using the identical basis. Findings from this chapter indicated that *both* methods performed well in molecular systems studied. Solid state systems presented in this thesis showed mixed results for both methods which we have found to be caused by some states being poorly confined. However, the merit of having two methods for confinement, and comparing to plane-wave calculations, enabled us to determine *which* states are poorly described. We do find, generally, that larger basis sets are required for comparable accuracy to plane-wave DFT and the development of methods for making

[1] Writing of this code is not attributed to the author and primarily the work of Prof. David R. Bowler.

large-scale DFT calculations with such basis set sizes are invaluable.

Taking CONQUEST from a development code to a freely accessible, general purpose DFT code was always high on the developers priorities list. One contribution which took CONQUEST closer to its initial release in 2020 was the implementation of the stress tensor, see Chapter 4. In this chapter we showed the individual contributions to stress and demonstrated our implementation is correct, comparing our calculated stress to finite differences of energy-volume curves. A fortuitous initial comparison of stress calculated by $O(N)$ compared to exact diagonalisation lead the author to theoretical work on the locality of density matrices, motivating the work in Chapter 5.

In Chapter 5 we used comparisons between $O(N)$ and exact diagonalisation calculations as a measure of density matrix decay rates, which are known to be related to the band gap, and quantified the error due to density matrix truncation. Using C, Si and Ge as a crude method of varying the band gap, and hence the decay rate of the density matrix, we found that forces are the least affected by density matrix truncation, followed by energy and then stress. This subject matter also presented an opportunity to probe the accuracy of $O(N)$ calculated lattice parameters and bulk moduli as compared to exact diagonalisation. We found that minimum energy derived lattice parameters are relatively unaffected by density matrix truncation and in general the bulk moduli are within a few percent at the smallest $\mathbf{L}$-ranges suggesting that elastic properties will require moderate values of density matrix cut off to be within 1% of those calculated by diagonalisation.

Whilst the locality of the density matrix does affect the forces for $O(N)$ calculations of small band gap materials, even with a small density matrix cutoff this equates to a 10% error[2]. This error will be small enough to proceed with the $O(N)$ structural relaxations of nanowires presented in chapter 6. In this chapter we show that Vegard's law is a poor approximation for estimating the axial lattice parameter in Si (core) - Ge (shell) nanowires. Furthermore, we present strain mapping for our

[2]Results in Chapter 5 show that these errors are *highly* band gap dependent, whilst results (and references) in Chapter 8 show the band gap of core-shell nanowires to be between those of bulk Si or Ge. Hence, the usage/transferability of our 10% error estimate found in Chapter 5 is well founded.

nanowires examining strain in the $\langle 001 \rangle$ and $\langle 111 \rangle$ bond directions, revealing the highly anisotropic strain environments present.

In light of the results in Chapter 3 and development of multi-site support functions enabling exact diagonalisation calculations of Si (core) - Ge (shell) nanowires, accurate calculation mechanical properties of core-shell nanowires were now possible. Using a TZTP basis we accurately determined the Young's modulus and Poisson ratios, finding that an increase in Ge shell deposition results in reductions to the Young's modulus but an increase to the Poisson ratio. Additionally, we found the Poisson ratios of these nanowire structures to be anisotropic.

Lastly, we arrive at the electronic structure results of chapter 8 where we find that the *intrinsic* uniaxial strain is responsible for Si (core) - Ge (shell) nanowires to transition from a direct gap to indirect gap structure when the total uniaxial strain is above 0.5%, which was driven by increased shell deposition. Effective hole masses were found to increase with increasing intrinsic shell strain and that they are lighter than those found in unreconstructed core-shell nanowires. We also found that the valence band offset is strongly linked to the intrinsic shell strain, increasing as compressive shell strain is increased. We also observe that the valence band offsets reported here are larger than those reported in the literature and attributed to the surface reconstructions also, demonstrating the importance of large-scale atomic structure modelling.

In this thesis we have shown that CONQUEST basis methods are able to reproduce results with plane-wave accuracy, with improved computational efficiency through our equal radii basis set generation methodology without severely compromising calculation accuracy. We have successfully made CONQUEST a more complete simulation software package via the implementation of stress calculation, which will enable the future implementation of Green-Kubo transport calculations. We have developed an understanding of the approximation made within the $O(N)$ methodology and their effect on calculation of materials properties. This understanding is crucial to future use of CONQUEST's $O(N)$ method since it will inform users how the band gap of a material will impact simulation accuracy and how to

account for this by using a larger density matrix range.

Strain maps produced in Chapters 6 and 7 will provide a valuable guide to the wider nanowire research community for the location of doping sites, dependent on the size of dopant atoms. When strain maps are combined with the atom projected DoS results of Chapter 8 we are able to develop an atomic picture of how the local strain environments enable the tuning of the band gap, an important result for the advancement of nanowire derived MOSFETs. Should future nanowire MOSFET designs leave the $\langle 001 \rangle$ surface reconstructions of our nanowire models intact, then: (i) the lighter effective hole masses predicted will yield nanowires with improved hole mobility and faster switching speeds; and (ii) the larger confinement potentials attributed to these reconstructions will improve the robustness of carrier separation and enable higher operational temperatures of MOSFET devices. Thus, the results presented in this thesis demonstrate the potential of large-scale simulation with CONQUEST and how it is leveraged for considerable insight to further the field of nanowire MOSFETs.

# Appendix A

# Supporting information for NWs

## A.1 Birch - Murnaghan for Si (core) - Ge (shell) nanowires

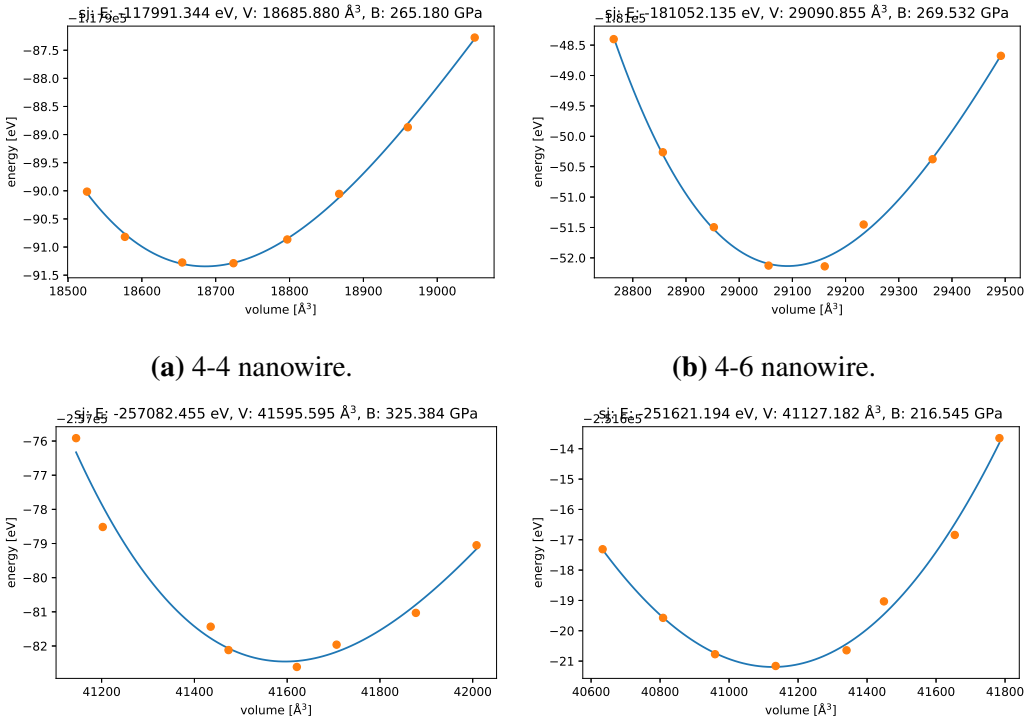


**(a)** 4-4 nanowire.

**(b)** 4-6 nanowire.

**(c)** 4-8 nanowire.

**(d)** 6-6 nanowire.

**Figure A.1:** Birch - Murnaghan equation of states for determining optimal nanowire volume.

## A.2 Young's modulus by finite differences

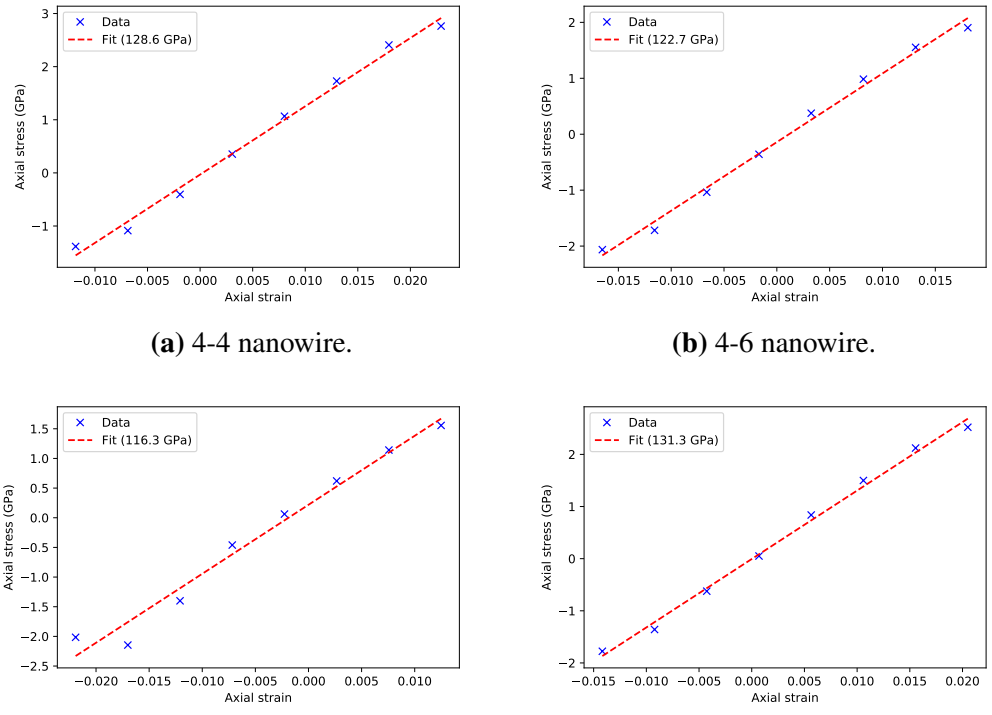


**(a)** 4-4 nanowire.

**(b)** 4-6 nanowire.

**(c)** 4-8 nanowire.

**(d)** 6-6 nanowire.

**Figure A.2:** Young's modulus determined by methods outlined in section 7.3.3. Values determined here to represent the general trends only since variations of nanowire volume and energy are unavoidable. Such fluctuations are relatively small, although stress converges much more rapidly and will only encode variations of the cross-sectional area, reducing the error present in values determined.

## A.3 Strain mapping code

```
PROGRAM NW_TRI_BOND
IMPLICIT NONE

INTEGER, PARAMETER  ::  my_kind = kind(1.d0)
TYPE position
REAL(kind=my_kind)  ::  x,y,z
END TYPE
TYPE atom
TYPE(POSITION)  ::  pos
INTEGER :: atom_type
REAL(kind=my_kind)  ::  radial_pos
END TYPE
TYPE(atom),ALLOCATABLE,DIMENSION(:) ::  atom_nw
REAL(kind=my_kind), parameter ::  tol=0.5, bond_length=4.6
INTEGER,ALLOCATABLE,DIMENSION(:,:,:,:)::no_bonds
REAL(kind=my_kind),ALLOCATABLE,DIMENSION(:,:,:,:) ::  bond_sum,dum_bond_sum
INTEGER ::  i,j,k,l,m,n,no_atoms,grid_points_x,grid_points_z,grid_x,grid_z,no,&
            & interp_width
REAL(kind=my_kind)  ::  grid_spacing,xx_NW,yy_NW,zz_NW,dum
REAL(kind=my_kind)  ::  centre_x,centre_z,dist,dx,dy,dz,bond_1,bond_2,&
                        & x_max,x_min,z_max,z_min

OPEN(9,file="dat.in")
OPEN(10,file="POS.NW.PASS")
OPEN(11,file="shell_map.1")
OPEN(12,file="shell_map.2")
OPEN(13,file="shell_map.3")
OPEN(14,file="core_map.1")
OPEN(15,file="core_map.2")
OPEN(16,file="core_map.3")
READ(10,*) xx_NW,dum,dum
READ(10,*) dum,yy_NW,dum
READ(10,*) dum,dum,zz_NW
READ(10,*) no_atoms
READ(9,*) grid_spacing,interp_width,bond_1,bond_2

grid_points_x=CEILING(xx_NW/grid_spacing)
grid_points_z=CEILING(zz_NW/grid_spacing)
print*,"grid points:",grid_points_x,grid_points_z
ALLOCATE(atom_nw(no_atoms),no_bonds(2,3,grid_points_x,grid_points_z),&
        & bond_sum(2,3,grid_points_x,grid_points_z))
ALLOCATE(dum_bond_sum(2,3,grid_points_x,grid_points_z))

no_bonds(:,:,:,:)=0
```

```
bond_sum(:,:,:,:)=0.0

DO i=1,no_atoms
  READ(10,*)  atom_nw(i)%pos%x,atom_nw(i)%pos%y,atom_nw(i)%pos%z,&
              atom_nw(i)%atom_type
END DO

DO i=1,no_atoms
  DO j=i+1,no_atoms
    IF (atom_nw(i)%atom_type .eq. atom_nw(j)%atom_type) THEN
      dx=atom_nw(i)%pos%x-atom_nw(j)%pos%x
      IF (abs(dx) >   xx_NW*0.5) dx = dx - sign(xx_NW,dx)
      dy=atom_nw(i)%pos%y-atom_nw(j)%pos%y
      IF (abs(dy) >   yy_NW*0.5) dy = dy - sign(yy_NW,dy)
      dz=atom_nw(i)%pos%z-atom_nw(j)%pos%z
      IF (abs(dz) >   zz_NW*0.5) dz = dz - sign(zz_NW,dz)
      dist=sqrt((dx*dx)+ (dy*dy)+(dz*dz))
      IF ((dist .gt. (bond_length-tol)) .AND. &
      & (dist .lt. (bond_length+tol))) THEN
        grid_x  = int((atom_nw(i)%pos%x - &
        & ((atom_nw(i)%pos%x-atom_nw(j)%pos%x)*0.5))/grid_spacing)
        grid_z  = int((atom_nw(i)%pos%z - &
        & ((atom_nw(i)%pos%z-atom_nw(j)%pos%z)*0.5))/grid_spacing)
        IF(ABS(dy) .gt. 3.0) THEN
          no_bonds(atom_nw(i)%atom_type,3,grid_x,grid_z) = &
          & no_bonds(atom_nw(i)%atom_type,3,grid_x,grid_z)+1
          bond_sum(atom_nw(i)%atom_type,3,grid_x,grid_z) = &
          & bond_sum(atom_nw(i)%atom_type,3,grid_x,grid_z)+dist
        ELSE
          IF((dx > 0.0)) THEN
            IF (dz > 0.0) THEN
              no_bonds(atom_nw(i)%atom_type,1,grid_x,grid_z) = &
              & no_bonds(atom_nw(i)%atom_type,1,grid_x,grid_z)+1
              bond_sum(atom_nw(i)%atom_type,1,grid_x,grid_z) = &
              & bond_sum(atom_nw(i)%atom_type,1,grid_x,grid_z)+dist
            ELSE
              no_bonds(atom_nw(i)%atom_type,2,grid_x,grid_z) = &
              & no_bonds(atom_nw(i)%atom_type,2,grid_x,grid_z)+1
              bond_sum(atom_nw(i)%atom_type,2,grid_x,grid_z) = &
              & bond_sum(atom_nw(i)%atom_type,2,grid_x,grid_z)+dist
            END IF
          ELSE
            IF(dz>0.0) THEN
              no_bonds(atom_nw(i)%atom_type,2,grid_x,grid_z) = &
              & no_bonds(atom_nw(i)%atom_type,2,grid_x,grid_z)+1     !type 2
              bond_sum(atom_nw(i)%atom_type,2,grid_x,grid_z) = &
```

```
91                & bond_sum(atom_nw(i)%atom_type,2,grid_x,grid_z)+dist
92              ELSE
93                no_bonds(atom_nw(i)%atom_type,1,grid_x,grid_z) = &
94                & no_bonds(atom_nw(i)%atom_type,1,grid_x,grid_z)+1      !type 1
95                bond_sum(atom_nw(i)%atom_type,1,grid_x,grid_z) = &
96                & bond_sum(atom_nw(i)%atom_type,1,grid_x,grid_z)+dist
97              END IF
98            END IF
99          END IF
100       END IF ! bonded
101     END IF ! atom types
102   END DO
103 END DO
104
105 DO k=1,2
106   DO l=1,3
107     DO i=1,grid_points_x
108       DO j=1,grid_points_z
109         IF(no_bonds(k,l,i,j) > 0) THEN
110           bond_sum(k,l,i,j)=(bond_sum(k,l,i,j)/no_bonds(k,l,i,j))
111         ELSE
112           IF(k==1) THEN
113             bond_sum(k,l,i,j)=0.0
114           ELSE
115             bond_sum(k,l,i,j)=0.0
116           END IF
117         END IF
118       END DO
119     END DO
120   END DO
121 END DO
122
123 DO k=1,2
124   DO l=1,3
125     DO i=1,grid_points_x
126       DO j=1,grid_points_z
127         IF(no_bonds(k,l,i,j) == 0) THEN
128           x_min=0.0
129           x_max=0.0
130           z_min=0.0
131           z_max=0.0
132           no=0
133           DO m=i-interp_width,i+interp_width
134             DO n=j-interp_width,j+interp_width
135               IF((m .ge. 1) .AND. (m .le. grid_points_x) &
136               & .AND. (n .ge. 1) .AND. (n .le. grid_points_z)) THEN
```

```
137                 IF (no_bonds(k,l,m,n) > 0) THEN
138                   x_min=x_min+bond_sum(k,l,m,n)
139                   no=no+1
140                 END IF
141               END IF
142             END DO
143           END DO
144           IF(no==0) THEN
145             IF (k==1) THEN
146               dum_bond_sum(k,l,i,j)=bond_1
147             ELSE
148               dum_bond_sum(k,l,i,j)=bond_2
149             END IF
150           ELSE
151             dum_bond_sum(k,l,i,j)=((x_min)/no)
152           END IF
153         END IF
154       END DO
155     END DO
156   END DO
157 END DO
158
159 DO k=1,2
160   DO l=1,3
161     DO i=1,grid_points_x
162       DO j=1,grid_points_z
163         IF(no_bonds(k,l,i,j) == 0) THEN
164           bond_sum(k,l,i,j)=dum_bond_sum(k,l,i,j)
165         END IF
166       END DO
167     END DO
168   END DO
169 END DO
170
171 DO i=1,grid_points_x
172   DO j=1,grid_points_z
173     WRITE(14,*) i*grid_spacing,j*grid_spacing, &
174                 & ((bond_sum(1,1,i,j)-bond_1)/bond_1)*100.0
175     WRITE(15,*) i*grid_spacing,j*grid_spacing, &
176                 & ((bond_sum(1,2,i,j)-bond_1)/bond_1)*100.0
177     WRITE(16,*) i*grid_spacing,j*grid_spacing, &
178                 & ((bond_sum(1,3,i,j)-bond_1)/bond_1)*100.0
179     WRITE(11,*) i*grid_spacing,j*grid_spacing, &
180                 & ((bond_sum(2,1,i,j)-bond_2)/bond_2)*100.0
181     WRITE(12,*) i*grid_spacing,j*grid_spacing, &
182                 & ((bond_sum(2,2,i,j)-bond_2)/bond_2)*100.0
```

```
183     WRITE(13,*) i*grid_spacing,j*grid_spacing, &
184                 & ((bond_sum(2,3,i,j)-bond_2)/bond_2)*100.0
185   END DO
186   WRITE(11,*)
187   WRITE(12,*)
188   WRITE(13,*)
189   WRITE(14,*)
190   WRITE(15,*)
191   WRITE(16,*)
192 END DO
193
194 END PROGRAM NW_TRI_BOND
```

**Listing A.1:** Code for producing strain maps.

# Bibliography


[1] Knut Blind, Mirko Böhm, Paula Grzegorzewska, Andrew Katz, Sachiko Muto, Sivan Pätsch, and Torben Schubert. The impact of Open Source Software and Hardware on technological independence, competitiveness and innovation in the EU economy. Technical report, Brussels, 2021.

[2] Hari Singh Nalwa. *Nanostructured materials and nanotechnology: concise edition*. Elsevier, 2001.

[3] Nicolás Agraït, Alfredo Levy Yeyati, and Jan M. van Ruitenbeek. Quantum properties of atomic-sized conductors. *Physics Reports*, 377(2-3):81–279, 2003.

[4] Ruoxue Yan, Daniel Gargas, and Peidong Yang. Nanowire photonics. *Nature Photonics*, 3(10):569–576, 2009.

[5] Daniel M. Lyons, Kevin M. Ryan, Michael A. Morris, and Justin D. Holmes. Tailoring the Optical Properties of Silicon Nanowire Arrays through Strain. *Nano Letters*, 2(8):811–816, 2002.

[6] Deyu Li, Yiying Wu, Philip Kim, Li Shi, Peidong Yang, and Arun Majumdar. Thermal conductivity of individual silicon nanowires. *Applied Physics Letters*, 83(14):2934–2936, 2003.

[7] Stéphane Cuenot, Christian Frétigny, Sophie Demoustier-Champagne, and Bernard Nysten. Surface tension effect on the mechanical properties of nanomaterials measured by atomic force microscopy. *Physical Review B - Condensed Matter and Materials Physics*, 69(16):1–5, 2004.

[8] G. Stan, C. V. Ciobanu, P. M. Parthangal, and R. F. Cook. Diameter-dependent radial and tangential elastic moduli of ZnO nanowires. *Nano Letters*, 7(12):3691–3697, 2007.

[9] Matthieu Jamet, André Barski, Thibaut Devillers, Valier Poydenot, Romain Dujardin, Pascale Bayle-Guillemaud, Johan Rothman, Edith Bellet-Amalric, Alain Marty, Joël Cibert, Richard Mattana, and Serge Tatarenko. High-curie-temperature ferromagnetism in self-organized Ge 1-xMnx nanocolumns. *Nature Materials*, 5(8):653–659, 2006.

[10] Olga Kazakova, Jaideep S. Kulkarni, Justin D. Holmes, and Sergej O. Demokritov. Room-temperature ferromagnetism in Ge1-xMnx nanowires. *Physical Review B - Condensed Matter and Materials Physics*, 72(9):1–6, 2005.

[11] S. Majumdar, A. K. Das, and S. K. Ray. Magnetic semiconducting diode of p -Ge1-x Mnx /n-Ge layers on silicon substrate. *Applied Physics Letters*, 94(12):98–101, 2009.

[12] Qing Xie, Xue Lin, Yanzhi Wang, Shuang Chen, Mohammad Javad Dousti, and Massoud Pedram. Performance Comparisons between 7-nm FinFET and Conventional Bulk CMOS Standard Cell Libraries. *IEEE Transactions on Circuits and Systems II: Express Briefs*, 62(8):761–765, 2015.

[13] Anil Kumar Bansal, Ishita Jain, Terence B. Hook, and Abhisek Dixit. Series resistance reduction in stacked nanowire FETs for 7-nm CMOS technology. *IEEE Journal of the Electron Devices Society*, 4(5):266–272, 2016.

[14] Ying Sun, Taige Dong, Linwei Yu, Jun Xu, and Kunji Chen. Planar Growth, Integration, and Applications of Semiconducting Nanowires. *Advanced Materials*, 32(27):1903945, 2020.

[15] Younan Xia, Peidong Yang, Yugang Sun, Yiying Wu, Brian Mayers, Byron Gates, Yadong Yin, Franklin Kim, and Haoquan Yan. One-Dimensional

Nanostructures: Synthesis, Characterization, and Applications. *Advanced Materials*, 15(5):353–389, 2003.

[16] N. Wang, Y. Cai, and R. Q. Zhang. Growth of nanowires. *Materials Science and Engineering R: Reports*, 60(1-6):1–51, 2008.

[17] Alfredo M. Morales and Charles M. Lieber. A laser ablation method for the synthesis of crystalline semiconductor nanowires. *Science (New York, N.Y.)*, 279(5348):208–11, 1998.

[18] Justin D. Holmes, Keith P. Johnston, R. Christopher Doty, and Brian A. Korgel. Control of thickness and orientation of solution-grown silicon nanowires. *Science (New York, N.Y.)*, 287(5457):1471–3, 2000.

[19] Li Ma, Jianguang Wang, Jijun Zhao, and Guanghou Wang. Anisotropy in stability and Young's modulus of hydrogenated silicon nanowires. *Chemical Physics Letters*, 452(1-3):183–187, 2008.

[20] Yong Zhu, Feng Xu, Gquan Qin, Wayne Y. Fung, and Wei Lu. Mechanical properties of vapor - Liquid - Solid synthesized silicon nanowires. *Nano Letters*, 9(11):3934–3939, 2009.

[21] Xinyuan Zhao, C. M. Wei, L. Yang, and M. Y. Chou. Quantum confinement and electronic properties of silicon nanowires. *Physical Review Letters*, 92(23):236805, 2004.

[22] Yue Wu, Yi Cui, Lynn Huynh, Carl J. Barrelet, David C. Bell, and Charles M. Lieber. Controlled growth and structures of molecular-scale silicon nanowires. *Nano Letters*, 4(3):433–436, 2004.

[23] Volker Schmidt, Stephan Senz, and Ulrich Gösele. Diameter-dependent growth direction of epitaxial silicon nanowires. *Nano Letters*, 5(5):931–935, 2005.

[24] C. X. Wang, Masahiro Hirano, and Hideo Hosono. Origin of diameter-dependent growth direction of silicon nanowires. *Nano Letters*, 6(7):1552–1555, 2006.

[25] A. Lugstein, M. Steinmair, Y. J. Hyun, G. Hauer, P. Pongratz, and E. Bertagnolli. Pressure-induced orientation control of the growth of epitaxial silicon nanowires. *Nano Letters*, 8(8):2310–2314, 2008.

[26] Charles Kittel. *Introduction to Solid State Physics*. Wiley, seventh edition, 1996.

[27] J R Hook and H E Hall. *Solid State Physics*. Manchester Physics Series. John Wiley & Sons, Incorporated, second edition, 1991.

[28] Naoki Fukata, Masanori Mitome, Takashi Sekiguchi, Yoshio Bando, Melanie Kirkham, Jung-Il Hong, Zhong Lin Wang, and Robert L. Snyder. Characterization of Impurity Doping and Stress in Si/Ge and Ge/Si CoreShell Nanowires. *ACS Nano*, 6(10):8887–8895, 2012.

[29] Lincoln J Lauhon, Mark S Gudiksen, Deli Wang, and Charles M Lieber. Epitaxial coreshell and coremultishell nanowire heterostructures. *Nature*, 420(6911):57–61, 2002.

[30] Jie Xiang, Wei Lu, Yongjie Hu, Yue Wu, Hao Yan, and Charles M. Lieber. Ge/Si nanowire heterostructures as high-performance field-effect transistors. *Nature*, 441(7092):489–493, 2006.

[31] C. Y. Wen, M. C. Reuter, J. Bruley, J. Tersoff, S. Kodambaka, E. A. Stach, and F. M. Ross. Formation of Compositionally Abrupt Axial Heterojunctions in Silicon-Germanium Nanowires. *Science*, 326(5957):1247–1250, 2009.

[32] Irene A Goldthorpe, Ann F Marshall, and Paul C Mcintyre. Inhibiting Strain-Induced Surface Roughening: Dislocation-Free Ge/Si and Ge/SiGe Core - Shell Nanowires. *Nano Letters*, 9(11):3715–3719, 2009.

[33] Yufeng Zhao and Boris I. Yakobson. What is the ground-state structure of the thinnest Si nanowires? *Physical Review Letters*, 91(3):035501/1–035501/4, 2003.

[34] R. N. Musin and Xiao-Qian Wang. Structural and electronic properties of epitaxial core-shell nanowire heterostructures. *Physical Review B*, 71(15):155318, 2005.

[35] Ryza N. Musin and Xiao Qian Wang. Quantum size effect in core-shell structured silicon-germanium nanowires. *Physical Review B - Condensed Matter and Materials Physics*, 74(16):1–5, 2006.

[36] A Nduwimana, R N Musin, A M Smith, and Xiao-Qian Wang. Spatial carrier confinement in core-shell and multishell nanowire heterostructures. *Nano letters*, 8(10):3341–4, 2008.

[37] Li Yang, Ryza N. Musin, Xiao-Qian Wang, and M. Y. Chou. Quantum confinement effect in Si/Ge core-shell nanowires: First-principles calculations. *Physical Review B*, 77(19):195325, 2008.

[38] Noor S. Mohammad. Understanding quantum confinement in nanowires: Basics, applications and possible laws. *Journal of Physics Condensed Matter*, 26(42), 2014.

[39] R. Rurali and N. Lorente. On the properties of surface reconstructed silicon nanowires. *Nanotechnology*, 16(5):1–5, 2005.

[40] R. Rurali and N. Lorente. Metallic and semimetallic silicon $\langle 100 \rangle$ nanowires. *Physical Review Letters*, 94(2):026805, 2005.

[41] Shiliang Wang, Zhiwei Shan, and Han Huang. The Mechanical Properties of Nanowires. *Advanced Science*, 4(4):1–24, 2017.

[42] D. R. Bowler, T. Miyazaki, and M. J. Gillan. Recent progress in linear scaling ab initio electronic structure techniques. *Journal of Physics Condensed Matter*, 14(11):2781–2798, 2002.

[43] David R Bowler. Atomic-scale nanowires: physical and electronic structure. *Journal of Physics: Condensed Matter*, 16(24):R721–R754, 2004.

[44] D. R. Bowler, R. Choudhury, M. J. Gillan, and T. Miyazaki. Recent progress with large-scale ab initio calculations: The CONQUEST code. *Physica Status Solidi (B) Basic Research*, 243(5):989–1000, 2006.

[45] Ayako Nakata, Jack S. Baker, Shereif Y. Mujahed, Jack T. L. Poulton, Sergiu Arapan, Jianbo Lin, Zamaan Raza, Sushma Yadav, Lionel Truflandier, Tsuyoshi Miyazaki, and David R. Bowler. Large scale and linear scaling DFT with the CONQUEST code. *The Journal of Chemical Physics*, 152(16):164112, 2020.

[46] Richard M. Martin. *Electronic Structure: Basic Theory and Practical Methods*. Cambridge University Press, 2004.

[47] M. Born and R. Oppenheimer. Zur Quantentheorie der Molekeln. *Annalen der Physik*, 389(20):457–484, 1927.

[48] M. Born and V. Fock. Beweis des Adiabatensatzes. *Zeitschrift für Physik*, 51(3-4):165–180, 1928.

[49] R. P. Feynman. Forces in Molecules. *Physical Review*, 56(4):340–343, 1939.

[50] P Hohenberg and W Kohn. Inhomogeneous Electron Gas. *Phys. Rev.*, 136(3B):B864–B871, 1964.

[51] W Kohn and L J Sham. Self-Consistent Equations Including Exchange and Correlation Effects. *Phys. Rev.*, 140(4A):A1133–A1138, 1965.

[52] D. M. Ceperley. Ground State of the Electron Gas by a Stochastic Method. *Physical Review Letters*, 45(7):566–569, 1980.

[53] Lee A Cole and J P Perdew. Calculated electron affinities of the elements. *Phys. Rev. A*, 25(3):1265–1271, 1982.

[54] J P Perdew and Alex Zunger. Self-interaction correction to density-functional approximations for many-electron systems. *Phys. Rev. B*, 23(10):5048–5079, 1981.

[55] John P Perdew and Yue Wang. Accurate and simple analytic representation of the electron-gas correlation energy. *Phys. Rev. B*, 45(23):13244–13249, 1992.

[56] S H Vosko, L Wilk, and M Nusair. Accurate spin-dependent electron liquid correlation energies for local spin density calculations: a critical analysis. *Canadian Journal of Physics*, 58(8):1200–1211, 1980.

[57] David Langreth and M. Mehl. Beyond the local-density approximation in calculations of ground-state electronic properties. *Physical Review B*, 28(4):1809–1834, 1983.

[58] A. D. Becke. Density-functional exchange-energy approximation with correct asymptotic behavior. *Physical Review A*, 38(6):3098–3100, 1988.

[59] John P. Perdew, Koblar A. Jackson, Mark R. Pederson, D. J. Singh, and Carlos Fiolhais. Atoms, molecules, solids, and surfaces: Applications of the generalized gradient approximation for exchange and correlation. *Physical Review B*, 46(11):6671–6687, 1992.

[60] John P. Perdew, Kieron Burke, and Matthias Ernzerhof. Generalized Gradient Approximation Made Simple. *Physical Review Letters*, 77(18):3865–3868, 1996.

[61] John P. Perdew, Kieron Burke, and Matthias Ernzerhof. Generalized Gradient Approximation Made Simple [Phys. Rev. Lett. 77, 3865 (1996)]. *Physical Review Letters*, 78(7):1396–1396, 1997.

[62] Jianmin Tao, John P. Perdew, Viktor N. Staroverov, and Gustavo E. Scuseria. Climbing the density functional ladder: Nonempirical metageneralized

gradient approximation designed for molecules and solids. *Physical Review Letters*, 91(14):3–6, 2003.

[63] John P. Perdew, Matthias Ernzerhof, and Kieron Burke. Rationale for mixing exact exchange with density functional approximations. *Journal of Chemical Physics*, 105(22):9982–9985, 1996.

[64] Carlo Adamo and Vincenzo Barone. Toward reliable density functional methods without adjustable parameters: The PBE0 model. *Journal of Chemical Physics*, 110(13):6158–6170, 1999.

[65] Jochen Heyd, Gustavo E. Scuseria, and Matthias Ernzerhof. Hybrid functionals based on a screened Coulomb potential. *Journal of Chemical Physics*, 118(18):8207–8215, 2003.

[66] Leonard Kleinman and D. Bylander. Efficacious Form for Model Pseudopotentials. *Physical Review Letters*, 48(20):1425–1428, 1982.

[67] G. Bachelet and M. Schlüter. Relativistic norm-conserving pseudopotentials. *Physical Review B*, 25(4):2103–2108, 1982.

[68] David Vanderbilt. Soft self-consistent pseudopotentials in a generalized eigenvalue formalism. *Phys. Rev. B*, 41(11):7892–7895, 1990.

[69] Hendrik J Monkhorst and James D Pack. Special points for Brillouin-zone integrations. *Physical Review B*, 13(12):5188–5192, 1976.

[70] W H Press, S A Teukolsky, W T Vetterling, and B P Flannery. *Numerical Recipes 3rd Edition: The Art of Scientific Computing*. Cambridge University Press, 2007.

[71] W. Kohn. Density Functional and Density Matrix Method Scaling Linearly with the Number of Atoms. *Physical Review Letters*, 76(17):3168–3171, 1996.

[72] Adam H.R. Palser and David E. Manolopoulos. Canonical purification of the density matrix in electronic-structure theory. *Physical Review B - Condensed Matter and Materials Physics*, 58(19):12704–12711, 1998.

[73] E. Hernández and M. J. Gillan. Self-consistent first-principles technique with linear scaling. *Physical Review B*, 51(15):10157–10160, 1995.

[74] E. Hernández, M. J. Gillan, and C. M. Goringe. Linear-scaling density-functional-theory technique: The density-matrix approach. *Physical Review B*, 53(11):7147–7157, 1996.

[75] Francesco Mauri, Giulia Galli, and Roberto Car. Orbital formulation for electronic-structure calculations with linear system-size scaling. *Physical Review B*, 47(15):9973–9976, 1993.

[76] R. McWeeny. Some recent advances in density matrix theory. *Reviews of Modern Physics*, 32(2):335–369, 1960.

[77] X.-P. Li, R. W. Nunes, and David Vanderbilt. Density-matrix electronic-structure method with linear system-size scaling. *Physical Review B*, 47(16):10891–10894, 1993.

[78] D.R. Bowler and M.J. Gillan. Density matrices in O(N) electronic structure calculations: theory and applications. *Computer Physics Communications*, 120(2-3):95–108, 1999.

[79] Klaus Koepernik and Helmut Eschrig. Full-potential nonorthogonal local-orbital minimum-basis band-structure scheme. *Physical Review B*, 59(3):1743–1757, 1999.

[80] B. Delley. From molecules to solids with the $DMol^3$ approach. *Journal of Chemical Physics*, 113(18):7756–7764, 2000.

[81] A S Torralba, M Todorović, V Brázdová, R Choudhury, T Miyazaki, M J Gillan, and D R Bowler. Pseudo-atomic orbitals as basis sets for the

O(N) DFT code CONQUEST. *Journal of Physics: Condensed Matter*, 20(29):294206, 2008.

[82] Otto F. Sankey and David J. Niklewski. Ab initio multicenter tight-binding model for molecular-dynamics simulations and other applications in covalent systems. *Physical Review B*, 40(6):3979–3995, 1989.

[83] José M. Soler, Emilio Artacho, Julian D. Gale, Alberto García, Javier Junquera, Pablo Ordejón, and Daniel Sánchez-Portal. The SIESTA method for ab initio order-N materials simulation. *Journal of Physics: Condensed Matter*, 14(11):2745–2779, 2002.

[84] Ayako Nakata, David R. Bowler, and Tsuyoshi Miyazaki. Efficient calculations with multisite local orbitals in a large-scale DFT code CONQUEST. *Journal of Chemical Theory and Computation*, 10(11):4813–4822, 2014.

[85] M. J. Rayson and P. R. Briddon. Highly efficient method for Kohn-Sham density functional calculations of 500-10000 atom systems. *Physical Review B - Condensed Matter and Materials Physics*, 80(20):205104, 2009.

[86] M. J. Rayson. Rapid filtration algorithm to construct a minimal basis on the fly from a primitive Gaussian basis. *Computer Physics Communications*, 181(6):1051–1056, 2010.

[87] Ayako Nakata, David R. Bowler, and Tsuyoshi Miyazaki. Optimized multisite local orbitals in the large-scale DFT program CONQUEST. *Physical Chemistry Chemical Physics*, 17(47):31427–31433, 2015.

[88] R. O. Jones. Density functional theory: Its origins, rise to prominence, and future. *Reviews of Modern Physics*, 87(3), 2015.

[89] Stefano Curtarolo, Wahyu Setyawan, Gus L.W. Hart, Michal Jahnatek, Roman V. Chepulskii, Richard H. Taylor, Shidong Wang, Junkai Xue, Kesong Yang, Ohad Levy, Michael J. Mehl, Harold T. Stokes, Denis O. Demchenko,

and Dane Morgan. AFLOW: An automatic framework for high-throughput materials discovery. *Computational Materials Science*, 58:218–226, 2012.

[90] Andrew R. Supka, Troy E. Lyons, Laalitha Liyanage, Pino D'Amico, Rabih Al Rahal Al Orabi, Sharad Mahatara, Priya Gopal, Cormac Toher, Davide Ceresoli, Arrigo Calzolari, Stefano Curtarolo, Marco Buongiorno Nardelli, and Marco Fornari. AFLOW$\pi$: A minimalist approach to high-throughput ab initio calculations including the generation of tight-binding hamiltonians. *Computational Materials Science*, 136:76–84, 2017.

[91] Anubhav Jain, Ivano E. Castelli, Geoffroy Hautier, David H. Bailey, and Karsten W. Jacobsen. Performance of genetic algorithms in search for water splitting perovskites. *Journal of Materials Science*, 48(19):6519–6534, 2013.

[92] Chu Chun Fu, Jacques Dalla Torre, François Willaime, Jean Louis Bocquet, and Alain Barbu. Multiscale modelling of defect kinetics in irradiated iron, 2005.

[93] M Friák, T Hickel, B Grabowski, L Lymperakis, A Udyansky, A Dick, D Ma, F Roters, L.-F Zhu, A Schlieter, U Kühn, Z Ebrahimi, R A Lebensohn, D Holec, J Eckert, H Emmerich, D Raabe, and J Neugebauer. Methodological challenges in combining quantum-mechanical and continuum approaches for materials science applications. *Eur. Phys. J. Plus*, 2011.

[94] Dandan Chen, Xinfu He, Genshen Chu, Xiao He, Lixia Jia, Zhaoshun Wang, Wen Yang, and Changjun Hu. An overview: multiscale simulation in understanding the radiation damage accumulation of reactor materials. *SIMULATION*, page 003754971988094, 2019.

[95] K. Lejaeghere, V. Van Speybroeck, G. Van Oost, and S. Cottenier. Error estimates for solid-state density-functional theory predictions: An overview by means of the ground-state elemental crystals. *Critical Reviews in Solid State and Materials Sciences*, 39(1):1–24, 2014.

[96] Kurt Lejaeghere, Gustav Bihlmayer, Torbjörn Björkman, Peter Blaha, Stefan Blügel, Volker Blum, Damien Caliste, Ivano E. Castelli, Stewart J. Clark, Andrea Dal Corso, Stefano De Gironcoli, Thierry Deutsch, John Kay Dewhurst, Igor Di Marco, Claudia Draxl, Marcin Dułak, Olle Eriksson, José A. Flores-Livas, Kevin F. Garrity, Luigi Genovese, Paolo Giannozzi, Matteo Giantomassi, Stefan Goedecker, Xavier Gonze, Oscar Grånäs, E. K.U. Gross, Andris Gulans, François Gygi, D. R. Hamann, Phil J. Hasnip, N. A.W. Holzwarth, Diana Iuan, Dominik B. Jochym, François Jollet, Daniel Jones, Georg Kresse, Klaus Koepernik, Emine Küçükbenli, Yaroslav O. Kvashnin, Inka L.M. Locht, Sven Lubeck, Martijn Marsman, Nicola Marzari, Ulrike Nitzsche, Lars Nordström, Taisuke Ozaki, Lorenzo Paulatto, Chris J. Pickard, Ward Poelmans, Matt I.J. Probert, Keith Refson, Manuel Richter, Gian Marco Rignanese, Santanu Saha, Matthias Scheffler, Martin Schlipf, Karlheinz Schwarz, Sangeeta Sharma, Francesca Tavazza, Patrik Thunström, Alexandre Tkatchenko, Marc Torrent, David Vanderbilt, Michiel J. Van Setten, Veronique Van Speybroeck, John M. Wills, Jonathan R. Yates, Guo Xu Zhang, and Stefaan Cottenier. Reproducibility in density functional theory calculations of solids. *Science*, 351(6280), 2016.

[97] Stefan Goedecker. Linear scaling electronic structure methods. *Reviews of Modern Physics*, 71(4):1085–1123, 1999.

[98] D. R. Bowler and T. Miyazaki. O(N) methods in electronic structure calculations. *Reports on Progress in Physics*, 75(3), 2012.

[99] D R Bowler and T Miyazaki. Calculations for millions of atoms with density functional theory: linear scaling shows its potential. *Journal of Physics: Condensed Matter*, 22(7):074207, 2010.

[100] Michiaki Arita, Sergiu Arapan, David R. Bowler, and Tsuyoshi Miyazaki. Large-scale DFT simulations with a linear-scaling DFT code CONQUEST on K-computer. *Journal of Advanced Simulation in Science and Engineering*, 1(1):87–97, 2014.

[101] Attila Szabó and Neil S. Ostlund. *Modern quantum chemistry: Introduction to advanced electronic structure theory*. Dover Publications, Mineola, N.Y., 1996.

[102] E. Artacho, D. Sánchez-Portal, P. Ordejón, A. García, and J. M. Soler. Linear-Scaling ab-initio Calculations for Large and Complex Systems. *physica status solidi (b)*, 215(1):809–817, 1999.

[103] David R. Bowler, Jack S. Baker, Jack T.L. Poulton, Shereif Y. Mujahed, Jianbo Lin, Sushma Yadav, Zamaan Raza, and Tsuyoshi Miyazaki. Highly accurate local basis sets for large-scale DFT calculations in conquest. *Japanese Journal of Applied Physics*, 58(10), 2019.

[104] Paolo Giannozzi, Stefano Baroni, Nicola Bonini, Matteo Calandra, Roberto Car, Carlo Cavazzoni, Davide Ceresoli, Guido L. Chiarotti, Matteo Cococcioni, Ismaila Dabo, Andrea Dal Corso, Stefano De Gironcoli, Stefano Fabris, Guido Fratesi, Ralph Gebauer, Uwe Gerstmann, Christos Gougoussis, Anton Kokalj, Michele Lazzeri, Layla Martin-Samos, Nicola Marzari, Francesco Mauri, Riccardo Mazzarello, Stefano Paolini, Alfredo Pasquarello, Lorenzo Paulatto, Carlo Sbraccia, Sandro Scandolo, Gabriele Sclauzero, Ari P. Seitsonen, Alexander Smogunov, Paolo Umari, and Renata M. Wentzcovitch. QUANTUM ESPRESSO: A modular and open-source software project for quantum simulations of materials. *Journal of Physics Condensed Matter*, 21(39), 2009.

[105] John P. Perdew, Adrienn Ruzsinszky, Gabor I. Csonka, Oleg A. Vydrov, Gustavo E. Scuseria, Lucian A. Constantin, Xiaolan Zhou, and Kieron Burke. Restoring the Density-Gradient Expansion for Exchange in Solids and Surfaces. *Physical Review Letters*, 100(13):136406, 2008.

[106] Susi Lehtola, Conrad Steigemann, Micael J.T. Oliveira, and Miguel A.L. Marques. Recent developments in LIBXC A comprehensive library of functionals for density functional theory. *SoftwareX*, 7:1–5, 2018.

[107] Kiarash Ahi. Review of GaN-based devices for terahertz operation. *Optical Engineering*, 56(09):1, 2017.

[108] Jack S Baker, Tsuyoshi Miyazaki, and David R Bowler. The pseudoatomic orbital basis: electronic accuracy and soft-mode distortions in ABO 3 perovskites. *Electronic Structure*, 2(2):025002, 2020.

[109] M. J. van Setten, M. Giantomassi, E. Bousquet, M. J. Verstraete, D. R. Hamann, X. Gonze, and G. M. Rignanese. The PSEUDODOJO: Training and grading a 85 element optimized norm-conserving pseudopotential table. *Computer Physics Communications*, 226:39–54, 2018.

[110] John R. Rumble. *CRC handbook of chemistry and physics*. CRC Press, 101 edition, 2020.

[111] Arnold Sommerfeld. *Mechanics of deformable bodies Lectures on theoretical physics*. Academic Press, 2nd edition, 1950.

[112] J F Nye. *Physical properties of crystals : their representation by tensors and matrices*. Oxford science publications. Clarendon Press, Oxford, 1985.

[113] L D Landau and E M Lifshitz. *Theory of elasticity*. Butterworth-Heinemann, Oxford [England] ; Burlington, MA, 3rd edition, 1986.

[114] T. Miyazaki, D. R. Bowler, R. Choudhury, and M. J. Gillan. Atomic force algorithms in density functional theory electronic-structure techniques based on local orbitals. *Journal of Chemical Physics*, 121(13):6186–6194, 2004.

[115] Antonio S. Torralba, David R. Bowler, Tsuyoshi Miyazaki, and Michael J. Gillan. Non-self-consistent density-functional theory exchange-correlation forces for GGA functionals. *Journal of Chemical Theory and Computation*, 5(6):1499–1505, 2009.

[116] O. H. Nielsen and Richard M. Martin. First-principles calculation of stress. *Physical Review Letters*, 50(9):697–700, 1983.

[117] O. H. Nielsen and Richard M. Martin. Quantum-mechanical theory of stress and force. *Physical Review B*, 32(6):3780–3791, 1985.

[118] O. H. Nielsen and Richard M. Martin. Erratum: Quantum-mechanical theory of stress and force. *Physical Review B*, 35(17):9308–9308, 1987.

[119] J. Ihm, Alex Zunger, and Marvin L. Cohen. Momentum-space formalism for the total energy of solids. *Journal of Physics C: Solid State Physics*, 12(21):4409–4422, 1979.

[120] J. Ihm, Alex Zunger, and Marvin L. Cohen. CORRIGENDUM: Momentum-space formalism for the total energy of solids. *Journal of Physics C: Solid State Physics*, 13(16):3095, 1980.

[121] O. H. Nielsen and Richard M. Martin. Stresses in semiconductors: Ab initio calculations on Si, Ge, and GaAs. *Physical Review B*, 32(6):3792–3805, 1985.

[122] Peter J. Feibelman. Pulay-type formula for surface stress in a local-density-functional, linear combination of atomic orbitals, electronic-structure calculation. *Physical Review B*, 44(8):3916–3925, 1991.

[123] G. P. Francis and M. C. Payne. Finite basis set corrections to total energy pseudopotential calculations. *Journal of Physics: Condensed Matter*, 2(19):4395–4404, 1990.

[124] G. M. Rignanese, Ph Ghosez, J. C. Charlier, J. P. Michenaud, and X. Gonze. Scaling hypothesis for corrections to total energy and stress in plane-wave-based ab initio calculations. *Physical Review B*, 52(11):8160–8178, 1995.

[125] H Hellmann. Einführung in die quantenchemie. *Franz Deutsche*, 1937.

[126] P. Pulay. Ab initio calculation of force constants and equilibrium geometries in polyatomic molecules. *Molecular Physics*, 17(2):197–204, 1969.

[127] Javier Junquera, Óscar Paz, Daniel Sánchez-Portal, and Emilio Artacho. Numerical atomic orbitals for linear-scaling calculations. *Physical Review B*, 64(23):235111, 2001.

[128] Eduardo Anglada, José M. Soler, Javier Junquera, and Emilio Artacho. Systematic generation of finite-range atomic basis sets for linear-scaling calculations. *Physical Review B - Condensed Matter and Materials Physics*, 66(20):1–4, 2002.

[129] N. Troullier and José Luriaas Martins. Efficient pseudopotentials for plane-wave calculations. *Physical Review B*, 43(3):1993–2006, 1991.

[130] D. R. Hamann. Optimized norm-conserving Vanderbilt pseudopotentials. *Physical Review B - Condensed Matter and Materials Physics*, 88(8), 2013.

[131] L. C. Balbás, José Luís Martins, and José M. Soler. Evaluation of exchange-correlation energy, potential, and stress. *Physical Review B - Condensed Matter and Materials Physics*, 64(16):1–7, 2001.

[132] J. Harris. Simplified method for calculating the energy of weakly interacting fragments. *Physical Review B*, 31(4):1770–1779, 1985.

[133] W. Foulkes and Roger Haydock. Tight-binding models and density-functional theory. *Physical Review B*, 39(17):12520–12536, 1989.

[134] A. J. Read and R. J. Needs. Tests of the Harris energy functional. *Journal of Physics: Condensed Matter*, 1(41):7565–7576, 1989.

[135] T. Ozaki and H. Kino. Efficient projector expansion for the ab initio LCAO method. *Physical Review B - Condensed Matter and Materials Physics*, 72(4):1–8, 2005.

[136] Rostam Golesorkhtabar, Pasquale Pavone, Jürgen Spitaler, Peter Puschnig, and Claudia Draxl. ElaStic: A tool for calculating second-order elastic constants from first principles. *Computer Physics Communications*, 184(8):1861–1873, 2013.

[137] Franz Knuth, Christian Carbogno, Viktor Atalla, Volker Blum, and Matthias Scheffler. All-electron formalism for total energy strain derivatives and stress tensor components for numeric atom-centered orbitals. *Computer Physics Communications*, 190:33–50, 2015.

[138] Norman T Huff, Ersan Demiralp, Tahir Çagin, and William A Goddard III. Factors affecting molecular dynamics simulated vitreous silica structures. *Journal of Non-Crystalline Solids*, 253(1-3):133–142, 1999.

[139] W. Kohn. Analytic properties of Bloch waves and Wannier functions. *Physical Review*, 115(4):809–821, 1959.

[140] W. Kohn and J. R. Onffroy. Wannier functions in a simple nonperiodic system. *Physical Review B*, 8(6):2485–2495, 1973.

[141] J. J. Rehr and W. Kohn. Wannier functions in crystals with surfaces. *Physical Review B*, 10(2):448–455, 1974.

[142] Jacques des Cloizeaux. Energy bands and projection operators in crystals. *Physical Review*, 135(3A):A685–A697, 1964.

[143] Uwe Stephan and David A. Drabold. Order projection method for first-principles computations of electronic quantities and Wannier functions. *Physical Review B - Condensed Matter and Materials Physics*, 57(11):6391–6407, 1998.

[144] Pablo Ordejón, David Drabold, Matthew Grumbach, and Richard M. Martin. Unconstrained minimization approach for electronic computations that scales linearly with system size. *Physical Review B*, 48(19):14646–14649, 1993.

[145] Walter Kohn. Density functional/Wannier function theory for systems of very many atoms. *Chemical Physics Letters*, 208(3-4):167–172, 1993.

[146] Roi Baer and Martin Head-Gordon. Sparsity of the density matrix in kohn-sham density functional theory and an assessment of linear system-size scaling methods. *Physical Review Letters*, 79(20):3962–3965, 1997.

[147] Sohrab Ismail-Beigi and T. A. Arias. Locality of the density matrix in metals, semiconductors, and insulators. *Physical Review Letters*, 82(10):2127–2130, 1999.

[148] Christian Brouder, Gianluca Panati, Matteo Calandra, Christophe Mourougane, and Nicola Marzari. Exponential localization of Wannier functions in insulators. *Physical Review Letters*, 98(4):1–4, 2007.

[149] Stefan Goedecker and M Teter. Tight-binding electronic-structure calculations and tight-binding molecular dynamics with localized orbitals. *Physical Review B*, 51(15):9455–9564, 1995.

[150] Francis Birch. Finite elastic strain of cubic crystals. *Physical Review*, 71(11):809–824, 1947.

[151] M. Hebbache and M. Zemzemi. Ab initio study of high-pressure behavior of a low compressibility metal and a hard material: Osmium and diamond. *Physical Review B - Condensed Matter and Materials Physics*, 70(22):5–10, 2004.

[152] Ask Hjorth Larsen, Jens Jørgen Mortensen, Jakob Blomqvist, Ivano E. Castelli, Rune Christensen, Marcin Dułak, Jesper Friis, Michael N. Groves, Bjørk Hammer, Cory Hargus, Eric D. Hermes, Paul C. Jennings, Peter Bjerre Jensen, James Kermode, John R. Kitchin, Esben Leonhard Kolsbjerg, Joseph Kubal, Kristen Kaasbjerg, Steen Lysgaard, Jón Bergmann Maronsson, Tristan Maxson, Thomas Olsen, Lars Pastewka, Andrew Peterson, Carsten Rostgaard, Jakob Schiøtz, Ole Schütt, Mikkel Strange, Kristian S. Thygesen, Tejs Vegge, Lasse Vilhelmsen, Michael Walter, Zhenhua Zeng, and Karsten W. Jacobsen. The atomic simulation environment - A Python library for working with atoms. *Journal of Physics Condensed Matter*, 29(27):273002, 2017.

[153] N. David Mermin. Thermal properties of the inhomogeneous electron gas. *Physical Review*, 137(5A):1–3, 1965.

[154] S. Goedecker. Decay properties of the finite-temperature density matrix in metals. *Physical Review B - Condensed Matter and Materials Physics*, 58(7):3501–3502, 1998.

[155] Pauli Virtanen, Ralf Gommers, Travis E. Oliphant, Matt Haberland, Tyler Reddy, David Cournapeau, Evgeni Burovski, Pearu Peterson, Warren Weckesser, Jonathan Bright, Stéfan J. van der Walt, Matthew Brett, Joshua Wilson, K. Jarrod Millman, Nikolay Mayorov, Andrew R.J. Nelson, Eric Jones, Robert Kern, Eric Larson, C. J. Carey, lhan Polat, Yu Feng, Eric W. Moore, Jake VanderPlas, Denis Laxalde, Josef Perktold, Robert Cimrman, Ian Henriksen, E. A. Quintero, Charles R. Harris, Anne M. Archibald, Antônio H. Ribeiro, Fabian Pedregosa, Paul van Mulbregt, Aditya Vijaykumar, Alessandro Pietro Bardelli, Alex Rothberg, Andreas Hilboll, Andreas Kloeckner, Anthony Scopatz, Antony Lee, Ariel Rokem, C. Nathan Woods, Chad Fulton, Charles Masson, Christian Häggström, Clark Fitzgerald, David A. Nicholson, David R. Hagen, Dmitrii V. Pasechnik, Emanuele Olivetti, Eric Martin, Eric Wieser, Fabrice Silva, Felix Lenders, Florian Wilhelm, G. Young, Gavin A. Price, Gert Ludwig Ingold, Gregory E. Allen, Gregory R. Lee, Hervé Audren, Irvin Probst, Jörg P. Dietrich, Jacob Silterra, James T. Webber, Janko Slavič, Joel Nothman, Johannes Buchner, Johannes Kulick, Johannes L. Schönberger, José Vinícius de Miranda Cardoso, Joscha Reimer, Joseph Harrington, Juan Luis Cano Rodríguez, Juan Nunez-Iglesias, Justin Kuczynski, Kevin Tritz, Martin Thoma, Matthew Newville, Matthias Kümmerer, Maximilian Bolingbroke, Michael Tartre, Mikhail Pak, Nathaniel J. Smith, Nikolai Nowaczyk, Nikolay Shebanov, Oleksandr Pavlyk, Per A. Brodtkorb, Perry Lee, Robert T. McGibbon, Roman Feldbauer, Sam Lewis, Sam Tygier, Scott Sievert, Sebastiano Vigna, Stefan Peterson, Surhud More, Tadeusz Pudlik, Takuya Oshima, Thomas J. Pingel, Thomas P. Robitaille, Thomas Spura, Thouis R. Jones, Tim Cera,

Tim Leslie, Tiziano Zito, Tom Krauss, Utkarsh Upadhyay, Yaroslav O. Halchenko, and Yoshiki Vázquez-Baeza. SciPy 1.0: fundamental algorithms for scientific computing in Python. *Nature Methods*, 17(3):261–272, 2020.

[156] Papiya Bose Roy and Sushil Bose Roy. Applicability of isothermal unrealistic two-parameter equations of state for solids. *Journal of Physics Condensed Matter*, 18(46):10481–10508, 2006.

[157] V. G. Tyuterev and Nathalie Vast. Murnaghan's equation of state for the electronic ground state energy. *Computational Materials Science*, 38(2):350–353, 2006.

[158] Michele Amato, Maurizia Palummo, and Stefano Ossicini. SiGe nanowires: Structural stability, quantum confinement, and electronic properties. *Physical Review B*, 80(23):235333, 2009.

[159] Alex R. Guichard, David N. Barsic, Shashank Sharma, Theodore I. Kamins, and Mark L. Brongersma. Tunable light emission from quantum-confined excitons in TiSi 2-catalyzed silicon nanowires. *Nano Letters*, 6(9):2140–2144, 2006.

[160] Ronit Popovitz-Biro, Andrey Kretinin, Palle Von Huth, and Hadas Shtrikman. InAs/GaAs core-shell nanowires. *Crystal Growth and Design*, 11(9):3858–3865, 2011.

[161] Magnus W. Larsson, Jakob B. Wagner, Mathias Wallin, Paul Håkansson, Linus E. Fröberg, Lars Samuelson, and L. Reine Wallenberg. Strain mapping in free-standing heterostructured wurtzite InAs/InP nanowires. *Nanotechnology*, 18(1):015504, 2007.

[162] Sònia Conesa-Boj, Francesca Boioli, Eleonora Russo-Averchi, Sylvain Dunand, Martin Heiss, Daniel Rüffer, Nicolas Wyrsch, Christophe Ballif, Leo Miglio, and Anna Fontcuberta I. Morral. Plastic and elastic strain fields in GaAs/Si core-shell nanowires. *Nano Letters*, 14(4):1859–1864, 2014.

[163] A. C. Meng, M. R. Braun, Y. Wang, C. S. Fenrich, M. Xue, D. R. Diercks, B. P. Gorman, M. I. Richard, A. F. Marshall, W. Cai, J. S. Harris, and P. C. McIntyre. Coupling of coherent misfit strain and composition distributions in coreshell Ge/Ge1-xSnx nanowire light emitters. *Materials Today Nano*, 5:100026, 2019.

[164] Lars Vegard. Der Mischkristalle und die Raumfüllung der Atome. *Zeitschrift für Physik*, 5(1):17–26, 1921.

[165] A R Denton and N W Ashcroft. Vegard's Law. *Physical Review A*, 43(6):3161–3164, 1991.

[166] Ekaterina I. Marchenko, Sergey A. Fateev, Andrey A. Petrov, Eugene A. Goodilin, Nikolay N. Eremin, and Alexey B. Tarasov. Transferable Approach of Semi-Empirical Modeling of Disordered Mixed-Halide Hybrid Perovskites $CH_3NH_3Pb(I_{1-x}Br_x)_3$: Prediction of Thermodynamic Properties, Phase Stability, and Deviations from Vegard's Law. *Journal of Physical Chemistry C*, 123(42):26036–26040, 2019.

[167] Liang Kong, Junqiu Guo, Joshua W. Makepeace, Tiancun Xiao, Heather F. Greer, Wuzong Zhou, Zheng Jiang, and Peter P. Edwards. Rapid synthesis of $BiOBr_xI_{1-x}$ photocatalysts: Insights to the visible-light photocatalytic activity and strong deviation from Vegard's law. *Catalysis Today*, 335:477–484, 2019.

[168] S. T. Murphy, A. Chroneos, C. Jiang, U. Schwingenschlögl, and R. W. Grimes. Deviations from Vegard's law in ternary III-V alloys. *Physical Review B - Condensed Matter and Materials Physics*, 82(7):073201, 2010.

[169] Yen Kuang Kuo, Bo Ting Liou, Sheng Horng Yen, and Han Yi Chu. Vegard's law deviation in lattice constant and band gap bowing parameter of zincblende $In_xGa_{1-x}N$. *Optics Communications*, 237(4-6):363–369, 2004.

[170] Zong Yan Zhao, Qing Lu Liu, and Wen Wu Dai. Structural, electronic, and optical properties of $BiOX_{1-x}Y_x$ (X, Y = F, Cl, Br, and I) solid solutions from DFT calculations. *Scientific Reports*, 6(1):1–12, 2016.

[171] A V G Chizmeshya, M R Bauer, and J Kouvetakis. Experimental and theoretical study of deviations from Vegard's law in the $Sn_xGe_{1-x}$ system. *Chemistry of Materials*, 15(13):2511–2519, 2003.

[172] H J Axon and W Hume-Rothery. The lattice spacings of solid solutions of different elements in aluminium. *Proceedings of the Royal Society of London. Series A. Mathematical and Physical Sciences*, 193(1032):1–24, 1948.

[173] K. A. Gschneidner and G. H. Vineyard. Departures from Vegard's law. *Journal of Applied Physics*, 33(12):3444–3450, 1962.

[174] Tomaš Stankevič, Simas Mickevičius, Mikkel Schou Nielsen, Olga Kryliouk, Rafal Ciechonski, Giuliano Vescovi, Zhaoxia Bi, Anders Mikkelsen, Lars Samuelson, Carsten Gundlach, and Robert Feidenhans'l. Measurement of strain in InGaN/GaN nanowires and nanopyramids. *Journal of Applied Crystallography*, 48(2):344–349, 2015.

[175] Ling Pan, Kok Keong Lew, Joan M. Redwing, and Elizabeth C. Dickey. Stranski-Krastanow Growth of Germanium on Silicon nanowires. *Nano Letters*, 5(6):1081–1085, 2005.

[176] Conn O Rourke, Shereif Y Mujahed, and Chathurangi Kumarasinghe. Structural properties of silicon germanium and germanium silicon core shell nanowires. *Journal of Physics: Condensed Matter*, 30, 2018.

[177] Shadi A. Dayeh, Jian Wang, Nan Li, Jian Yu Huang, Aaron V. Gin, and S. Thomas Picraux. Growth, Defect Formation, and Morphology Control of Germanium-Silicon Semiconductor Nanowire Heterostructures. *Nano Letters*, 11(10):4200–4206, 2011.

[178] Scott T. Dunham, Milan Diebel, Chihak Ahn, and Chen Luen Shih. Calculations of effect of anisotropic stress/strain on dopant diffusion in silicon under equilibrium and nonequilibrium conditions. *Journal of Vacuum Science and Technology B: Microelectronics and Nanometer Structures*, 24(1):456–461, 2006.

[179] Erik Bitzek, Pekka Koskinen, Franz Gähler, Michael Moseler, and Peter Gumbsch. Structural Relaxation Made Simple. *Physical Review Letters*, 97(17):170201, 2006.

[180] Y. Yano, T. Nakajima, and K. Shintani. Mechanical properties of Ge/Si core-shell nanowires under a uniaxial tension. In *Materials Research Society Symposium Proceedings*, volume 958, pages 213–218. Cambridge University Press, 2007.

[181] Adolfas Dargys and Jurgis Kundrotas. *Handbook on physical properties of Ge, Si, GaAs and InP*. Science and Encyclopedia Publishers, 1994.

[182] Xihong Peng and Paul Logan. Electronic properties of strained Si/Ge core-shell nanowires. *Applied Physics Letters*, 96(14):143119, 2010.

[183] Xihong Peng, Fu Tang, and Paul Logan. Band structure of Si/Ge core-shell nanowires along the [110] direction modulated by external uniaxial strain. *Journal of physics. Condensed matter : an Institute of Physics journal*, 23(11):115502, 2011.

[184] Alex J Lee, Minjung Kim, Charles Lena, and James R Chelikowsky. Mechanical and electronic properties of strained Ge nanowires using ab initio real-space pseudopotentials. *Physical Review B*, 86(11):115331, 2012.

[185] Yann Michel Niquet, Christophe Delerue, and Christophe Krzeminski. Effects of strain on the carrier mobility in silicon nanowires. *Nano Letters*, 12(7):3545–3550, 2012.

[186] M. A. Hopcroft, W. D. Nix, and T. W. Kenny. What is the Young's Modulus of Silicon? *Journal of Microelectromechanical Systems*, 19(2):229–238, 2010.

[187] Xueyan Wu, Jaideep S. Kulkarni, Gillian Collins, Nikolay Petkov, Dorothee Almécija, John J. Boland, Donats Erts, and Justin D. Holmes. Synthesis and electrical and mechanical properties of silicon and germanium nanowires. *Chemistry of Materials*, 20(19):5954–5967, 2008.

[188] Jinhui Song, Xudong Wang, Elisa Riedo, and Zhong L. Wang. Elastic property of vertically aligned nanowires. *Nano Letters*, 5(10):1954–1958, 2005.

[189] Min Feng Yu, Oleg Lourie, Mark J. Dyer, Katerina Moloni, Thomas F. Kelly, and Rodney S. Ruoff. Strength and breaking mechanism of multiwalled carbon nanotubes under tensile load. *Science*, 287(5453):637–640, 2000.

[190] Bin Wu, Andreas Heidelberg, and John J. Boland. Mechanical properties of ultrahigh-strength gold nanowires. *Nature Materials*, 4(7):525–529, 2005.

[191] Tobias Hanrath and Brian A. Korgel. Supercritical fluid-liquid-solid (SFLS) synthesis of Si and Ge nanowires seeded by colloidal metal nanocrystals. *Advanced Materials*, 15(5):437–440, 2003.

[192] Chao Zhang, Dmitry G. Kvashnin, Laure Bourgeois, Joseph F.S. Fernando, Konstantin Firestein, Pavel B. Sorokin, Naoki Fukata, and Dmitri Golberg. Mechanical, Electrical, and Crystallographic Property Dynamics of Bent and Strained Ge/Si Core-Shell Nanowires As Revealed by in situ Transmission Electron Microscopy. *Nano Letters*, 18(11):7238–7246, 2018.

[193] X. W. Liu, J. Hu, and B. C. Pan. The composition-dependent mechanical properties of Ge/Si core-shell nanowires. *Physica E: Low-Dimensional Systems and Nanostructures*, 40(10):3042–3048, 2008.

[194] S. K. Deb Nath, Naba Kumar Peyada, and Sung Gaun Kim. On the elastic modulus, and ultimate strength of Ge, Ge-Si nanowires. *Computational Materials Science*, 185:109931, 2020.

[195] Nuo Liu, Ning Lu, Yong Xin Yao, Yan Rong Li, Cai Zhuang Wang, and Kai Ming Ho. Strain effects in Ge/Si and Si/Ge core/shell nanowires. *Journal of Physical Chemistry C*, 115(32):15739–15742, 2011.

[196] Byeongchan Lee and Robert E Rudd. First-principles study of the Young's modulus of Si $\langle 001 \rangle$ nanowires. *Physical Review B - Condensed Matter and Materials Physics*, 75(4):041305, 2007.

[197] Paul W Leu, Alexei Svizhenko, and Kyeongjae Cho. Ab initio calculations of the mechanical and electronic properties of strained Si nanowires. *Physical Review B - Condensed Matter and Materials Physics*, 77(23):235305, 2008.

[198] M. Maksud, J. Yoo, C. T. Harris, N. K.R. Palapati, and A. Subramanian. Young's modulus of [111] germanium nanowires. *APL Materials*, 3(11), 2015.

[199] Y. Calahorra, O. Shtempluck, V. Kotchetkov, and Y. E. Yaish. Young's modulus, residual stress, and crystal orientation of doubly clamped silicon nanowire beams. *Nano Letters*, 15(5):2945–2950, 2015.

[200] J. J. Wortman and R. A. Evans. Young's Modulus, Shear Modulus, and Poisson's Ratio in Silicon and Germanium. *Journal of Applied Physics*, 36(1):153–156, 1965.

[201] E. Borchi, S. De Gennaro, R. Macii, and M. Zoli. Elastic moduli of polycrystalline Si and Ge. *Journal of Physics D: Applied Physics*, 21(8):1304–1305, 1988.

[202] Damon A. Smith, Vincent C. Holmberg, Doh C. Lee, and Brian A. Korgel. Young's modulus and size-dependent mechanical quality factor of nanoelec-

tromechanical germanium nanowire resonators. *Journal of Physical Chemistry C*, 112(29):10725–10729, 2008.

[203] Lien T Ngo, Dorothée Almécija, John E Sader, Brian Daly, Nikolay Petkov, Justin D Holmes, Donats Erts, and John J Boland. Ultimate-Strength Germanium Nanowires. *Nano Letters*, 6(12):2964–2968, 2006.

[204] Charles R. Harris, K. Jarrod Millman, Stéfan J. van der Walt, Ralf Gommers, Pauli Virtanen, David Cournapeau, Eric Wieser, Julian Taylor, Sebastian Berg, Nathaniel J. Smith, Robert Kern, Matti Picus, Stephan Hoyer, Marten H. van Kerkwijk, Matthew Brett, Allan Haldane, Jaime Fernández del Río, Mark Wiebe, Pearu Peterson, Pierre Gérard-Marchant, Kevin Sheppard, Tyler Reddy, Warren Weckesser, Hameer Abbasi, Christoph Gohlke, and Travis E. Oliphant. Array programming with NumPy. *Nature*, 585(7825):357–362, 2020.

[205] Kenneth Levenberg. A method for the solution of certain nonlinear problems in least squares. *Quarterly of Applied Mathematics*, 2(2):164–168, 1944.

[206] Donald W. Marquardt. An Algorithm for Least-Squares Estimation of Nonlinear Parameters. *Journal of the Society for Industrial and Applied Mathematics*, 11(2):431–441, 1963.

[207] Jorge J. Moré. The Levenberg-Marquardt algorithm: Implementation and theory. In G A Watson, editor, *Numerical Analysis*, volume 630, pages 105–116. Springer Berlin Heidelberg, 1978.

[208] Akram I. Boukai, Yuri Bunimovich, Jamil Tahir-Kheli, Jen-Kan Yu, William A. Goddard III, and James R. Heath. Silicon nanowires as efficient thermoelectric materials. *Nature*, 451(7175):168–171, 2008.

[209] M. W. Finnis. A faster way to relax interfaces in supercells. *Journal of Physics Condensed Matter*, 16(27), 2004.

[210] Stefan Goedecker, Frédéric Lançon, and Thierry Deutsch. Linear scaling relaxation of the atomic positions in nanostructures. *Physical Review B - Condensed Matter and Materials Physics*, 64(16):1–4, 2001.

[211] R. Dingle, H. L. Störmer, A. C. Gossard, and W. Wiegmann. Electron mobilities in modulation-doped semiconductor heterojunction superlattices. *Applied Physics Letters*, 33(7):665–667, 1978.

[212] Friedrich Schäffler. High-mobility Si and Ge structures. *Semiconductor Science and Technology*, 12(12):1515–1549, 1997.

[213] Irene A. Goldthorpe, Ann F. Marshall, and Paul C. McIntyre. Synthesis and strain relaxation of Ge-core/Si-shell nanowire arrays. *Nano Letters*, 8(11):4081–4086, 2008.

[214] Michele Amato, Maurizia Palummo, and Stefano Ossicini. Reduced quantum confinement effect and electron-hole separation in SiGe nanowires. *Physical Review B*, 79(20):201302, 2009.

[215] Alexis Nduwimana and Xiao-Qian Wang. Core and Shell States of Silicon Nanowires under Strain. *The Journal of Physical Chemistry C*, 114(21):9702–9705, 2010.

[216] T. Vo, A. J. Williamson, and G. Galli. First principles simulations of the structural and electronic properties of silicon nanowires. *Physical Review B - Condensed Matter and Materials Physics*, 74(4):045116, 2006.

[217] R. Rurali, A. Poissier, and N. Lorente. Size effects in surface-reconstructed 100 and 110 silicon nanowires. *Physical Review B - Condensed Matter and Materials Physics*, 74(16):1–8, 2006.

[218] M. V. Fernández-Serra, Ch. Adessi, and X. Blase. Surface segregation and backscattering in doped silicon nanowires. *Physical Review Letters*, 96(16):1–4, 2006.

[219] Ayako Nakata, Yasunori Futamura, Tetsuya Sakurai, David R. Bowler, and Tsuyoshi Miyazaki. Efficient Calculation of Electronic Structure Using O(N) Density Functional Theory. *Journal of Chemical Theory and Computation*, 13(9):4146–4153, 2017.

[220] Yann Michel Niquet and Christophe Delerue. Carrier mobility in strained Ge nanowires. *Journal of Applied Physics*, 112(8), 2012.

[221] Wei Lu, Jie Xiang, Brian P. Timko, Yue Wu, and Charles M. Lieber. One-dimensional hole gas in germanium/silicon nanowire heterostructures. *Proceedings of the National Academy of Sciences of the United States of America*, 102(29):10046–10051, 2005.

[222] Wei Lu, Ping Xie, and Charles M. Lieber. Nanowire transistor performance limits and applications. *IEEE Transactions on Electron Devices*, 55(11):2859–2876, 2008.

[223] Naoki Fukata, Mingke Yu, Wipakorn Jevasuwan, Toshiaki Takei, Yoshio Bando, Wenzhuo Wu, and Zhong Lin Wang. Clear Experimental Demonstration of Hole Gas Accumulation in Ge/Si Core - Shell Nanowires. *ACS Nano*, 9(12):12182–12188, 2015.

[224] David C. Dillen, Kyounghwan Kim, En-Shao Liu, and Emanuel Tutuc. Radial modulation doping in core-shell nanowires. *Nature Nanotechnology*, 9(2):116–120, 2014.

[225] Samit K. Ray, Ajit K. Katiyar, and Arup K. Raychaudhuri. One-dimensional Si/Ge nanowires and their heterostructures for multifunctional applications - A review. *Nanotechnology*, 28(9), 2017.

[226] Chris G Van de Walle and Richard M Martin. Theoretical calculations of heterojunction discontinuities in the Si/Ge system. *Physical Review B*, 34(8), 1986.

[227] Shouting Huang and Li Yang. Strain engineering of band offsets in Si/Ge core-shell nanowires. *Applied Physics Letters*, 98(9):2009–2012, 2011.

[228] Koichi Momma and Fujio Izumi. VESTA 3 for three-dimensional visualization of crystal, volumetric and morphology data. *Journal of Applied Crystallography*, 44(6):1272–1276, 2011.